Design and Characterization of the MEMS Sensor Fusion for Real Time Damage Detection in Structures

BY

HOSSAIN SABOONCHI
B.S. (Mechanical Engineering from Yazd University) 2005
M.S. (Mechanical Engineering from Isfahan University of Technology) 2008

THESIS

Submitted in partial fulfillment of the requirements
for the degree of Doctor of Philosophy in Civil Engineering
in the Graduate College of the
University of Illinois at Chicago, 2014

Chicago, Illinois

Defense Committee:

Dr. Didem Ozevin, Chair and Advisor
Dr. Farhad Ansari, Civil & Materials Engineering
Dr. Eduard Karpov, Civil & Materials Engineering
Dr. Sheng-Wei Chi, Civil & Materials Engineering
Dr. Laxman Saggere, Mechanical & Industrial Engineering

This thesis is dedicated to,

my loving, caring, kind and beautiful wife,

and my wonderful parents.

I'm blessed to have them in my life.

ACKNOWLEDGMENTS

I would like to thank the Civil & Materials Department of University of Illinois at Chicago for providing the opportunities and funding that made attending graduate school possible.

I would like to thank all of the individuals who helped me in the completion of this thesis. First and foremost my advisor, Dr. Ozevin who has been a knowledgeable mentor and a supportive friend during these years. I've always respected and envied her level of ambition, hard work and insight. I am truly grateful to have had the opportunity to work with and learn from her. Secondly my thesis committee, Dr. Ansari, Dr. Saggere, Dr. Karpov, and Dr. Chi for each of their willingness to review and provide valuable comments.

I would also like to thank members of Non-Destructive Evaluation laboratory over these years. Many thanks to Adam, Hazim, Lu, Hossein, Zeynab, Minoo, and Amir for providing a friendly work environment. Also, I would like to thank Dr. Ansari, Dr. Zhou, Dr. An, Dr. Royston, Dr. Dai, Mr. Taylor, and Mr. Mecha for opening their laboratories, providing testing equipment and support. Much appreciation to the department's staff, Pam, Sara, Dansel, and James. I also want to thank my immediate and extended family for their love, support, and encouragement. Finally and most importantly, I cherish the infinite love and inspiration that I get from my beloved wife, Zahra, with whom I've shared my happiness and sorrow, success and failure, days and nights, all these years.

CONTRIBUTION OF AUTHORS

The dissertation comprises of seven chapters. Chapter 1 introduces the motivation, objective and approach of the research. Chapter 2 reviews literature relevant to the subject of this research, including a review of common SHM methods, sensors for acoustic emission and strain measurement, and a brief description of the MetalMUMPs. The design parameters, numerical and experimental characterizations of the MEMS out-of-plane AE sensors are discussed in chapter 3. The content presented in the chapter 3 was previously published [1] with my PhD advisor as the co-author. The design parameters, numerical and experimental characterizations of the MEMS in-plane AE sensors are discussed in chapter 4. Chapter 4 was partially published [2] with my PhD advisor as the co-author. I anticipate that this part of research will be continued in the laboratory after I leave and the results will be published as part of a co-authored manuscript. The design parameters, numerical and experimental characterizations of the MEMS strain sensors are presented in chapter 5. The content presented in the chapter 5 was previously published [3] with my PhD advisor as the co-author. The combined behavior of the MEMS AE and strain sensors for detecting the initiation and growth of fatigue crack in aluminum 7075 specimens is presented in chapter 6. Chapter 6 is partially presented [4] and will be published to a journal with my PhD advisor as the co-author. Finally, the conclusions and future work are discussed in chapter 7.

TABLE OF CONTENTS

TABLE OF CONTENTS (Continued)

CHAPTER **PAGE**

TABLE OF CONTENTS (Continued)

CHAPTER **PAGE**

LIST OF TABLES

LIST OF TABLES (Continued)

TABLE **PAGE**

LIST OF FIGURES

LIST OF FIGURES (Continued)

LIST OF FIGURES (Continued)

FIGURE **PAGE**

LIST OF FIGURES (Continued)

FIGURE **PAGE**

LIST OF FIGURES (Continued)

LIST OF FIGURES (Continued)

FIGURE **PAGE**

LIST OF ABBREVIATIONS

AE	Acoustic Emission
DR	Dynamic Range
MEMS	Micro-Electro-Mechanical Systems
MetalMUMPs	Metal-Multi-User-MEMS-Processes
SHM	Structural Health Monitoring
SNR	Signal to Noise Ratio

SUMMARY

Micro-electro-mechanical systems (MEMS) have diverse manufacturing capabilities to design and manufacture various sensing elements in order to monitor various mechanical behaviors in structures. In this study, capacitive acoustic emission sensors are integrated with piezoresistive strain sensors on a small footprint device. The integrated sensing allows redundant data measurement from a given point and intelligent data collection strategy in order to increase the reliability of Structural Health Monitoring (SHM) methods.

The acoustic emission (AE) sensors are designed with the principle of capacitance change under dynamic excitation, and tuned to the range of 60 kHz to 150 kHz via changing spring and mass geometry. The MetalMUMPs (Multi-User-MEMS-Processes) are implemented to manufacture the sensors on a 1 cm x 1 cm device area. Using surface micromachining method, the MEMS AE sensors have improved signal to noise characteristics as compared to the designs. The sensor sensitivities are comparable to piezoelectric sensors. Considering the relative sizes of two sensor types, this is a significant achievement in the field of AE sensor design.

Four different MEMS AE sensors are designed on the same device: two out-of-plane sensors with the transduction principle of capacitive gap change, and two in-plane sensors (comb drives) with the transduction principles of capacitive gap change and area change. Since the sensors are tuned to a particular frequency, the influence of the background noise outside the frequency bandwidth of interest is limited. If the sensors are tuned to a particular wave direction, wave velocity in plate-like structures can be estimated accurately, which improves the source localiza-

tion capability of the AE method. The experimental characterization includes capacitance and impedance measurement, and mechanical simulation experiments including laser, ball impact and pencil lead break for the comparison with conventional piezoelectric sensors.

The MEMS strain sensors are designed with the principle of piezoresistivity property of polysilicon, which have higher gauge factor as compared to conventional metal gauges. For the design of strain sensors, trenching concept is implemented to increase the strain transfer, and strain-free resistance is limited to near 350 Ω in order to use conventional Wheatstone bridge data acquisition systems designed for metal gauges. Three strain sensors are placed in horizontal, vertical and angled directions to extract the principle stresses. The influences of the sensor position on the silicon substrate and the trenching to the strain transfer from structure under loading to polysilicon layer are numerically demonstrated, and experimentally validated. The characterization experiments include monotonic, cyclic and fatigue mechanical loading, and thermal loading.

Combining strain sensors on the same package of other SHM sensors can tackle several limitations of SHM methods such as the need of redundant measurement to increase the reliability and defining idle/active mode of acoustic emission sensor using strain sensor to reduce the power consumption, and enabling the integration of the energy harvesting devices.

The concurrent performance of MEMS strain sensors and acoustic emission sensors is tested under fatigue loading of two notched aluminum specimens. The strain sensor strengthens the interpretation of complex acoustic emission data via monitoring the driving force and allowing on-chip data filtering in order to process the data recorded from high stress levels.

CHAPTER 1

INTRODUCTION

1.1 Motivation

More than eleven percent of the bridges in the US are categorized as structurally deficient [5]. According to a report published by the Transportation for America group in 2013, the average age of a bridge is about 43 years, despite the fact that most bridges are designed to last 50 years before major repair or replacement [5]. Considering the volume of bridges, a prioritization method for determining which bridges should be repaired or replaced is needed. Structural Health Monitoring (SHM) methods are based on installing sensors on structures for continuously assessing their state for potential degradation. The SHM methods can be implemented for understanding the state of a structure after the preliminary assessments are conducted to determine the prior condition. Proper monitoring strategies will warn if any structural behaviors deviate from the accepted values.

The common SHM methods are guided wave ultrasonics, vibration monitoring, strain monitoring, and acoustic emission. Guided wave ultrasonics is an active SHM method since a perturbation is introduced to a structure and variations in propagating waves are examined as an indication of damage. Vibration, strain and acoustic emission are passive SHM methods since sensors detect the structural behavior due to structurally introduced motion such as acceleration due to dynamic loading induced by traffic or wind. The challenge of guided wave

ultrasonics for civil structures is that every structure has a unique design that requires the development of new baseline data, as there is no repeatable baseline data available [6]. Three passive NDE techniques, strain gage (e.g. [7]), vibration (e.g. [8]) and acoustic emission (AE) [9] are typically used in large scale structural monitoring such as highway bridges. Static and dynamic strain measurement provides localized information and is influenced by the factors other than damage (e.g. temperature). The vibration method relies on changes in modal properties of structures such as fundamental frequencies and mode shapes. However, the method requires significant damage in the structure in order to detect its presence in the frequency harmonics of the structure as compared to the baseline data. Additionally, strain and vibration based methods cannot detect the nucleation of damage.

The AE method relies on the release of energy from newly formed damage surfaces, as shown in Figure 1. When a crack grows due to the loading of a structure, the change in the stress-strain field at the crack tip causes the propagation of transient waves. The AE sensors are typically mounted on the surface of the structure and detect the surface motion. While the AE method is capable of source localization by means of local, global, remote or online monitoring, the issue of background noise interference with damage emissions is a critical problem that may require severe data cleaning and experienced personnel [9]. An intelligent data acquisition at the sensor level is needed for the reliable application of the AE method.

There are two important components of successful implementation of the AE method: the data acquisition strategy and the sensor. Typical data acquisition of the AE method is based on threshold: if the signal level at a sensor output channel is higher than the pre-set threshold

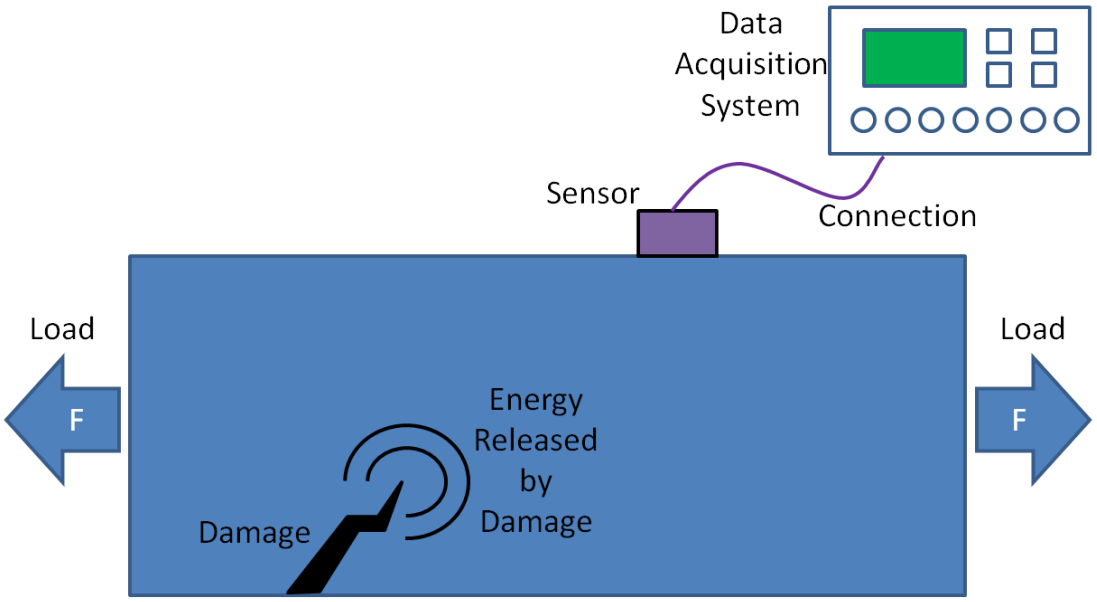

Figure 1. Schematic of active flaw detection using the AE method

level, the data acquisition system acquires the AE data. This approach can cause high hit-rate and recording of irrelevant data, where relevant data is defined as the propagating elastic waves due to newly formed damage surfaces other than secondary sources such as friction. Strain-based or load-based triggering mechanisms have been explored in the literature; however, they rely on additional sensor installation, which increases the cost of the SHM method.

Typical AE sensors are made of piezoelectric ceramics, which can be designed as resonant or broadband types. The resonant sensors are highly sensitive to a specific frequency bandwidth. The broadband sensors are not as sensitive as the resonant sensors due to the damping material in order to achieve a wideband frequency response; however, they do not influence the waveform

signature of the source mechanisms. They are bulky in size and weight, which complicates long-term installation. The other alternative sensor type is Micro-Electro-Mechanical-Systems (MEMS) based AE sensors with the transduction mechanism of capacitance. However, the current MEMS AE sensors in the literature do not have sufficient sensitivity in order to detect the early stage of damage.

To achieve real time identification of damage in structures, it is necessary to bring about a paradigm shift in the state of the art of the AE method. The methodology needs to be minimally invasive for integration within various structural elements; easily mass produced and enabling cost effective implementation for use in the large-scale structural systems. Using the diverse materials and manufacturing methods available in the MEMS field, an innovative single device accommodating several sensing elements, while having a small footprint can be designed.

1.2 Objectives, Scope and Approach

1.2.1 Objectives of Research

The objective of this research is to minimize the collection of irrelevant AE data using the on-chip strain-based triggering approach. The AE and strain sensors are designed and manufactured on the same device using the MEMS technology. The hypothesis of the research objective is that cracks will initiate and grow under high load levels. The AE system can be in idle-mode when strain level is below the pre-defined threshold. The AE system will be then active-mode when strain level is above the threshold, and wait for emissions released from active flaws. The strain-based triggering approach for the AE data collection will significantly reduce the collection of irrelevant data, minimize the decision making process, and enable

wireless/energy harvesting system integration for long term monitoring of structures. The research has four major steps to achieve the research objective, and test the hypothesis:

- Step 1: Design, manufacture and characterize capacitive MEMS AE sensors with comparable sensitivity to piezoelectric types. The design constraints of the MEMS AE sensors are:
  - Minimum capacitance of 20 pF to increase the sensitivity;
  - Maximum size of 5 mm in each direction to prevent the aperture effect;
  - Two different frequencies applicable for civil structures (60 kHz for concrete, 150 kHz for steel);
  - Two different sensors sensitive to unique wave direction (out-of-plane and in-plane) to increase the accuracy of source localization.
- Step 2: Design, manufacture and characterize a polysilicon based MEMS strain sensor to identify the dynamic strain at the location of the integrated MEMS device;The design constraints of the MEMS strain sensors are:
  - Resistance near 350 Ω in order to utilize existing data acquisition systems;
  - The strain transfer from the substrate to sensor should be maximized;
  - The strain sensors should be positioned at three angles to extract the principle stresses.
- Step 3: Minimize the AE data collection rate intelligently through eliminating the influence of background noise;

- Step 4: Validation on the laboratory scale geometry.

1.2.2 Scope of Research

The scope of research includes the design, modeling and characterization of capacitive MEMS AE sensors and piezoresistive MEMS strain sensors manufactured using the MetalMUMPs (Metal Multi-User MEMS Processes) on a 1 cm x 1 cm device area. The MetalMUMPs provide specific features to manufacture sensors, and enable prototype sensor manufacturing. The service is provided by MEMSCAP Inc., located in North California. The hypothesis validation is limited to laboratory scale fatigue testing of aluminum coupon samples.

1.2.3 Summary of Approach

The resonant type MEMS AE sensors are tuned to the particular directions and frequencies, which are commonly selected in civil engineering structures (e.g., 60 kHz for concrete, 150 kHz for metals). Four different MEMS AE sensors are designed on the same device: two out-of-plane sensors with the transduction principle of capacitive gap change and tuned to 60 kHz and 150 kHz, and two in-plane sensors (comb drives) with the transduction principles of capacitive gap change and area change. Since the sensors are tuned to a particular frequency, the influence of background noise outside the frequency bandwidth of interest is limited. If the sensors are tuned to a particular wave direction, wave velocity in plate-like structures can be estimated accurately, which improves the source localization capability of the AE method. The experimental characterization includes capacitance and impedance measurement, and mechanical simulation experiments including laser, ball impact and pencil lead break for the comparison with conventional piezoelectric sensors.

The MEMS strain sensors are utilized in order to determine the threshold load level for triggering the active mode of the AE sensors. Strain-based triggering mechanism, where the AE data is recorded when strain (i.e., load) level is high, significantly reduces the collection of irrelevant data, which further reduces the size of data collected, and facilitates the interpretation of the AE data. For the design of strain sensor, the trenching concept is implemented to increase the strain transfer, and strain-free resistance is limited to near 350 Ω in order to use conventional Wheatstone bridge data acquisition systems designed for metal gauges. The characterization experiments include monotonic, cyclic and fatigue mechanical loading, and thermal loading.

After the individual characterizations of MEMS AE and strain sensors are completed, the concurrent performance of the sensors is demonstrated on fatigue testing of notched aluminum 7075 coupon samples. The results show that the MEMS AE sensors have significantly low noise level than piezoelectric AE sensors because of narrow frequency bandwidth, and can detect the initiation of damage similar to piezoelectric AE sensors. The MEMS strain sensors can track the fatigue cycles while they are highly influenced by thermal drift, which can be reduced with an on-chip full-bridge configuration.

The figure placed in Table I shows the final layout of the MEMS device accommodating AE and strain sensors as well as accelerometers. However, the characterization of the accelerometers will be future work. Table II describes the characteristics of the sensors and their locations on the device.

TABLE I

OVERALL SENSORS LOCATIONS

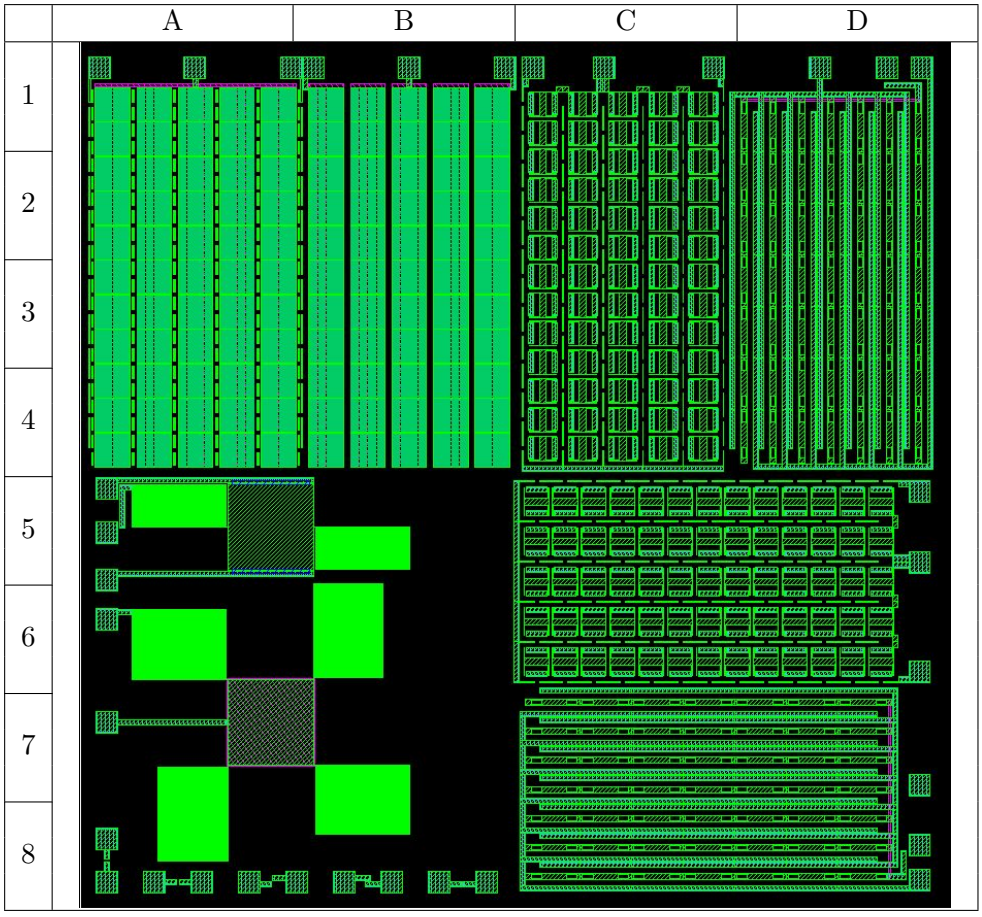

TABLE II

SENSORS DESCRIPTIONS

ID	Location	Type	Mode	Principal
S1	A(1 -4)	Acoustic Emission Sensor	Out-of-plane mode	Gap change-z
S2	B(1-4)	Acoustic Emission Sensor	Out-of-plane mode	Gap change-z
S3	C(1-4)	Acoustic Emission Sensor	In-plane mode	Gap change-y
S4	D(1-4)	Acoustic Emission Sensor	In-plane mode	Area change-x
S5	C,D(5,6)	Acoustic Emission Sensor	In-plane mode	Gap change-x
S6	C,D(7,8)	Acoustic Emission Sensor	In-plane mode	Area change-y
S7	A,B(5)	Accelerometer/Inertia Switch	In-plane mode	Gap change-y
S8	A,B(6,7)	Accelerometer/Inertia Switch	Out-of-plane mode	Gap change-z
S9	A,B(8)	Strain Sensor	Single element	Resistance
S10	A,B(8)	Strain Sensor	Rosetta design	Resistance

1.3 Organization of Dissertation

The dissertation comprises of seven chapters. Following the introductory chapter, chapter 2 reviews literature relevant to the subject of this research, including a review of common SHM methods, sensors for acoustic emission and strain measurement, and a brief description of the MetalMUMPs. The design parameters, numerical and experimental characterizations of the MEMS out-of-plane AE sensors are discussed in chapter 3. The design parameters, numerical and experimental characterizations of the MEMS in-plane AE sensors are discussed in chapter 4. The design parameters, numerical and experimental characterizations of the MEMS strain sensors are discussed in chapter 5. The combined behavior of the MEMS AE and strain sensors

for detecting the initiation and growth of fatigue crack in aluminum 7075 specimens is presented in chapter 6. Finally, the conclusions and future work are discussed in chapter 7.

CHAPTER 2

BACKGROUND

The content of this chapter was partially previously published as "MEMS acoustic emission transducers designed with high aspect ratio geometry" in the journal of smart materials and structures with my advisor, Dr. Ozevin, as the co-author [1], also as "In-Plane MEMS Acoustic Emission Sensors Development and Experimental Characterization" in the "Proceedings of the 2013 Annual Conference on Experimental and Applied Mechanics" with my advisor, Dr. Ozevin, as the co-author [2] .

2.1 Introduction

This chapter begins with the descriptions of common SHM methods, their advantages and drawbacks. The conventional sensors and their current alternatives for measuring acoustic emission and strain are discussed. The MetalMUMPs manufacturing procedure is explained in the last section of this chapter.

2.2 Structural Health Monitoring (SHM) Methods

The current approaches for estimating the remaining life of structural components requires significant amount of historical information, and may not provide the information sufficiently early [10],[11]. They are based on a number of assumptions related to the definition of a healthy/damaged state, its relationship with neighboring states, and their dependence on the different types of loading conditions. Damage is amulti-scale process which inherently is dy-

namic [12]. Damage in structures consists of several stages and which can be varied significantly based on overall component design and material type. However, in structural assessment, detection of early stage of damage initiation and progression is vital to avoid catastrophic failures by responding promptly. For this purpose, SHM methods provide information related to the damage initiation and progression in structures.

The passive SHM methods are based on the processing of sensor data related to structural properties without introducing any external stimulus to structures. There are three common passive SHM methods implemented in monitoring damage in large-scale structures: vibration method, strain measurement and acoustic emission. The vibration method requires placing accelerometers on a structure to extract modal properties such as fundamental frequencies and mode shapes. The method has been studied by several researchers, and installed on several bridges for continuous monitoring (e.g. [13]). However, the method requires significant damage in the structure in order to detect its presence in modal properties of the structure as compared to the baseline data, or installing many accelerometers to extract higher order harmonics, which are more sensitive to flaws.

The strain method requires placing strain sensors at strategic locations on a structure to extract one or multi-directional strain due to live load or time-dependent load such as temperature. The strain sensors are nonintrusive, effective sensors in order to monitor strain-time traces for health monitoring and the estimation of damage progress ([14], [15], [16]), or total strain in laboratory scale experiments to measure crack velocity and static or dynamic initiation toughness if they are positioned in away that the sensors and the crack growth are in lined

[17]. Additionally, the strain sensors provide fundamental information needed for reliability based damage prognostics such as cyclic count and threshold driving force for crack initiation and growth ([18], [19]). Three fundamental characteristics of a strain sensor to achieve those capabilities described above are (1) good spatial resolution to measure strain at a point, (2) unaffected response from the ambient conditions and (3) high frequency response for the dynamic measurement [20]. The drawback of conventional metal gauges is minimum size limitation with sufficient sensitivity that significantly affects the strain reading in the regions of high strain gradient such as crack tips. If the metal gauges are used for measuring strain, high strain gradient at the singularity domain will cause unacceptable error. Additionally, the error due to lateral sensitivity of commercial strain gauge increases with the increase in dimensions, in the range of 0.05 to -0.19 % [20]. The strain distribution at the singularity region can be measured using the photo-stress coating and interferometer (optical method), which is expensive and not feasible for field deployment. Static and dynamic strain measurement provides localized information and is influenced by factors other than damage (e.g. temperature), which requires a compensation circuitry.Common resistive type strain sensors converts mechanical strain (i.e. input) transfered from structure to strain sensor into electrical voltage (i.e. output) using Wheatstone bridge. It is schematically drawn in Figure 2.

The AE method relies on the release of energy from newly formed damage surfaces, as shown in Figure 1 where energy is released in the form of stress waves. When a crack grows under loading, the stress-strain field changes at the crack tip, which causes the propagation of transient waves. The AE sensors are mounted on the surface of the structure and detect

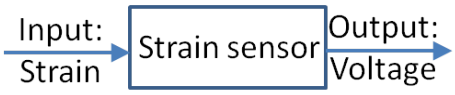

Figure 2. The transfer block of strain sensors

Figure 3. The transfer block of capacitive AE sensors

the surface motion, which is called AE signal. The transfer block of AE sensors convert the mechanical surface motion (i.e. input: acceleration, velocity or displacement) to electrical voltage (i.e. output). The transfer block of capacitive AE sensors is schematically drawn in Figure 3.

The AE signals are represented by various time dependent and frequency dependent features for pattern recognition methods. Figure 4 shows a typical waveform, and the first threshold crossing at t_{start} and the last threshold crossing at t_{end}, identifies the total duration of an AE signal. The integration of waveform with respect to time is the AE energy. The AE amplitude is the maximum amplitude of the time domain waveform. The amplitude and energy are related to the intensity of the source, consequently crack velocity. The frequency content of

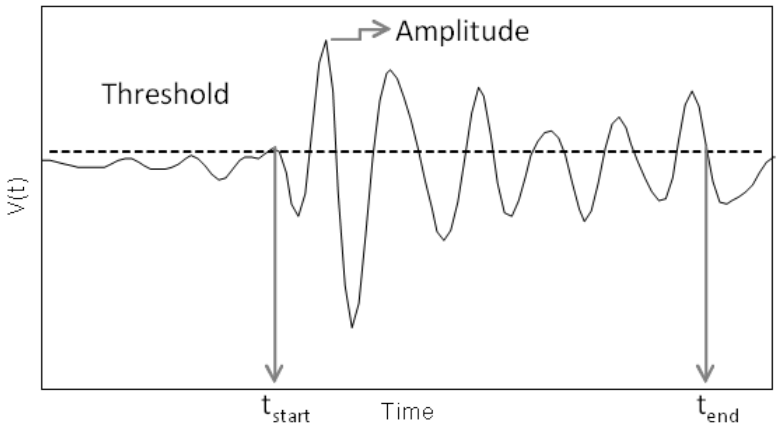

Figure 4. Acoustic emission waveform and crack velocity related features

the AE waveform informs about various source mechanisms such as crack growth, rubbing of crack surfaces and mechanical friction due to vibration. Pattern recognition methods using multivariate analysis mixed with time domain and frequency domain features are implemented to differentiate source mechanisms. The early part of the AE waveform represents the source mechanisms (e.g. crack growth, yielding) as the later parts of the AE waveform are affected by sensor ringing and reflections.

One of the advantages of the AE method is that it can identify the source location in 1D, 2D or 3D if an array of sensors are used. The minimum number of sensors required to identify the n dimensions of an unknown coordinates, is $n+1$. For example, Figure 5 shows a 2D source location on a steel connection, which requires a minimum of three sensors in order to determine damage coordinates. Propagating elastic waves due to a newly formed damage source reach

the AE sensors at different times due to their relative locations to the source. Using the arrival times of three sensors, locations of the sensors and wave velocity as known variables, unknown coordinates are calculated. The variables that affect an accurate source location using the AE method are relative location of the sensors and source, wave velocity, amplitude/threshold ratio, and system busyness.

While the AE method is capable of source localization by means of local, global, remote, or online monitoring, the issue of background noise (such as friction) interference with damage emissions is a critical problem that may require severe data cleaning and experienced personnel. Developing a standard test procedure applicable to various materials and geometries is also a challenge because of complexity in the measurement process.

Table III summarizes the advantages and drawbacks of three common passive type SHM methods. The objective of this research is to reduce the drawbacks of the AE method through integrating AE and strain sensors on the same platform using micromachining methods for redundant measurement and generating a trigger mechanism for the AE sensors based on strain data in order to record AE data at high strain values when crack initiation and growth is expected.

2.3 AE sensors

2.3.1 Piezoelectric Sensors

Piezoelectricity is the electric charge that accumulates in certain solid materials (such as crystals, certain ceramics, and some biological matters) in response to applied mechanical stress

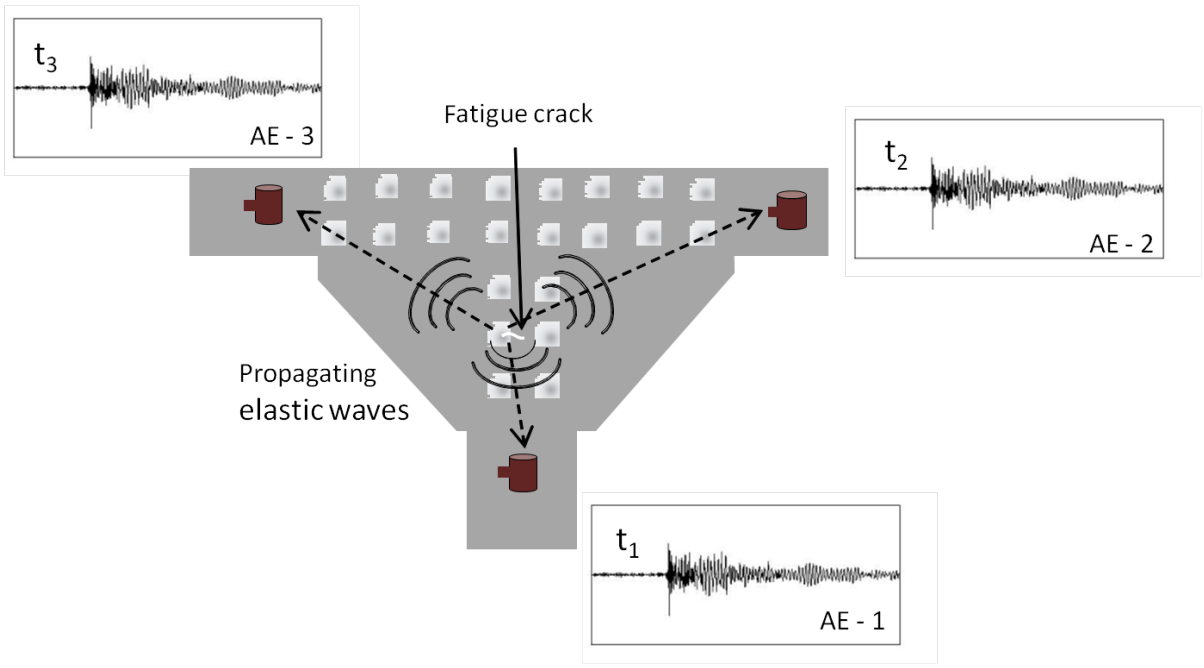

Figure 5. The application of the Acoustic Emission method on a structural connection

TABLE III

THE COMPARISON OF THREE COMMON SHM STRATEGIES FOR MONITORING LARGE-SCALE STRUCTURES

Method	Advantages	Drawbacks
System identification	Well-established method, Direct understanding structural properties such as vibrational modes and frequencies	Insensitive to small flaws Need of densely populated sensors for extracting higher modes of vibration
Strain monitoring	Well-established method, Sensitive to static and dynamic strains	Influence of secondary sources such as temperature, Need of densely populated sensors for increasing sensitivity
Acoustic emission	Sensitive to micro-flaws, Capable of detecting and locating hidden defects, Global and local monitoring opportunity	Influence of background noise, Complex data collection process that challenges the repeatability and signal processing

[21]. The constitutive equations of piezoelectric materials are a coupled set between electrical charge and mechanical stress [22] as:

$$S_{ij} = s^{D}_{ijkl} T_{kl} + g_{kij} D_k \tag{2.1}$$

$$E_i = -g_{ikl} T_{kl} + \beta^{T}_{ik} D_k \tag{2.2}$$

"where S_{ij} is the strain tensor, s^{D}_{ijkl} is the compliance matrix at constant electric displacement, T_{kl} is the stress tensor, g_{kij} is the piezoelectric voltage confident, D_k is the electric displacement, E_i is the electric field, and β^{T}_{ijkl} is the inverse of the effective dielectric permittivity ϵ_{ik} at constant stress" [22].

The fundamental benefits of piezoelectric AE sensors are high sensitivity and independence of external power. Typical AE sensors are made of piezoelectric ceramics (e.g. PZT-5H), which can be designed as resonant or broadband types. The resonant sensors are highly sensitive to a specific frequency bandwidth. The geometry of piezoelectric material is designed in a way to have its fundamental frequency at thickness mode as its resonant frequency. Figure 6 shows examples of piezoelectric AE sensors manufactured by Mistras Group Inc. When the target frequency decreases, the size of the AE sensor increases significantly. Therefore, low frequency miniature AE sensors cannot be designed using piezoelectricity. The broadband sensors are not as sensitive as the resonant sensors due to the damping material used to achieve a wideband frequency response. Broadband sensors do not influence the waveform signature of the source mechanisms. However, they are highly fragile and not suitable for field deployment.

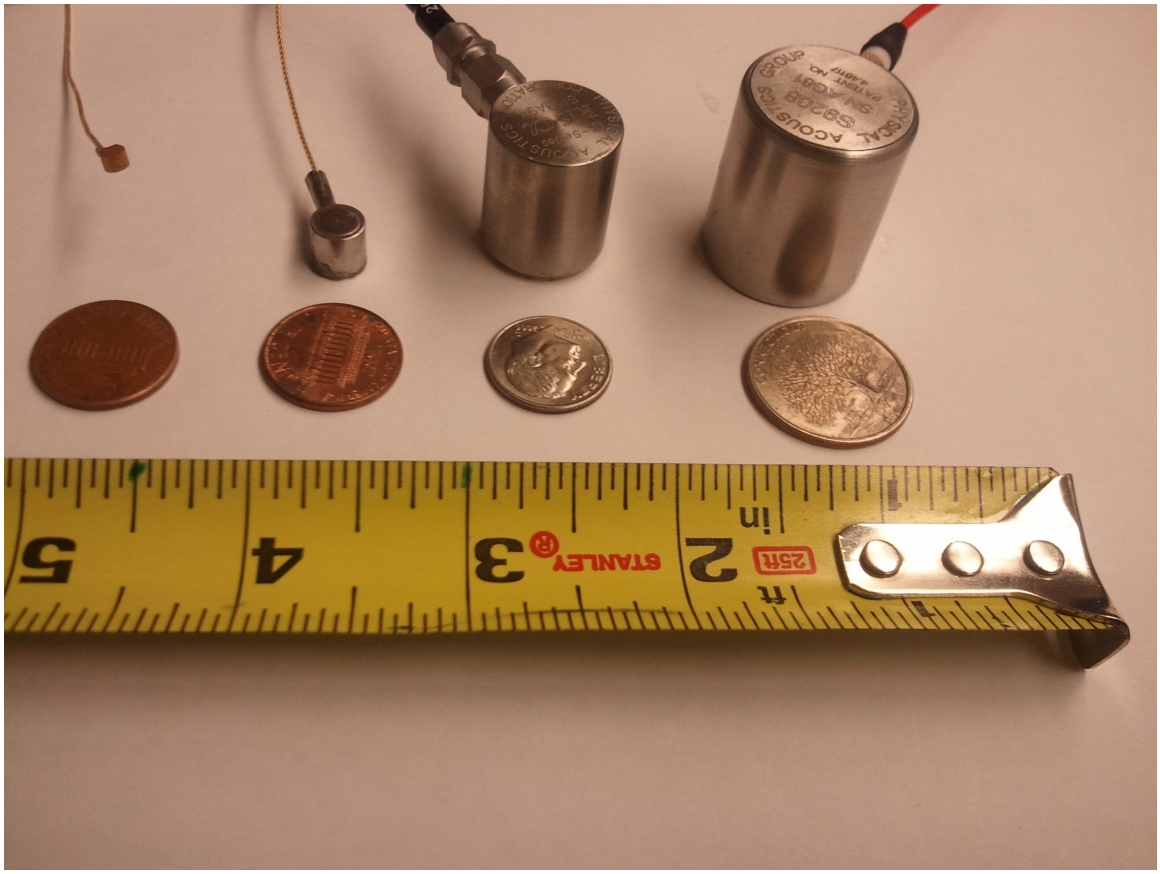

Figure 6. Typical AE sensors and dimensions for different frequencies (from left to right:) MHz, Mhz/kHz, kHz, and broadband

Pickwell et al [23] used MEMS to miniaturize the piezoelectric element; however, the detection of AE in a dynamic application failed due to the low signal to noise ratio. Feng and Tsai [24] used the micro-embossing fabrication method to constructe the multi-piezoelectric layers. While the size of sensing element is micro level, the required backing material increases the overall size of the sensor significantly.

2.3.2 MEMS Type Capacitive Sensors

Capacitive MEMS sensors are made using two parallel plates as the electrodes separated by a dielectric material, typically air. The capacitance is calculated by the following equation:

$$C = \epsilon_0 \epsilon_r \frac{A}{d} \tag{2.3}$$

where C is capacitance, ϵ_0 is the electric constant ($\epsilon_0 \approx 8.854 \times 10^{-12} Fm^{-1}$), ϵ_r is the relative static permittivity of the material between the plates (for a vacuum $\epsilon_r = 1$), A is the area of the plates which face each other, and d is the gap between the plates. The capacitance change may occur due to changes in one or more parameters given in Equation 2.3:

$$\frac{\delta C}{C} = \frac{\delta \epsilon}{\epsilon} + \frac{\delta A}{A} - \frac{\delta d}{d} \tag{2.4}$$

where ϵ will remain constant during the sensor operation since it is a material property (unless a chemical reaction is involved) while the other two terms can vary with an external stimulus. The sensor can be designed as the area change or the gap change with a specific geometric design. The critical parameter considered for the design of the resonant type capacitive MEMS

AE sensor is the natural frequency of vibration at the sensing direction. The natural frequency determines which wave frequency is detected, functioning as an on-chip filter. The fundamental frequency of the capacitive MEMS sensor idealized as a single degree of freedom system can be calculated using the following equation:

$$f = 2\pi\sqrt{\frac{K_{mech}}{m}} \tag{2.5}$$

where f is frequency, K_{mech} is the mechanical stiffness, and m is the mass of the system.

While there are many studies in the literature on MEMS-based capacitive accelerometers (e.g., add a few references here), there are limited MEMS capacitive AE sensors. The main differences are frequency range and level of input signal. The AE sensors require sensing pm level displacement while accelerometers are sensitive to a level of 0.1g acceleration (please check this out). MEMS AE sensors are designed using a surface micromachining method with the transduction principle of capacitance change. Ozevin et al [25] developed capacitive type resonant MEMS AE sensors that span the frequency range of 100 kHz to 500 kHz. The MEMS sensors were approximately fifty times less sensitive than the conventional piezoelectric AE sensors in atmospheric pressure. Harris [26] optimized the properties of capacitive MEMS AE sensors to reach a sensitivity level comparable with the conventional AE sensors. The MEMS device in this study had a reduced damping geometry in order to increase the resonant response at atmospheric pressure. The MEMS AE sensors developed in these studies ([25], [26]) were manufactured using PolyMUMPs (polysilicon multi-user MEMS processes), which

limits the microstructure thickness to 2 μm and the gap between the stationary layer and the freely moving microstructure layer to 1.25 μm. The process requirements limit any further design optimization. PolyMUMPS also has no additional dielectric layer between stationary and moving electrodes other than air. The possibility of stiction reduces the reliability for long-term usage of the sensors for the SHM applications. Auerswald et al [27] designed a comb-drive type AE sensor with the capacitance change principle; however, the sensor has a lack of sensitivity problem.

2.4 Resistive Type Strain Sensors

Measuring strain is crucial for stress analyses and SHM methods in order to monitor driving forces in structures under varying amplitude cyclic loading, initiation of fatigue damage, excessive loading, etc. The application field ranges from large scale to small scale, such as highway bridges, wind turbine blades, and rotating machinery. For instance, Benedetti et al. [16] concluded that the strain change at the vicinity of a fatigue crack, which is initiating at the wind turbine towers, is the best index to detect the crack initiation. Liu et al. [15] implemented the strain data for the reliability measure of bridge systems. The most common strain sensors are metal gauges, fiber optic sensors [28], and semiconductor sensors [29], [30], [31].

The scope of this thesis in terms of strain gauges is limited to the resistive type strain sensors. The principle of strain sensing based on resistance change can be achieved via changing the resistivity coefficient, length or area using Equation 2.6 and Equation 2.7:

$$R = \frac{\rho L}{A} \tag{2.6}$$

$$\frac{\delta R}{R} = \frac{\delta \rho}{\rho} + \frac{\delta L}{L} - \frac{\delta A}{A} \tag{2.7}$$

where ρ is the resistivity coefficient, L is the length, and A is the cross sectional area of the resistor. Considering a wire shaped element sensitive to strain only in one direction, Equation 2.7 can be simplified as:

$$\frac{\Delta R}{R} = \frac{\Delta \rho}{\rho} + \epsilon(1 + 2\nu) \tag{2.8}$$

where ν is the Poison's ratio and ϵ is the strain. The gauge factor (GF) defines the sensitivity of resistance to the strain and is calculated using the following equation:

$$GF = \frac{\frac{\Delta R}{R}}{\epsilon} = \frac{\Delta \rho}{\rho \epsilon} + (1 + 2\nu) \tag{2.9}$$

In this equation, the third term is a function of piezoresistivity coefficients π and stress tensor T that the piezoresistive element is exposed to and is calculated by the following equations [32]:

$$\frac{\Delta \rho_{ij}}{\rho} = \sum_{k,l} \pi_{ijkl} T_{k,l} \text{ with } i, j, k, l = 1, 2, 3 \tag{2.10}$$

For metal gauges, the piezoresistivity coefficients are close to zero and therefore the gauge factor is limited to the range of 1.4 to 2.0. However, semiconductor materials have significantly high piezoresistivity coefficients [33] leading to the theoretical gauge factor as high as 175 (substituting $-102.2 \times 10^{-11} Pa^{-1}$ for the piezoresistive coefficients of (100) n doped silicon for longitudinal direction [34] and Poison's ratio of 0.28 and young modules of 169 GPa [35]). In this study, the piezoresistive material is made of polysilicon, and the exact piezoresistivity

coefficient is not known. However, in literature, the piezoresistive coefficient of the polysilicon is reported to be approximately half of that of the single crystal silicon with the same doping concentration [36]. It is also noted that polysilicon properties depend on the grain size, grain crystal orientation and the bonding between the grains [37].

MEMS based strain sensors use semiconductor materials and have advantages such as miniaturization, low power functionality, and CMOS (Complementary Metal–Oxide–Semiconductor) integration; however, since the sensors are bonded to the host structure through the silicon substrate, the strain transfer is influenced by packaging. Moradi and Sivoththaman [38] discuss that the stiff substrate significantly influences the gauge factor. The authors numerically showed that the trenching the silicon substrate around the strain element maximizes the strain transfer. The strain transfer to silicon substrate can be improved further by the eutectic bonding method developed by Sosnowchik et al. [39]. The other potential solution proposed by Kim et al. [29] is to separate the silicon strain sensor from the substrate for direct bonding. While the approach increases the strain transfer significantly, it is not practical for the SHM applications due to fragility of the silicon layer.

Another challenge of semiconductor based strain sensors is that they have high temperature sensitivity due to the temperature dependent piezoresistive property [40]. The temperature dependence can be reduced via increasing the dopant concentration [30] which also results in reduction of the sensitivity simultaneously. In order to compensate for the reduction in the sensitivity, which is caused by increasing the dopant concentration, Mohammed et al. [30] designed microstructure configuration with geometric features as strain riser points in order to

amplify the strain level that the sensing element is exposed to. The design layer can be modified further with wide band-gap semiconductors such as silicon carbide or diamond like carbon for harsh environments [41].

2.5 MetalMUMPs Manufacturing Method

There are three common methods to manufacture MEMS devices: bulk micromachining, surface micromachining and LIGA. Bulk micromachining is based on machining the substrate, typically single crystal silicon, to produce the intended microstructure. Surface micromachining consists of materials in the form of thin layers. Usually the main purpose of the substrate is the foundation for the MEMS structure and very few processes may affect the geometry of the substrate. Other processes which may be used in a MEMS process include but are not limited to doping, wafer cleaning and wire bonding. Another MEMS manufacturing process is called LIGA (Lithographie, Galvanoformung, Abformung which is German for: Lithography, Electroplating, and Molding) which provides high aspect ratio (ratio of thickness of the structure to the minimum feature width).

The MetalMUMPs are LIGA like micro-fabrication processes, which provide relatively high aspect ratio. The MetalMUMPs have some specific features, which differ from similar processes like PolyMUMPs. The main feature of the MetalMUMPs is a thick electroplated nickel. A doped polysilicon layer is another layer, which can be utilized as a microstructural layer or electrical connection. Silicon nitride is used as the electrical isolation layer. Silicon oxide is utilized as the sacrificial layer. Another feature of this process is the trenching, which is defined

as etching of the silicon oxide and the silicon substrate. Gold overplate can be utilized to coat the sidewalls of the nickel structures. This feature provides low contact resistance.

MetalMUMPs provide specific thickness for each layer. That sets a limit on the device design. Other than the thickness there are other limitations such as the gap between the structures or the minimum width of a structure. Design Rule Checking or DRC is used to ensure that the design follows the design rules of the MetalMUMPs.

The procedure includes the following manufacturing steps; however, it is not necessary to use all the steps in a design.

1. A high resistivity (<4000 Ωcm) n-type (100) silicon wafer forms the substrate.
2. A 2 μm thick layer of silicon oxide (SiO_2) is grown on the surface of the wafer as an insulator.
3. A 0.5 μm layer of silicon oxide (SiO_2) is deposited on top of the previous layer. This layer may be used as the sacrificial layer for the trenching.
4. A 0.35 μm layer of low stress silicon nitride (Si_3N_4) is deposited as the one of the protective layers for polysilicon structures. Also this layer is used as a part of mechanical structure and as an insulator for the electrical circuit.
5. A 0.7 μm layer of polysilicon is deposited. This layer has the resistivity coefficient 22 Ω/sq. This layer also has the dopant type and level of phosphorous (n-type) and $8 \times 10^{-15} cm^{-3}$, respectively.

6. Another 0.35 μm layer of silicon nitride (Si_3N_4) is deposited on the polysilicon layer. One of the features designed for this layer is the opening windows in order to provide the electrical connection between the metal layer and the polysilicon layer.

7. A 1.1 μm layer of silicon oxide is deposited as the second sacrificial layer which is used to release the metal layer.

8. A thin layer of anchor metal (Cr and Pt) is deposited in order to generate better adhesion between the metal layer and the polysilicon layer.

9. A thin layer of plating base metal (500 nm Cr protected by a thin Ti layer) is deposited in order to generate better electrical connection.

10. A 20 μm layer of nickel is deposited as the main structural layer.

11. A 0.5 μm layer of gold is deposited on the nickel layer in order to provide a suitable pad material for wire bonding.

12. A 1-3 μm layer of gold is plated on the top and the sides of the metal layer where selected through a patterning mask. The purpose of this layer is to provide low contact electrical resistance.

13. The final manufacturing steps include etching of sacrificial layers and etching the silicon substrate to form a 25 μm deep trench using KOH. The purpose of trenching is to provide better thermal and electrical isolation.

14. The wafers are diced with areas as 1 cm x 1 cm or 0.5 cm x 0.5 cm.

More details on this procedure can be found in the MetalMUMPs design handbook provided by MEMSCAP [42].

The following features are utilized in this study to manufacture the AE and strain sensors:

(a) Electroplated nickel is the primary structural material and electrical interconnecting layer. The thickness is 20 μm, which allows designing vertically elevated microstructures.

(b) Doped polysilicon can be used for resistors, additional mechanical structures, or cross-over electrical routing. Doped polysilicon isolated into two silicon nitride layers is used as the strain gage in this study.

(c) Two layers of silicon nitride are used as electrical isolation layers. The second silicon nitride layer between doped polysilicon (stationary layer) and electroplated nickel (freely vibrating layer) significantly reduces the stiction problem.

(d) Deposited oxide is used for the sacrificial layer.

(e) A trench layer in the silicon substrate is incorporated at the selected locations for additional thermal and electrical isolation and to increase the strain transfer.

(f) Gold overplate can be used to coat the sidewalls of the nickel structures with a low contact resistance material. This is the ideal case for ohmic contact switches.

Figure 7 shows the cross section of metalMUMPS layers and potential microstructure geometries with a trench for reducing substrate resistance. The process, masks, and layers are adequate to design and manufacture three sensors (i.e., AE, strain gage, and accelerometer) integrated on a single device.

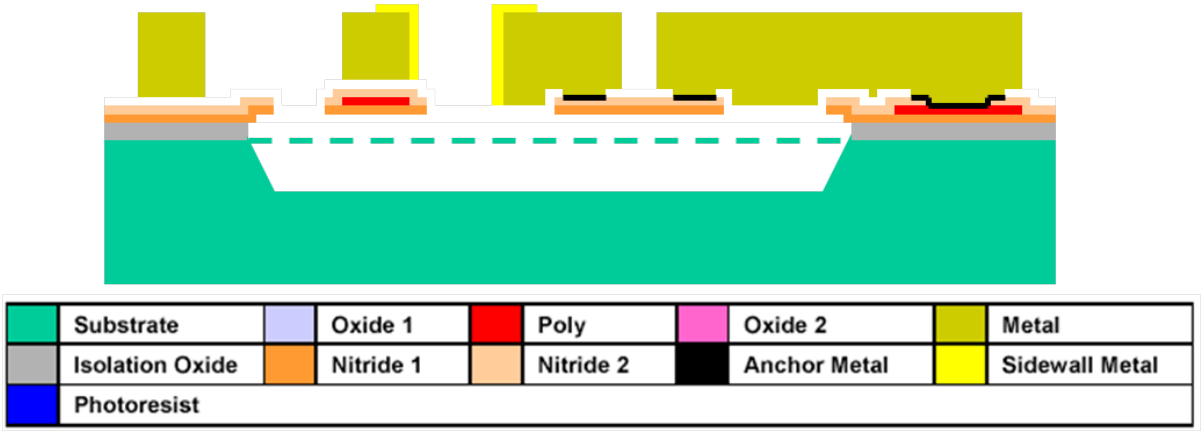

Figure 7. Schematic of the etched and trenched form of MetalMUMPs layers (source: www.memscap.com)

CHAPTER 3

MEMS OUT-OF-PLANE AE SENSORS

The content of this chapter was previously published as "MEMS acoustic emission transducers designed with high aspect ratio geometry" in the journal of smart materials and structures with my advisor, Dr. Ozevin, as the co-author [1], also partially published as "In-Plane MEMS Acoustic Emission Sensors Development and Experimental Characterization" in the "Proceedings of the 2013 Annual Conference on Experimental and Applied Mechanics" with my advisor, Dr. Ozevin, as the co-author [2] .

3.1 Introduction

This chapter begins with the design parameters and the final layout of the out-of-plane (OOP) MEMS AE sensors. The manufacturing steps to reach the intended microstructure geometry are presented. The analytical equations and numerical models utilized in the design process are discussed. Finally, the experimental characterization of the OOP MEMS AE sensors is presented in comparison with the analytical and numerical results.

3.2 Layout and Design Parameters

The transduction principle of the sensors presented in this chapter is the capacitance change due to the varying gap between two electrodes under vibration in the –z direction. The sensor design includes two microstructural layers to form a parallel plate capacitance. One of the layers is made of a freely vibrating thick metal (20 μm nickel + 0.5 μm gold), which resonates

at a particular frequency with a narrowband response. This microstructural layer acts as the mass of the spring-mass dynamic system with four suspending arms acting as the spring of the system, which are anchored to the insulated substrate. The geometry of the spring elements defines the stiffness, and the geometry of microstructural layer forms the mass of the system. Mass and stiffness are controlled in order to tune the sensor response to the target frequency with the assumption that the system behaves as a single degree of freedom system in the normal direction to the plate surface. The target frequencies are in the range of 50 kHz and 200 kHz. Two sensors are designed on the MEMS device: (1) near 60 kHz and called S1 sensor, (2) near 150 kHz and called S2 sensor. Multiple unit cells are connected in parallel to increase the total capacitances of the sensors. Each sensor is formed by 55 unit cells, which are identified by two constraints: one dimension as 5 mm in order to place other sensors on the device area of 10 mm x 10 mm and total capacitance targeted as higher than 20 pF (pico Farad). The sensor sensitivity is directly proportional to the total capacitance. It is assumed that the mechanical properties of the combined geometry are the same as the single unit cell. The bases of the this assumption are twofold: (1) the sizes of individual unit cells are significantly smaller than the wavelength of the excitation signal; (2) each unit cell has anchorage points outside the mass, and they are connected through the anchorage points. Therefore, each unit cell vibrates under loading independently. Figure 8 indicates the electrodes connected to each capacitive layer and particular connection pads. There is a redundant moving electrode pad for the case of malfunctioning wirebonding. All the unit cells are electrically connected to combine their

current changes under static or dynamic motion. The overall area of the each sensor is about 2.5 mm x 5 mm.

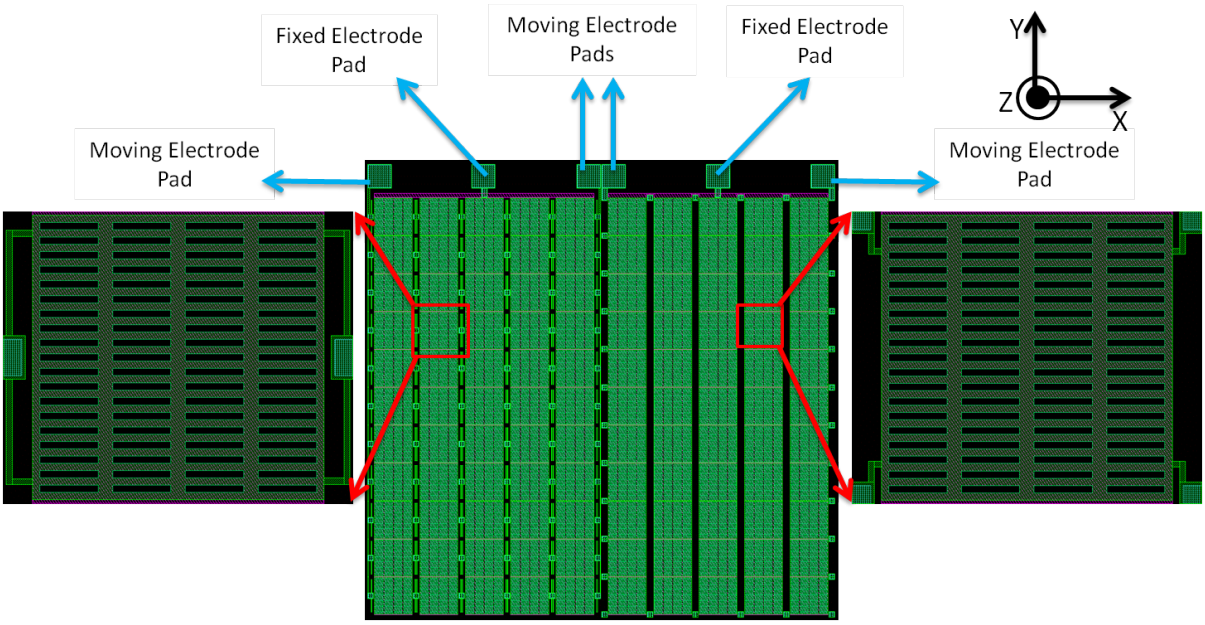

Figure 8. CADENCE plots indicating the unit cells, combined sensors and connection pads for the AE sensors

Figure 9 shows the dimensions of two sensors highlighted on the SEM images of individual cells. The comparison of the design (Figure 8) and SEM images (Figure 9) indicates that the process flows are correctly performed to manufacture the target geometry. The mass dimensions of two sensors are the same as 390 $\mu m \times$ 400 μm while the spring lengths are modified to control

the fundamental resonant frequency as shown in Figure 9. Low frequency design requires longer springs to lower the stiffness value. Etch hole strips with the dimensions as 80 μm long and 10 μm wide are created to reduce the squeeze film damping [26]. Each unit mass has an array of 4 x 10 etch hole rectangles.

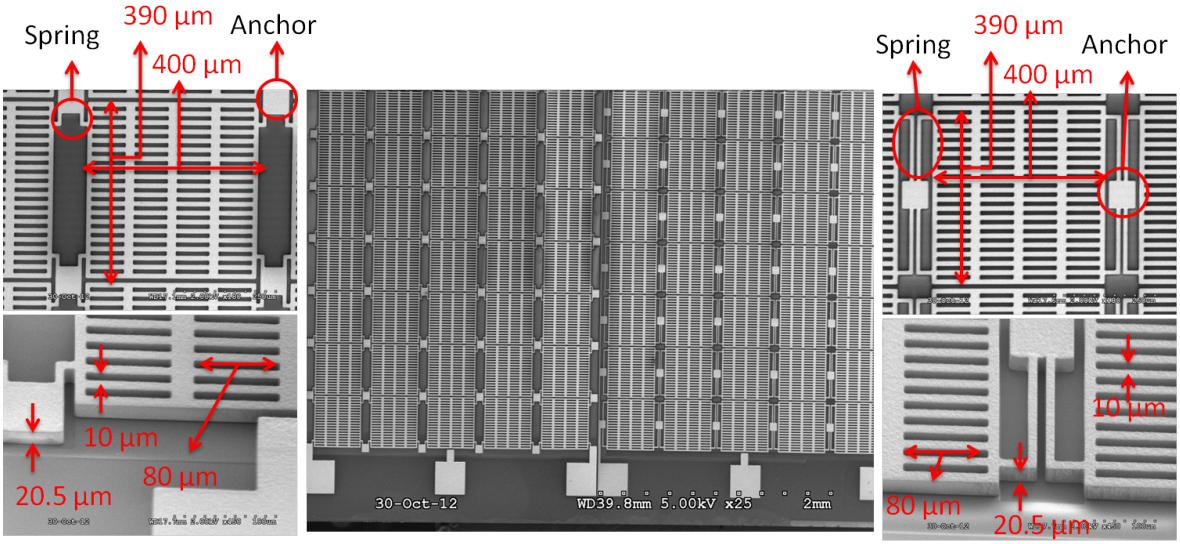

Figure 9. SEM images of single unit cell and the array with the dimensions of low frequency S1 design (right) and high frequency S2 design (left)

The moving mass acts as one of the electrodes in the capacitance. The other electrode is made of a thin layer (0.7 μm) of n-doped polysilicon deposited beneath a 0.35 μm of silicon nitride layer. The total gap between polysilicon layer (stationary layer) and nickel layer (freely

moving layer) is 1.45 μm (1.1 μm air + 0.35 μm silicon nitride). While the presence of silicon nitride layer increases the gap between two layers, which reduces the sensitivity, the potential of the stiction phenomenon is eliminated. The polysilicon layer is in the form a rectangle with the dimensions of 390 $\mu m \times$ 400 μm, similar to the nickel layer.

3.3 Manufacturing Steps

The manufacturing layers and processes to design the OOP MEMS AE sensors discussed in this chapter are described below and shown in Figure 10:

1. A highly resistive n-type (100) silicon wafer forms the substrate.
2. A layers of silicon oxide (SiO_2) is formed for the total thickness of 2.5 μm. This layer is used as the insulation layer between the substrate and polysilicon layer which forms the fixed electrode of the capacitive sensor.
3. A thin layer (0.35 μm) of silicon nitride (Si_3N_4) is used to provide an additional layer of insulation.
4. Polysilicon layer is deposited on the nitride layer. The thickness of this layer is 0.7 μm, and it is patterned as the fixed electrode of the capacitance. This layer is doped and has the electrical square resistivity of 22 Ω/sq.
5. The second layer of silicon nitride is deposited on polysilicon layer to be used to eliminate the stiction phenomenon.

6. Another silicon oxide layer is deposited that functions as the sacrificial layer, and etched at the end of the process to release the metal layer. The silicon oxide layer is 1.1 μm thick and patterned to create the etch windows.
7. Very thin layers of anchor metal and plating base are deposited for better adhesion and electrical connection between the metal layer and the nitride layer or the poly layer. Without this layer, the metal layer may peel off during the manufacturing process.
8. Finally the metal layer is deposited through an electroplating of 20 μm nickel and a 0.5 μm of gold. The gold coat enhances the wire bonding procedure at the connection pads and reduces the corrosion potential of nickel layer. The metal layer is patterned to form the spring and mass system.
9. The sacrificial layer is removed in order to release the metal layer.
10. The wafers are diced to form 1 cm x 1 cm device size.
11. Each die is mounted in a ceramic package with epoxy. Then each pad is wire bonded to one of the pins of the package.

Figure 10 provides the basic steps of micromachining using the cross sectional view of the design and the numbers in the figure represent the manufacturing steps described above. The thickness of each layer is controlled by the process while the planer view is controlled by the design as shown in Figure 8 and Figure 9 to create resonating modes in –z direction in the range of 50 kHz and 200 kHz.

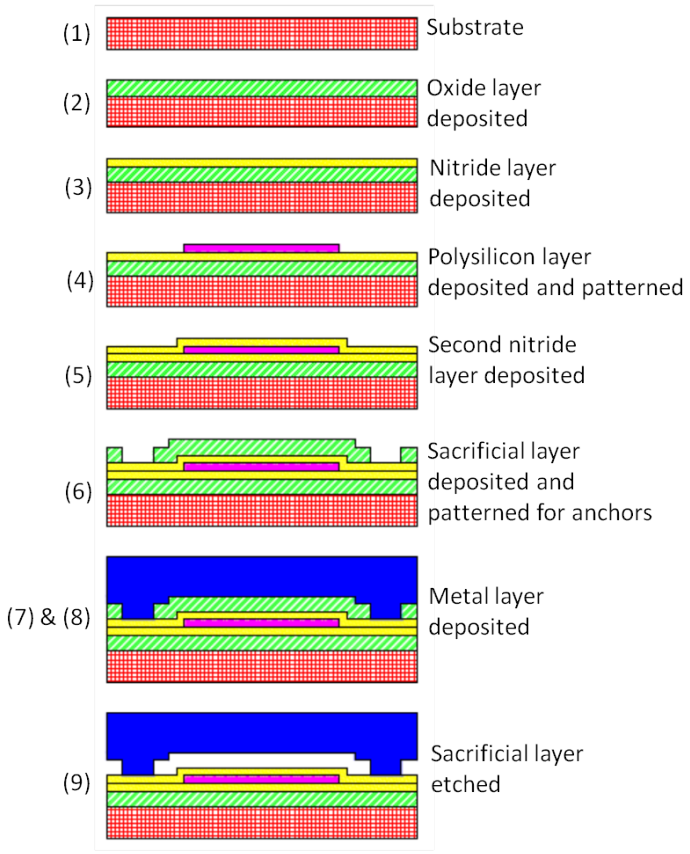

Figure 10. Summary of micromachining steps to design MEMS OOP AE sensors

3.4 Analytical and Numerical Modeling of OOP MEMS AE sensors

The variables calculated using analytical and numerical methods include fundamental resonant frequency, capacitance, capacitance change with DC voltage and damping.

3.4.1 Resonant Frequency

The resonant frequency is obtained with single degree of freedom assumption at –z direction and calculated by Equation 2.5. The unit mass value is 23 μg. The spring dimensions are 140 μm and 32 μm for the S1 design, 24 μm and 14 μm for the S2 design. Each spring has the cross sectional area of 20.5 $\mu m \times$ 8 μm. With the assumption that there is no rotation at the connection points of spring elements and mass, which is a valid assumption for the rigid body motion of the mass, the stiffness values of the S1 and S2 sensors are calculated as 2.4 kN/m and 200 kN/m, respectively. The first modal frequencies of the S1 and S2 sensors at the –z direction result in 51 kHz and 464 kHz, respectively.

In addition to the analytical solutions of the problem, the sensor geometry is modeled using COMSOL Multiphysics software (COMSOL 4.2a). The eigenfrequency analysis provides the fundamental mode shapes and the frequencies as shown in Figure 11. The low frequency design has analytical result as 51 kHz based on single degree of freedom idealization while the finite element result is 88 kHz. The analytical and finite element solutions of the high frequency design are 464 kHz and 205 kHz, respectively. The idealized rigid body assumption provides sufficiently accurate result for the preliminary design of the low frequency sensor; however, the error becomes larger when the spring elements have higher stiffness value. The increased stiffness causes diaphragm motion instead of rigid body motion. Therefore, the selection of generalized displacement as the rigid body motion of the mass for the shape function becomes incorrect. The mode shapes shown in Figure 11 indicate that the low frequency design has consistent deformation in –z direction while the high frequency design has varying displacement

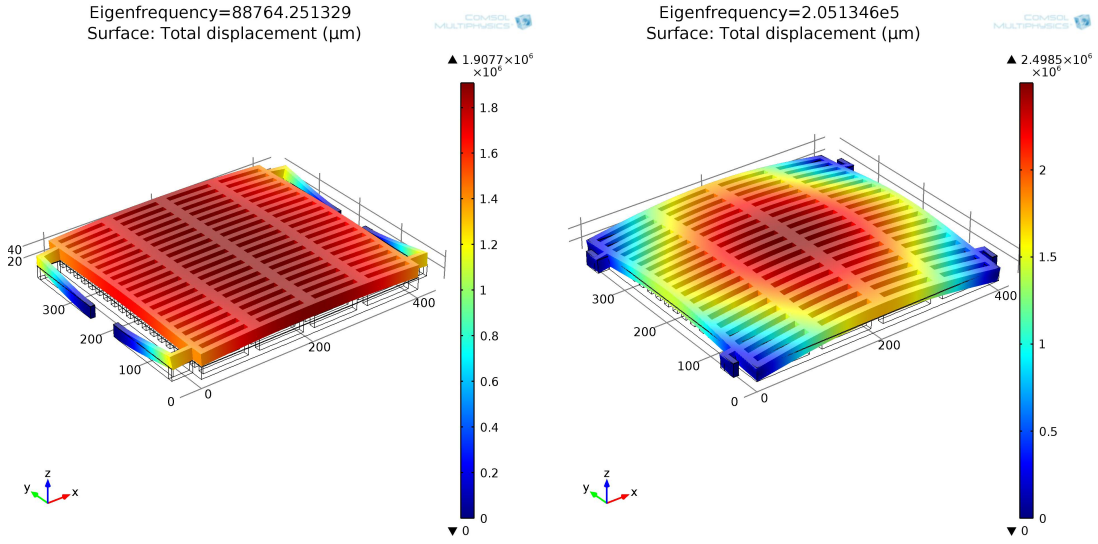

Figure 11. The out-of-plane mode shapes for the S1 sensor at 88 kHz (left) and the S2 sensor at 205 kHz (right)

values from the edge to the middle section, similar to square plate vibration. The analytical approach with the assumed mode shape does not provide an accurate prediction of the first modal frequency for the S2 sensor. As there is no close form solution for the boundary conditions of the S2 sensor, numerical solution is needed to predict the design frequency of the sensor.

3.4.2 Capacitance and sensitivity

The capacitance C_0 of parallel plates is calculated using Equation 2.3 [43]. The capacitance is formed by polysilicon and nickel, which are separated by air ($d_{air} = 1.1\mu m$) and silicon nitride ($d_{SiN} = 0.35\mu m$). The total capacitance is calculated by:

$$C_0 = \frac{1}{\frac{1}{C_{SiN}} + \frac{1}{C_{air}}} = \epsilon_0 A \frac{1}{\frac{d_{SiN}}{\epsilon_{SiN}} + d_{air}} \tag{3.1}$$

where ϵ_{SiN} is the relative permittivity of silicon nitride which is 7.5. When the moving electrode displaces -z towards the fixed electrode, the air gap changes from d_{air} to $(d_{air} - z)$ that causes capacitance change as:

$$C_2 = \frac{1}{\frac{1}{C_{SiN}} + \frac{1}{C_{air}}} = \epsilon_0 A \frac{1}{\frac{d_{SiN}}{\epsilon_{SiN}} + (d_{air} - z)} \tag{3.2}$$

From the Taylor series expansion and defining $a = (\frac{d_{SiN}}{\epsilon_{SiN}} + d_{air})$ the capacitance expression is written as:

$$C_2 = \epsilon_0 A(\frac{1}{a} + \frac{z}{a^2} + \frac{z^2}{a^3} + \cdots) \tag{3.3}$$

By substituting C_2 into the electrical force, the electrical force equation [43] can be written as under DC bias voltage using the first two terms of the Taylor series expansion as:

$$F_{elec} = -\frac{d}{dz}(\frac{CV_{DC}^2}{2}) = -\frac{V_{DC}^2}{2}\epsilon_0 A(\frac{1}{a^2} + \frac{2z}{a^3}) \tag{3.4}$$

The displacement z of the moving electrode is calculated through the force equilibrium of the electrical and mechanical forces as:

$$z = \frac{V_{DC}^2 \epsilon_0 A(\frac{d_{SiN}}{\epsilon_{SiN}} + d_{air})}{2(k_{mech}(\frac{d_{SiN}}{\epsilon_{SiN}} + d_{air})^3 - V_{DC}^2 \epsilon_0 A)} \tag{3.5}$$

where K_{mech} is the mechanical stiffness of the microstructure and calculated from the geometry and mechanical properties of the spring elements. Substituting z into the capacitance equation C_2, the capacitance change under constant bias voltage is obtained. For unit DC voltage, the displacement value is 75 pm and the capacitance change per unit cell of S1 sensor is $6.23 \times 10^{-17} F$. If there were no silicon nitride layer, the values would be 81 pm and $7.35 \times 10^{-17} F$. Because of the relative permittivity of silicon nitride, the increase in gap between the electrodes from 1.1 μm to 1.45 μm does not influence total capacitance change of the sensor significantly. Using the electrical module of COMSOL, the capacitance of each sensor is identified. The electrical model includes three layers as polysilicon, silicon nitride and nickel with defining the electrodes as polysilicon (ground) and nickel (terminal). The silicon nitride and nickel are separated by air. The thicknesses for polysilicon, silicon nitride, air and nickel are 0.7 μm, 0.35 μm, 1.1 μm and 20 μm, respectively. A box of air is formed around the geometry in order to enable the software to create the electrical field and solve for the electrical properties including the capacitance. 1 V_{DC} is applied to the terminal (nickel layer). The capacitance value of S1 and S2 sensors is calculated as 45.5 pF while the analytical result is 35.3 pF. The numerical 3D model considers the fringe fields; therefore, the resultant capacitance is higher

TABLE IV

MATERIAL PROPERTIES USED IN NUMERICAL SIMULATIONS

Materials	Density ρ (kg/m^3)	Young's Modulus E (GPa)	Poisson's Ratio ν	Relative Permittivity ϵ_r
Ni	8900	219	0.31	
Au	19300	70	0.44	
Air	From table based on (T,P)			1
Poly-Si	2320	158	0.22	4.5
Si3N4	3100	245	0.23	9.7

than the assumption of simple 2D parallel plate capacitance [43]. The COMSOL has some build material with predefined physical and electrical properties. These properties are changed with the values provided with the manufacturer where available as indicated in Table IV.

3.4.3 Damping

Fluid motion in microstructural geometries has been explained by Navier-Stocks (NS) equation. In this equation, there are several terms to quantify the loss of energy through viscous damping. If the fluid is a narrow film between solid boundaries which are moving toward or away from each other, the loss of energy is called squeeze film damping. The squeeze film damping can be reduced by decreasing atmospheric pressure (i.e. vacuum packaging), increasing the size and frequency of etch holes to provide the flow of air through the holes and increasing the gap between the electrodes to reduce the pressure. Vacuum packaging has reliability problem for long-term usage due to outgassing, and is not a cost efficient approach. In this study, rectan-

gular etch holes, adapted from Harris [26] are implemented to reduce the squeeze film damping; therefore, the sensors exhibit resonance behavior in atmospheric pressure. The damping coefficient $C_{squeeze-film}$ can be simplified as the damping ratio ζ as shown in Equation 3.7 [44]. The damping is also represented using the dimensionless number as the Quality (Q) factor as shown in Equation 3.8.

$$C_{squeeze-film} = (\frac{6hb^2}{a^3} + \frac{b^3}{g^3})\eta L \tag{3.6}$$

$$\zeta = \frac{C_{squeeze-film}}{2\sqrt{km}} \tag{3.7}$$

$$Q = \frac{1}{2\zeta} \tag{3.8}$$

where h is the moving plate thickness, a is the hole thickness, b is the thickness of a bar, g is the gap between the electrodes, L is the length of the beams, η is the viscosity of air, and ζ is damping ratio. Table V compares the analytical calculation of the damping and the quality factor of the MEMS sensors designed in this study in comparison with the literature. There is an improvement in the Q factor of the design in this study, which increases the sensor sensitivity proportionally.

The squeeze film damping equation may vary depending on several factors: design parameters (i.e. the thickness of the film, size of the moving plates, the presence of etch holes and their shape, distance and size, structural properties such as frequency, acceleration and stiffness of springs), surface condition, environment parameters such as temperature and pressure [45]. The analytical approach adapted in this study considers no-slip condition. The factor

TABLE V

COMPARISON OF $C_{SQUEEZE-FILM}$ AND Q WITH THE LITERATURE

Sensor	$C_{squeeze-film}(\mu Ns/m)$	Q
Wright [3]: OOP1	1.05	82.1
Wright [3]: OOP2	1.55	53.8
Current Study: S1	88	114
Current Study: S2	88	264

that measures the applicability of no slip condition is known as the Knudsen number K_n. This number specifies the rarefield gas condition and limits the use of slip condition instead of common no-slip condition, typically implemented in numerical programs. The Knudsen number is calculated by [45]:

$$K_n = \frac{\lambda}{h} \tag{3.9}$$

where λ is the mean free path of the gas and is a function of temperature and pressure and h is the air gap. For the sensors developed in this study, the Knudsen number is about 0.06, which is in the range of slip condition ($0.001 < K_n < 0.1$). Neglecting this condition may lead to significant errors in the damping calculations. Considering the factors and conditions affecting the analytical model, numerical model is expected to lead to a more precise estimate of the quality factor, which may result in a better prediction of sensor behavior.

3.4.4 Summary of Analytical and Numerical Models

Table VI summarizes the analytical and numerical results. The difference between the analytical and numerical capacitance are due to the fringe effects. As discussed above, the analytical approach as rigid body motion for high frequency design has higher error due to the plate-like behavior of the mass. The computations include the design geometry and the material details while two main phenomena are not considered: damping and residual stress. The damping affects the resonant frequency and the sensitivity of the sensors. The residual stress in the metal layer caused by manufacturing process may deform the structural layer and change the gap between two electrodes. Residual stress may influence both resonant frequency through changing the stiffness and capacitance. The manufacturing method used to deposit the metal, electroplating, leaves 100 MPa residual stress in the structure (provided by the manufacturer). The level of the residual stress is less than many other deposition techniques such as Electron Beam Evaporation causing up to 1 GPa residual stress [46]. Both phenomena affect the experimental results. Their influences on the measured values are discussed in the next section.

3.5 Experimental Characterization

3.5.1 Electromechanical Characterization

The sensor preparation procedure includes mounting the device on a ceramic package with two-part epoxy and wirebonding. The capacitance and admittance of each sensor are measured using HP 4294A Impedance Analyzer. The capacitance curve is obtained through sweeping a range of DC voltages with 500 mV alternative voltage at 1 MHz. Figure 12 shows the

TABLE VI

THE COMPARISON OF ANALYTICAL AND NUMERICAL RESULTS

Sensor	Frequency (kHz)		Capacitance (pF)	
	Analytical	Numerical	Analytical	Numerical
S1	50	88.8	35.3	45.5
S2	464	205		

capacitance curves of two sensors together with the second order polynomial curve fit acquired by using Matlab (2011b). The static capacitances are measured as 62 pF and 59 pF for the S1 and S2 sensors, respectively. The numerical value as 45.4 pF is sufficiently close to the experimental values. The sensors exhibit parabolic C-V relationship, which agrees with the theory.

The admittance values in the form of magnitude and phase are obtained through sweeping a range of frequencies at constant DC bias voltage as 10 V and 20 V for the S1 and S2 sensors, respectively. As shown in Figure 14, when the resonance frequency of the sensor and the sweep frequency match, the admittance of the sensor is amplified (both magnitude and phase). The resonance is clearly seen in the phase results due to smaller range for –y axis as compared to the magnitude values. The admittance equation is obtained from the equivalent circuit model (as shown in Figure 13) of the capacitive sensor considering certain amount of resistance as:

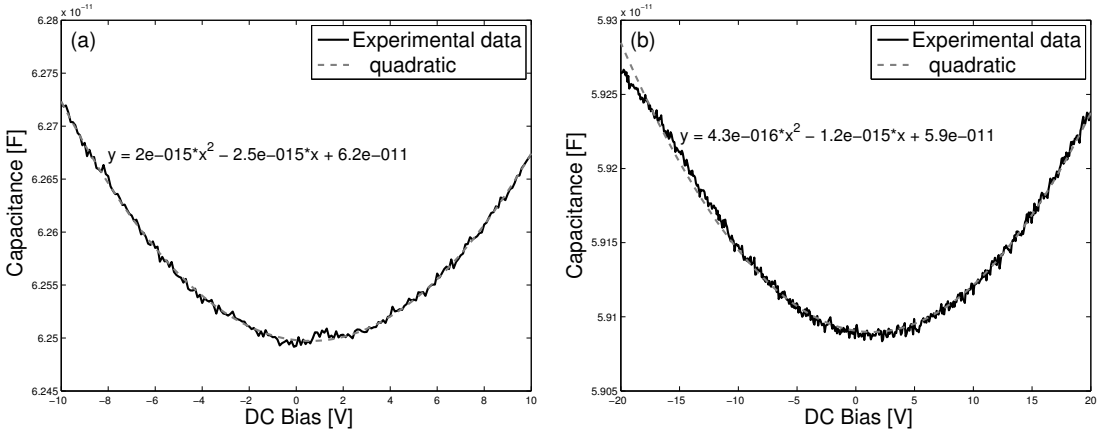

Figure 12. C-V curves and parabolic curve fits for (a) the S1 sensor, (b) the S2 sensor

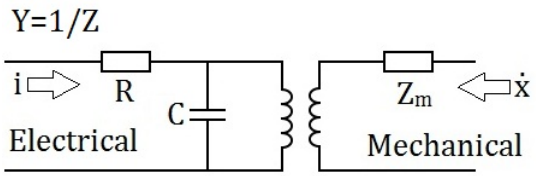

Figure 13. The equivalent circuit model

$$Y = \frac{1}{R + \frac{1}{j\omega C_0 + \frac{1}{m}(\frac{C_0 V_{dc}}{g})^2 + \frac{j\omega}{\omega_0^2 + \omega^2 + \frac{j\omega\omega_0}{Q}}}} \tag{3.10}$$

The measured values of the sensors are compared with the numerical results in Table VII. The measured capacitances are slightly higher than the calculated capacitances. A consistent

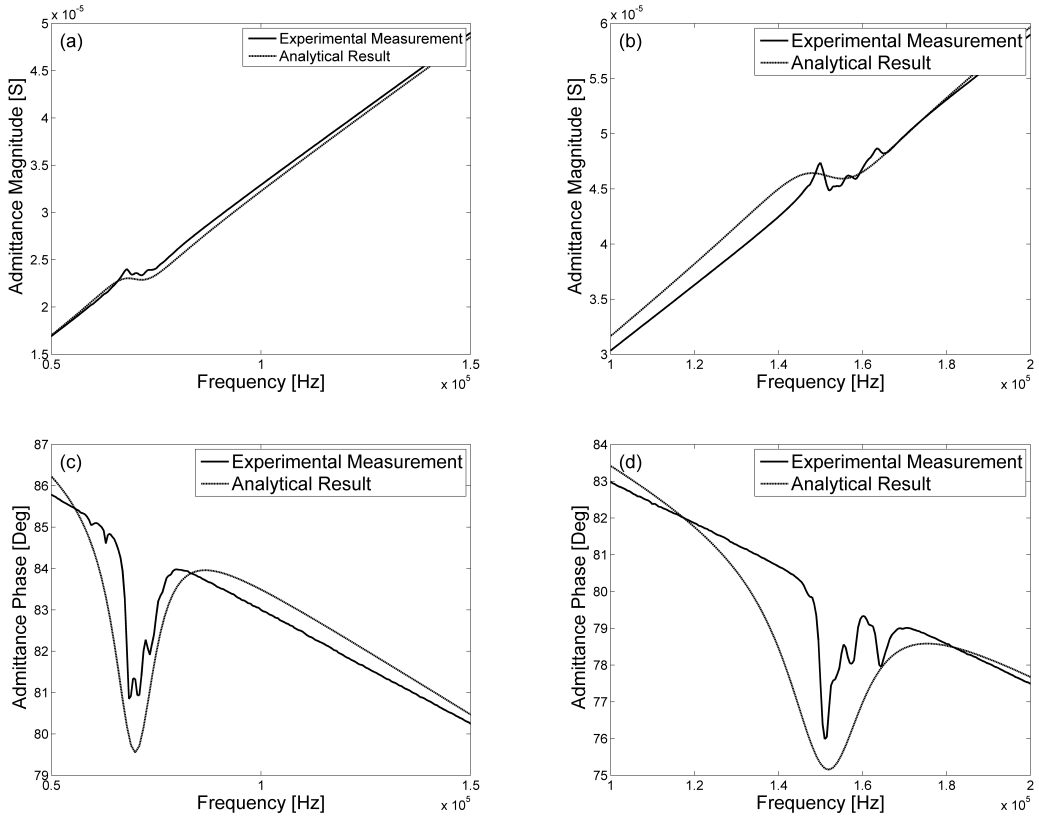

Figure 14. Admittance measurement results; (a) magnitude of the S1 sensor, (b) magnitude of the S2 sensor, (c) phase of the S1 sensor, (d) phase of the S2 sensor

TABLE VII

THE COMPARISON OF NUMERICAL AND EXPERIMENTAL RESULTS FOR FREQUENCY AND CAPACITANCE

Sensor Name	Frequency (kHz)		Capacitance (pF)	
	Numerical	Experimental	Numerical	Experimental
S1	88.8	68	45.5	62
S2	205	149	45.5	59

shift to lower frequencies from the calculated values is observed for both sensors. The difference may be because of variations in geometry and material properties caused by micromachining, approximations and residual stress.

The measured values have been used to recalculate some physical parameters such as air gap quantified as 1.168 μm, which is close to the actual value as 1.1 μm.

3.5.2 Mechanical Characterization

The directionality of sensors is studied using a point source created by a short-pulse laser in the sensing direction –z (out-of-plane) and the other directions in –x or –y (in-plane). Figure 15 shows the test setup and modes of loading. The sensor package is attached to a steel block in order to place it in the line with the laser beam. Nd:Yag Q-switched laser is mounted on an optical breadboard which provides control on the laser beam direction and location. The laser specifications are 50 mJ laser energy, 4-5 nsec rise time and 3 mm beam diameter. The ceramic package is made of an aluminum oxide alloy known as Kyocera A440 (Black). Aluminum oxide's reflective index for the 90° incidence angle is approximately 100% [47]. Since the laser source

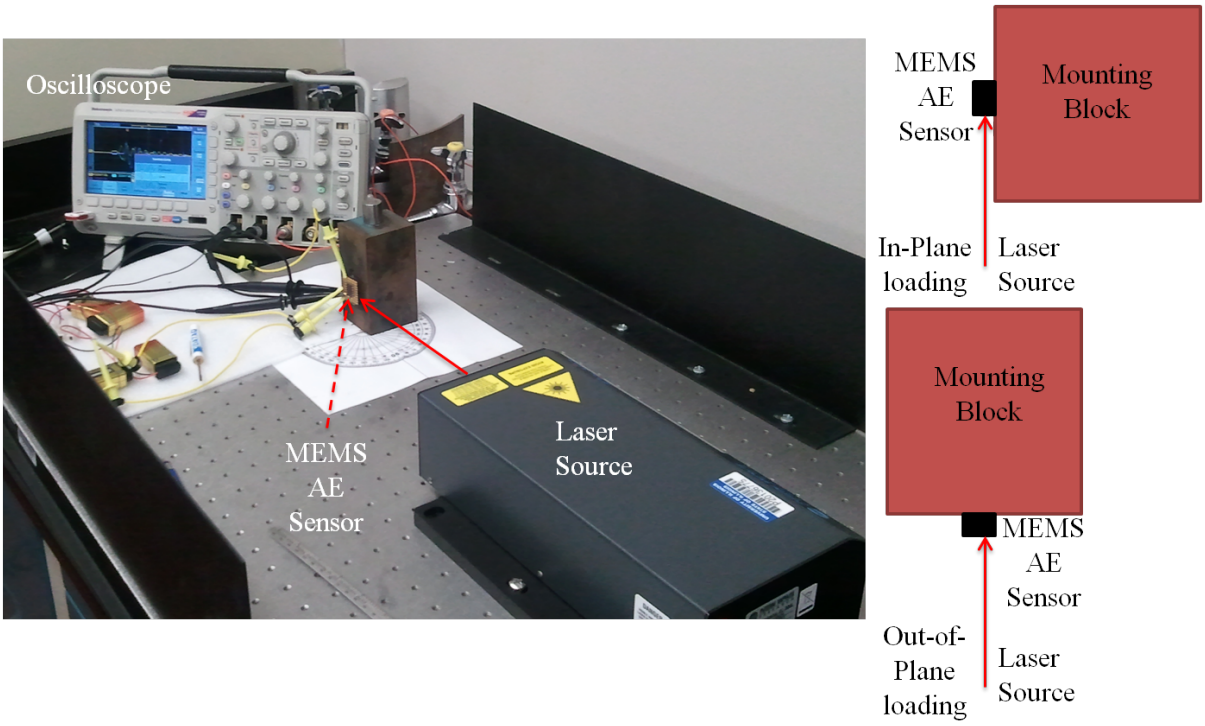

Figure 15. Laser test setup and loading directions

created is in non-ablation zone, the short pulse laser source introduces a Heaviside dipole force normal to the laser beam and creates wideband thermoelastic stresses [48]. The wave amplitude parallel to the laser beam is considerably higher than the wavefield in the vertical direction [49]. Therefore, the directional response of the sensor can be obtained through changing the direction of the laser beam as shown in Figure 15.

Figure 16 illustrates the waveform histories of two sensors with the laser source applied in –z and –x directions. The laser power for –x direction testing is increased from 66% to

75% of total laser power in order to capture the pulse in the in-plane direction above the electronic noise level. The laser-source simulation experiments clearly show that the sensors are sensitive only to –z direction. One of the disadvantages of the piezoelectric sensors is that they response to any wave, regardless of the direction of the wave. On the other hand, MEMS AE sensors can be designed to be only sensitive to waves with one specific direction. The disadvantage of piezoelectric sensors as being responsive to any directional wave motion due to bulky characteristics is overcome with the MEMS approach. The arrivals of multiple wave reflections are clearly observed in Figure 16(b) (high frequency design) while there are overlaps for low frequency design (Figure 16(a)) due to longer wavelength. Both sensors have a well-defined resonant sensor profile with a rise time and a decay time, which is related to the sensor Q factor. The amplitude of the S1 sensor is about twice of the S2 sensor. While their total capacitance values are close, the capacitance change for the S1 sensor is higher than the S2 sensor due to softer spring elements. The applied DC voltages for the S1 and S2 sensors are 10 V and 20 V, respectively.

3.5.3 MEMS vs Piezoelectric AE Sensors

The sensitivity and waveform signatures in time and frequency domains of the MEMS sensors are compared with the conventional piezoelectric sensors at similar resonant frequencies. The S1 sensor is compared with an R6 piezoelectric sensor, both having the resonant frequency at 60 kHz. The S2 sensor is compared with an R15 piezoelectric sensor, both having the resonant frequency at 150 kHz. Piezoelectric sensors, R6 and R15, are manufactured by Mistras Group Inc. Both sensor types are mounted on a 1 mm thick 7075 aluminum plate using vacuum

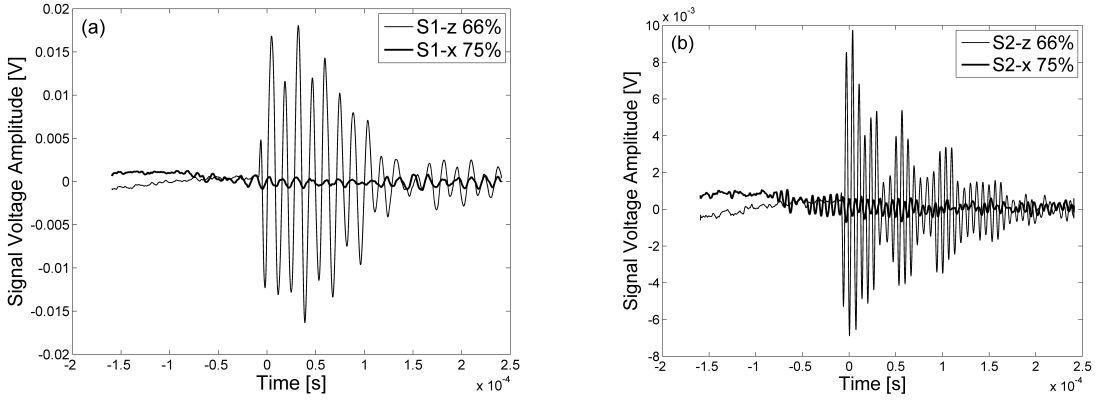

Figure 16. Directional sensitivities of (a) S1 sensor (b) S2 sensor

grease, Figure 17. The sensors are directly connected to a four-channel oscilloscope (Tektronix MSO2014) without any amplifier. The S1 sensor is powered using two 9 V batteries; the S2 sensor is powered using five 9 V batteries. The schematic of the electrical circuit used in the mechanical testing is shown in Figure 18.

Two simulation methods are implemented: ball drop and pencil lead break. The specifications of ball drop test are 3.2 mm diameter steel ball and 10 cm drop height. The force function created by the ball drop on a material is obtained by the following equation [50].

$$\begin{aligned} F &= \frac{1.14\nu_0^2}{k_1\alpha_m}\sin\frac{1.068\nu_0 t}{\alpha_m} \qquad \text{for } 0 \leq t \leq \frac{\pi\alpha_m}{1.068\nu_0} \\ F &= 0 \qquad\qquad\qquad\qquad\quad \text{for} \qquad t \geq \frac{\pi\alpha_m}{1.068\nu_0} \end{aligned} \tag{3.11}$$

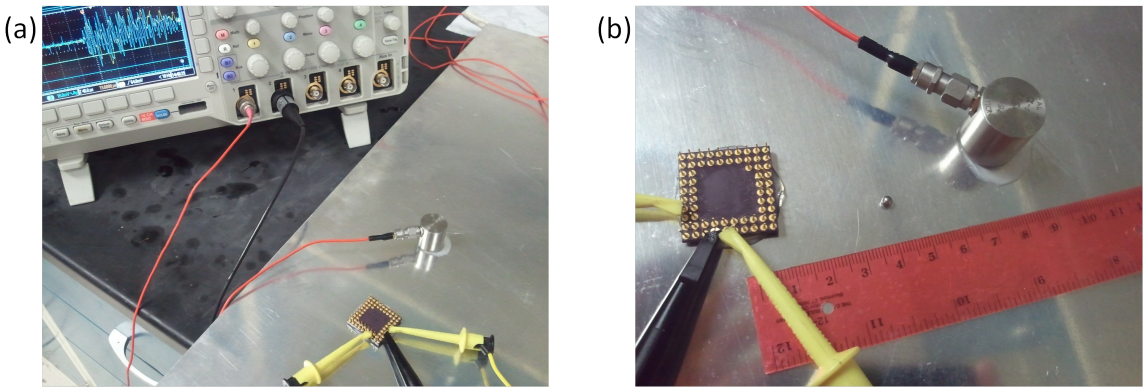

Figure 17. Ball drop impact and pencil break test setups for MEMS and piezoelectric AE sensors (a) test setup, (b) detailed close up illustration

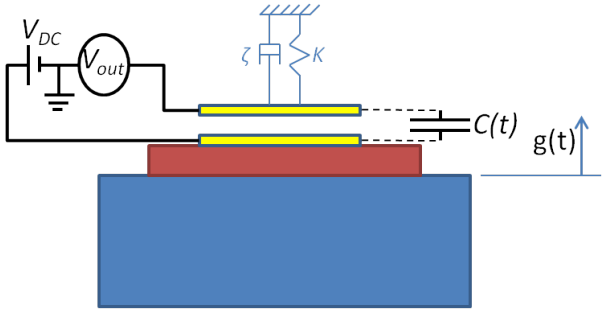

Figure 18. The electrical circuit for mechanical testing of capacitive MEMS AE sensors

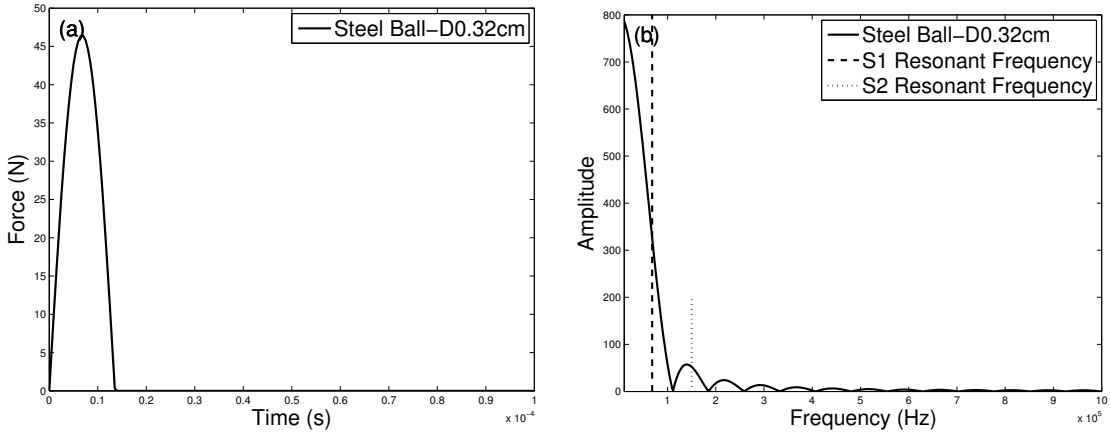

Figure 19. Ball drop impact test force (a) loading function in time domain, (b) frequency spectrum of the loading function

where $k_1 = \frac{1}{m_1} = \frac{3}{(4\pi\rho_1 R_1^3)}$ is the inverse of ball mass, ρ is density, R is radius, impact parameter is $\alpha_m = (\frac{15\pi\nu_0^2(\sigma_1+\sigma_2)m_1}{16\sqrt{R_1}})^{0.4}$, $\nu_0 = \sqrt{2gH}$ is initial relative velocity at free fall, g is the gravity constant, H is the height of fall, $\sigma = \frac{1-\nu}{\pi E}$ calculated from Hertz law of contact is relative to the Poisson's ratio, ν, and inverse of Young's Modulus, E. The force introduced to the plate by the ball drop selected in this study is calculated and plotted in Figure 19(a). Figure 19(b) indicates that the source function has higher amplitude in the frequency range of S1 sensor as compared to the S2 sensor. Therefore, the ball drop simulation is selected for testing the response of the S1 sensor.

The source function created by the Pencil Lead Break (PLB) is quantified as ramp function shown in the equation below [51].

$$\begin{aligned} F &= F_{max}(\frac{t}{t_e}) \qquad \text{for } 0 \leq t \leq t_e \\ F &= F_{max} \qquad\quad \text{for} \qquad t \geq t_e \end{aligned} \tag{3.12}$$

where F_{max} is the maximum force and t_e is the rise time, which is typically 1 μsec. The PLB simulation generates a wideband source, which is more appropriate approach for identifying the response of high frequency S2 sensor. The force amplitude is controlled by the lead diameter. In this study, the diameter of 0.7 mm pencil lead is selected for the PLB test. Figure 20(a) and 20(c) show the time domain and frequency domain responses of the S1 and R6 sensors due to ball drop test. The repeated drops indicate similar waveform signatures at each trial. The amplitude of the R6 sensor in time domain considering the summation of all the frequencies that the sensor responds is about 5 times higher than the S1 sensor. However, the MEMS sensor has a narrowband response at its resonant frequency while the R6 sensor has other frequency components than the resonant frequency, which causes a complex waveform signature. The comparison of two sensors at their resonant frequencies indicates that the MEMS and piezoelectric sensors have similar sensitivities, while the size of MEMS sensor is significantly smaller. Figure 20(b) and 20(d) show the time domain and frequency domain responses of the S2 and R15 sensors. The cumulative amplitude of the R15 is about 20 times higher than the S1 sensor. Similar to R6 sensor, the time domain response of R15 sensor is mixed with multiple frequencies. The bulk geometry of the piezoelectric ceramic without any backing material causes

internal reflections that influence the sensor output in addition to the primary resonance mode. The difference of two high frequency sensors at 150 kHz frequency is smaller. As opposed to the repeatability of the ball drop tests, the source functions of the pencil break are influenced by the angle of the pencil with respect to the plate. If the breakage is performed at nearly perpendicular to the aluminum plate, the signal of the MEMS sensor is higher than the smaller angle results. As the angle changes from 90 degrees, the source causes extensional wave mode as well while this is the insensitive direction for the MEMS sensor.

The reason of lower sensitivity measured from the S2 sensor is attributed to the signal loss at the interfaces of the MEMS package. In the current setup, the MEMS device is mounted on the ceramic package with pins down and closed with a ceramic cap using an adhesive layer around the cap. The layers that the wave needs to propagate before reaching to the MEMS sensors include a layer of vacuum grease, ceramic cap, an adhesive layer and ceramic package. Due to lower wavelength of the S2 design, wave amplitude reaching to the sensor is smaller than the S1 design. A different packaging structure can reduce the wave motion loss at the interfaces, which improves the MEMS sensor response at higher frequencies. Additionally, the package material significantly influences the sensor response. For instance, the experiments conducted on a steel structure indicate smaller amplitudes obtained from the MEMS sensors as compared to the aluminum plate test. The ceramic package is known as KY0CERA A440 with a coat of alumina. This ceramic is mainly aluminum oxide (Alumina: Al2O3), which has close acoustic impedance value (Z) to the aluminum plate. Table VIII summarizes the common acoustic impedances studied in this research. When a thin layer of aluminum oxide forms on

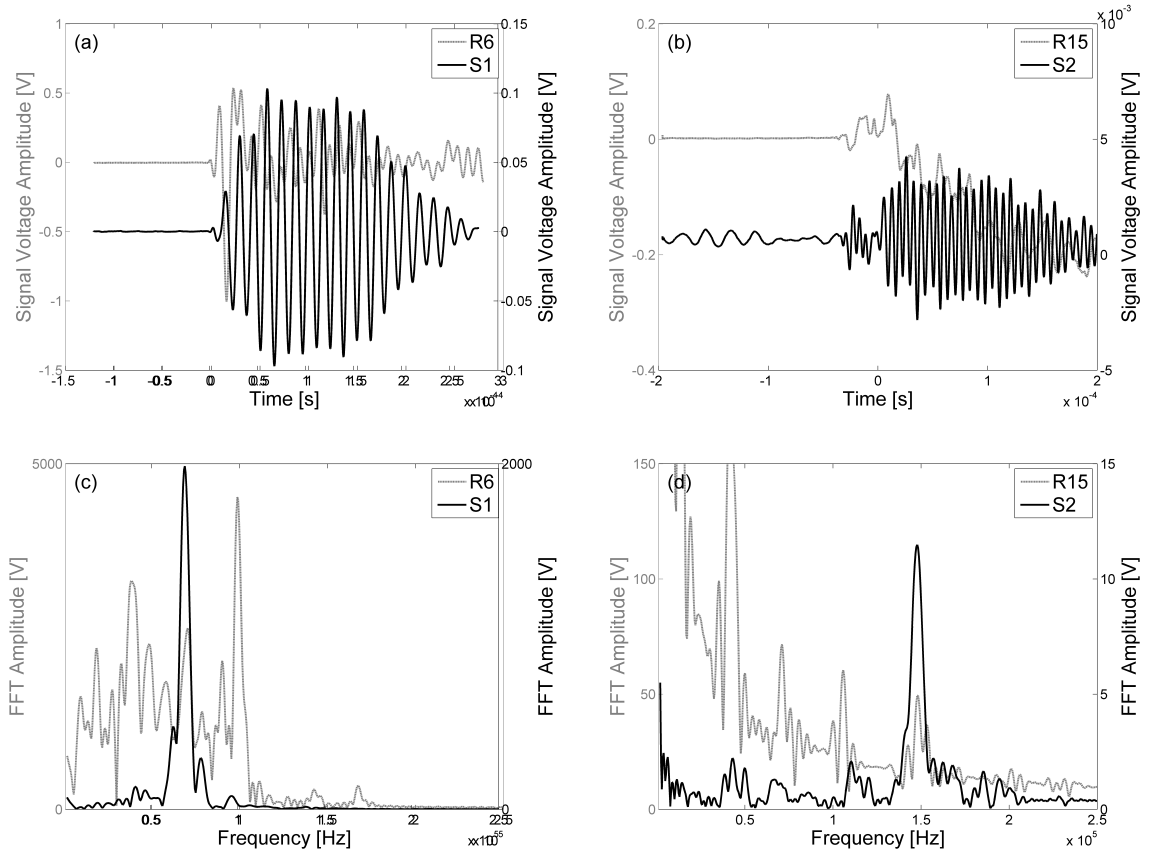

Figure 20. The comparison of MEMS and piezoelectric AE sensors (a) time domain responses of S1 and R6, (b) time domain responses of S2 and R15, (b) frequency spectra of S1 and R6, (d) frequency spectra of S2 and R15

TABLE VIII

ACOUSTIC IMPEDANCE VALUES OF SELECTED MATERIALS

Material	Acoustic Impedance Z $(g/cm^2sec \times 10^5)$
Alumina	25.5
Steel	46
Aluminum	17.1
PZT-5A	33.7

the aluminum plate, the impedances of two structures become closer. However, the acoustic impedance of steel is about twice of alumina, which causes wave motion loss at the interface.

The Q factor is measured using the half-power bandwidth method. Figure 21 indicates the crossing points at 3 dB lower than the peak amplitudes of the S1 and S2 sensors on their frequency spectra obtained from the ball drop and pencil lead break tests. The equation of the Q factor is:

$$Q = \frac{1}{2\zeta} = \frac{\omega_n}{\omega_1 - \omega_2} \tag{3.13}$$

where ω_1 and ω_2 are the lower and higher bands of the frequency spectrum for the half-power bandwidth, ω_n is the peak frequency of the spectrum.

Table IX compares the half-power bandwidth results with the analytical and admittance test results. The Q factor is obtained using the admittance test through fitting Equation 3.10 to the measured data. However, this equation has other variables than the Q factor, including

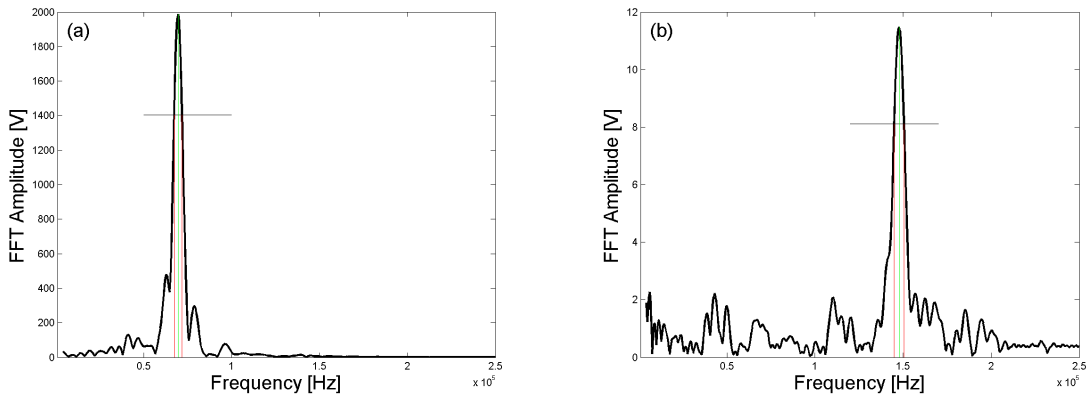

Figure 21. The half-power bandwidth method implemented on MEMS AE sensors (a) the S1 sensor result for ball impact test, (b) the S2 sensor result for PLB test

capacitance, resistance, mass and gap. Therefore, the potential error in quantifying the Q factor is higher than the direct measurement using the half-power bandwidth. The discrepancy between the analytical and experimental results of the Q factor indicates the inaccuracy of the simplification needed for the analytical method (e.g. no-slip condition).

In addition to the amplitudes and the waveforms of the MEMS and piezoelectric sensors, the signal to noise ratios (SNR) are compared. Equation 3.14 and Equation 3.15 define the SNR and SNR_{db}, respectively.

$$SNR = \frac{P_{Signal}}{P_{Noise}} = (\frac{A_{Signal}}{A_{Noise}})^2 \tag{3.14}$$

$$SNR_{db} = 20 \log \frac{A_{Signal}}{A_{Noise}} \tag{3.15}$$

TABLE IX

THE COMPARISON OF THE Q FACTOR RESULTS

sensor	Analytical	Admittance test	Half-power bandwidth method
S1	114	6	16
S2	264	7	27

P is the power and A is the amplitude of the sensor output. In these equations, the amplitude can be calculated solely based on the properties of the sensing element to predict the nominal SNR. In the nominal SNR, A_{signal} is the maximum signal amplitude, which the sensing element produces. A_{noise} is based on the calculation of thermal noise and Flicker noise of the sensing element [43]. Since the nominal SNR doesn't consider anything beyond the sensor such as cables, connections and packaging effect, the method overestimates the SNR values. Therefore, in this study the experimentally identified amplitude values are used to calculate the SNR. Based on Equation 3.14 and Equation 3.15, Table X is formed to compare the SNR values of the MEMS and the piezoelectric sensors excited under the same source. In this table, the complete waveform signatures of the sensors are used in the 'overall response' calculation to read the amplitudes at the pre-trigger region (A_{noise}) and the sensor response to the source (A_{signal}). The amplitudes at the resonance frequencies of the sensors in the frequency domain are used to quantify the SNR values for 'only for the ω_n' column.

Considering the responses only for the ω_n, the S1 sensor has slightly higher SNR_{db} value than the R6 sensor, and the S2 sensor has slightly lower SNR_{db} value than the R15 sensor at

TABLE X

SNR MEASUREMENTS FOR THE MEMS AND PIEZOELECTRIC SENSORS

sensors	Overall response		Only for the ω_n	
	SNR	SNR_{db}	SNR	SNR_{db}
MEMS-S1	2916	34.65	752221	58.76
Piezoelectric-R6	19321	42.86	292287	54.66
MEMS-S2	2.25	3.52	9595	39.82
Piezoelectric-R15	324	25.10	23802	43.77

their resonant frequencies. If the footprint areas of the sensor types are taken into consideration, the MEMS sensors have superior performance. The piezoelectric sensors have a circular footprint of 19 mm diameter (about 283.5 mm^2), while the MEMS sensors have the rectangular footprint of 2.5 mm $\times$ 5 mm (about 12.5 mm^2). The MEMS sensors are about 22 times smaller than the piezoelectric sensors without considering the MEMS packaging. In the current design, the MEMS device includes several other designs for the research purpose; therefore, the device size is 10 mm $\times$ 10 mm while the sub-dicing could reduce the device size to the same as the individual sensor unit.

3.6 Summary

The MEMS AE sensors presented in this chapter have improved signal to noise characteristics as compared to the current designs using surface micromachining method. The sensor sensitivities are comparable to piezoelectric sensors. MetalMUMPs allow designing thick metal layer and dielectric layer between the electrodes to prevent the failure mode of stiction. The

sensors are sensitive to unique wave direction, which can be utilized to increase the accuracy of source localization through selecting the correct wave velocity on structures having guided waves. The time domain signatures indicate a well-defined resonant behavior as opposed to the piezoelectric sensors. The MEMS sensors are functional at atmospheric pressure and are more sensitive at their design frequencies in comparison with the similar frequency piezoelectric sensors. Considering the relative sizes of two sensor types, this is a significant achievement. Further improvements in the sensor performance can be achieved through proper packaging design and a low noise pre-amplifier circuit.

CHAPTER 4

MEMS IN-PLANE AE SENSORS

The content of this chapter is partially published as "In-Plane MEMS Acoustic Emission Sensors Development and Experimental Characterization" in the "Proceedings of the 2013 Annual Conference on Experimental and Applied Mechanics" with my advisor, Dr. Ozevin, as the co-author [2] .

4.1 Introduction

This chapter presents the design, layout, numerical and experimental characterization of in-plane (IP) MEMS AE sensors. The numerical models include resonant frequency calculations at the intended in-plane direction and the unintended out-of-plane direction, and capacitance computation. The experimental characterization includes capacitance and impedance measurement, and mechanical characterization to understand the directional dependence of the sensor output under dynamic excitation.

4.2 Design Parameters and Final Layout

The IP MEMS AE sensors are made of comb drives, which are formed by stationary and moving fingers in the planar direction. The comb drive sensors are designed with two principles as area change and gap change in order to compare the response characteristics as signal to noise ratio and the separation of the intended in-plane motion and the unintended out-of-plane motion. Similar to the OOP MEMS AE sensors, the design parameters include maximum

capacitance value and resonant frequencies in the range of 100-200 kHz. The total capacitance is controlled by number of fingers and their overlap areas; the spring and mass dimensions are varied to tune the sensors to particular frequencies. Two IP MEMS AE sensor are designed on the same device: 1) near 150 kHz and called S3 sensor, which uses change in the gap between the electrodes as its principal of transduction, 2) near 100 kHz and called S4 sensor, which uses change in the facing area of electrodes as its principal of transduction. Figure 22 indicates the electrodes connected to each capacitive microstructurs and particular connection pads. There is a redundant moving electrode pad for the case of malfunctioning wirebonding for the S3 sensor.

Multiple unit cells are connected in parallel to increase the total capacitances of the sensors. Each sensor is formed by 65 unit cells and 49 unit cells for S3 and S4 respectively, which are identified by two constraints: one dimension as 5 mm in order to place other sensors on the device area of 10 mm x 10 mm and total capacitance targeted as higher than 20 pFarad. The sensor sensitivity is directly proportional to the total capacitance. It is assumed that the mechanical properties of the combined geometry are the same as the single unit cell.

The S3 and S4 sensors are designed to be sensitive to –y (ΔG_y) and –x (ΔA_x) directions, respectively as shown in Figure 22. The identical sensors are rotated by 90° and placed next to them in order to differentiate orthogonal wave motions. The sensors are referred as S5 and S6 sensors, which are sensitive to –x (ΔG_x) and –y (ΔA_y) directions, respectively. Figure 23 shows the locations of four IP MEMS AE sensors on the overall device area.

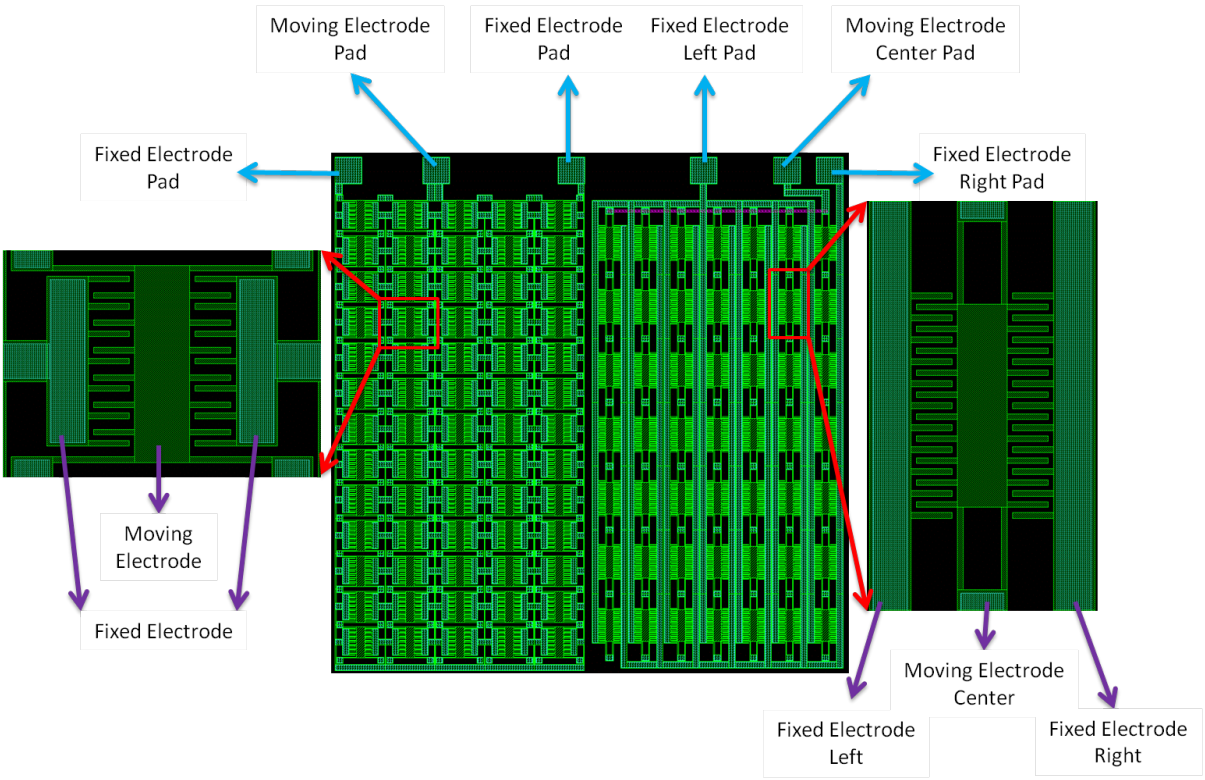

Figure 22. CADENCE plots indicating the unit cells, combined sensors and connection pads for the MEMS IP AE sensors

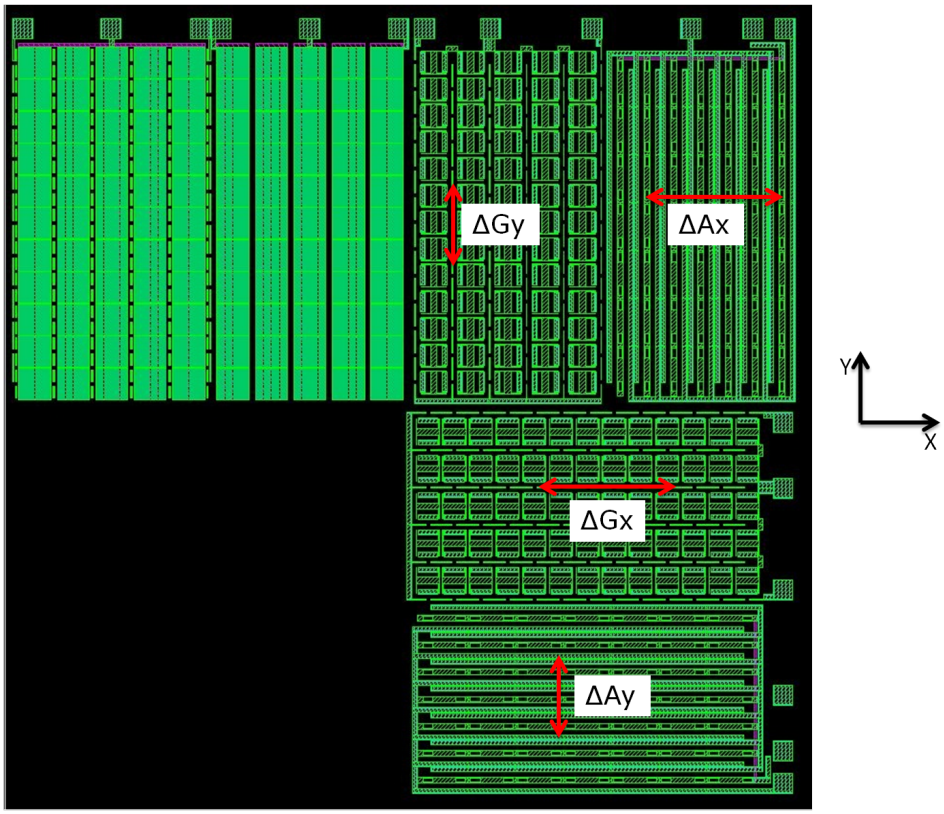

Figure 23. CADENCE plots indicating the sensitivity directions of four IP MEMS AE sensors

TABLE XI

THE DIMENTIONS OF AREA CHANGE AND GAP CHANGE IP MEMS AE SENSORS

Sensor type	Mass		Spring		Gap				Fingers	
	Width	Length	Width	Length	1	2	3	4	Thickness	Length
Area change	80	288	8	120	8	8	8	8	8	60
Gap change	72	296	8	120	8	16	8	8	8	60

all units are μm

Figure 24 describes the geometric variables of unit cells of two designs. For the area change design, Figure 24(a), the spring elements forming the stiffness of the dynamic system move in -x direction that causes the overlap area of stationary fingers and moving fingers change. The spring length and the mass width are varied to reach the target frequency in the range of 100-200 kHz. The vibration frequency of the fingers is designed as greater than 1 MHz; therefore, they stay stationary under the dynamic excitation, which does not include frequencies higher than 1 MHz. The dimensions of the unit cell gap 1 to gap 4, mass and spring elements are provided in Table XI. The area change design is configured such a way that the sensor can operate as differential mode in order to remove the effect of unintended out-of-plane motion. For the gap change design, Figure 24(b), the spring elements move in -y direction, which causes the changes of gap 1 and gap 2 shown in the figure. When the fingers move in -y direction, gap 1 decreases while gap 2 increases.

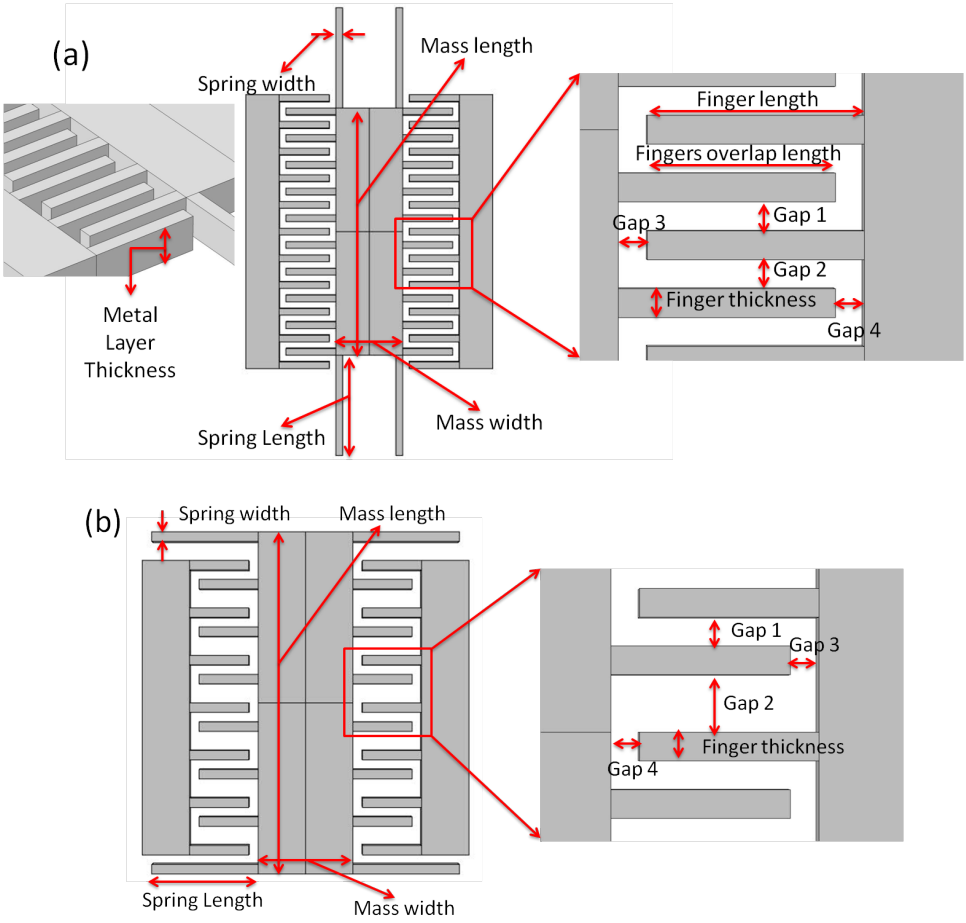

Figure 24. The descriptions of unit cells, (a) the S4 sensor, (b) the S3 sensor

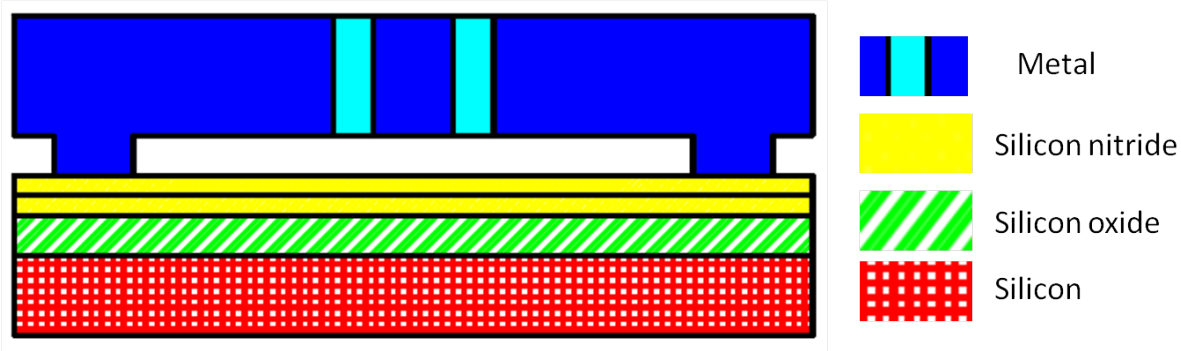

Figure 25. The cross section of the IP MEMS AE sensors

4.3 Manufacturing Steps

The manufacturing layers and processes to design the MEMS in-plane AE sensors discussed in this chapter are the same as the process steps described in section 3.3 except that the polysilicon layer is only used in electrical connection and not as a part of the sensing structure. Figure 25 illustrates the cross sectional view of the IP MEMS AE sensors.

Figure 26 shows the SEM images of the sensors. Comparing the design and the final geometry indicates that the intended geometry is successfully manufactured.

4.4 Numerical Modeling of IP MEMS AE sensors

4.4.1 Resonant Frequency

Each unit cell is numerically modeled using Comsol Multiphysics software (COMSOL 4.2a) in order to determine the resonant frequencies and the static capacitance. For the frequency identification, the model is simulated using the eigenfrequency study using the design geometries

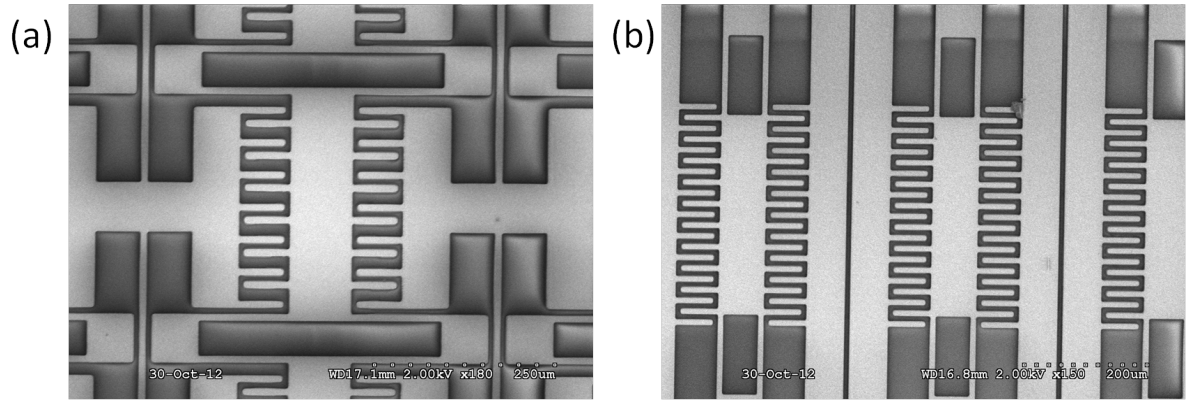

Figure 26. SEM images of (a) the S3 sensor, (b) the S4 sensor

and material properties. The first (in-plane direction) and second (out-of-plane) modes are shown in Figure 27 and Figure 28, respectively. The mode shapes and eigenfrequencies are indicated on the images. The lateral resonance is proportional to $\sqrt{hb^3}$ while the transverse resonance is proportional to $\sqrt{bh^3}$. Therefore, the analytical ratio of the frequencies of out-of-plane direction to in-plane direction is about 2.5; however the numerical and experimental results discussed in the following sections doesn't agree with this theoretical ratio. The first natural frequencies (in-plane direction) are calculated as 144 kHz and 101 kHz for the S3 and S4 sensors, respectivly. The second natural frequencies (the out-of-plane direction) are calculated as 267 kHz and 165 kHz for the S3 and S4 sensors, respectively.

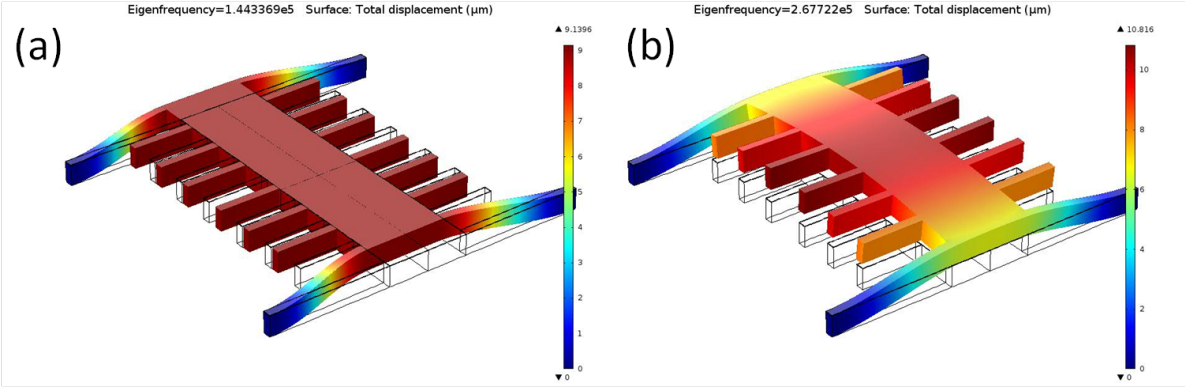

Figure 27. The first and second mode shapes of the moving electrode of the S3 sensor: (a) in-plane mode at 144 kHz (b) out-of-plane mode at 267 kHz

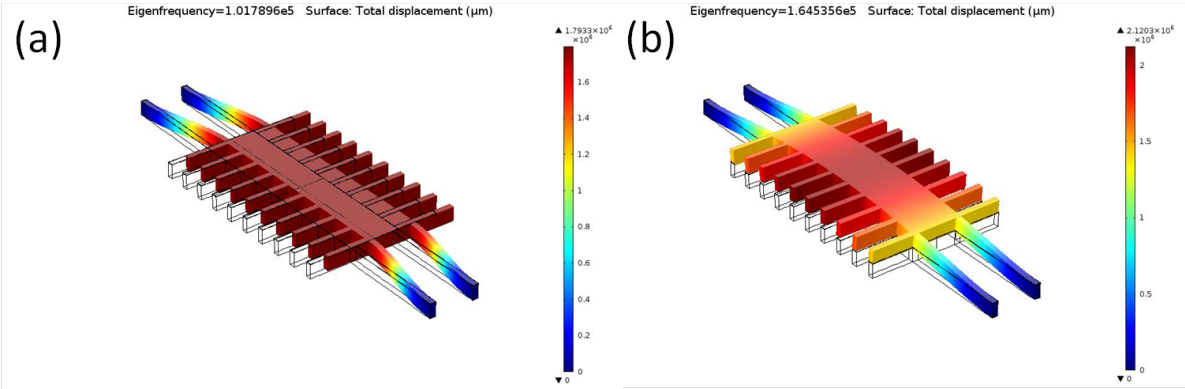

Figure 28. The first and second mode shapes of the moving electrode of the S4 sensor (a) in-plane mode at 101 kHz (b) out-of-plane mode at 165 kHz

4.4.2 Capacitance

The static capacitance including the fringe fields is obtained using COMSOL software. A box of air is formed around the geometry to create the electrical field and solve for the capacitance. 1 V_{DC} is applied to the stationary comb, which forms the terminal; the moving layer is defined as the ground terminal to measure the capacitance. The 3D model includes the fringe fields as well as the parallel plate capacitance, shown in Figure 29. The capacitance of individual sensors are calculated as 3 pF for gap change and 2 pF for each side of the area change comb drive. As stated before, 65 unit cells for S3 and 49 unit cells for S4 are parallelly connected to from the final design. Therefore the calculated final capacitance for the S3 and S4 are 195 pF and 98 pF, respectively. However the experimental values measured and presented in the next section are approximatly 23 pF and 17 pF, respectively. Understanding the accurate behavior of IP MEMS AE sensors is future work.

4.5 Experimental Characterization

4.5.1 Electromechanical Characterization

The electromechanical characterization tests include capacitance measurement and impedance measurement using HP 4294A Impedance Analyzer. The capacitance curve is obtained through sweeping a range of DC voltages with 500 mV alternative voltage at 1 MHz. Figure 30 shows the C-V plots for area change and gap change sensors. While the capacitance sensors have parabolic relationship between capacitance and DC bias voltage, unexpected response is observed. There are two potential explanations for the C-V responses. The alternative voltage frequency is close to vibration frequency of the fingers, which may cause unexpected resonance of fingers. While

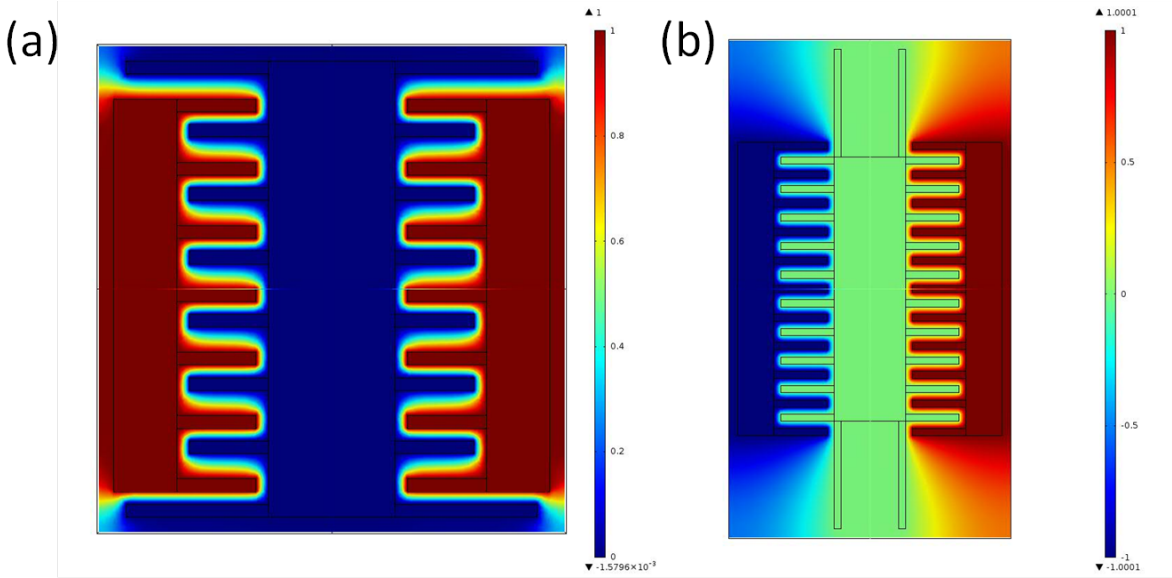

Figure 29. Numerical simulations indicating the capacitance and fringe fields for(a) the S3 sensor, (b) the S4 sensor

the frequency is varied to be away from the resonance frequency of the fingers, the error in the capacitance measurement due to the limitation of the impedance analyzer becomes higher. The other reason may be because of parasitic displacement in the unintended direction at the out-of-plane direction [52]. The C-V behaviors of the sensors require further research.

The magnitude and phase plots of the admittance values for a range of frequencies are shown in Figure 31. While the resonance is not clear in the magnitude plot, it is clearly seen in the phase plot. The resonance frequencies of the S3 and S4 sensors are measured as 190 kHz and 150 kHz, respectively. The admittance measurement can't differentiate between the out-

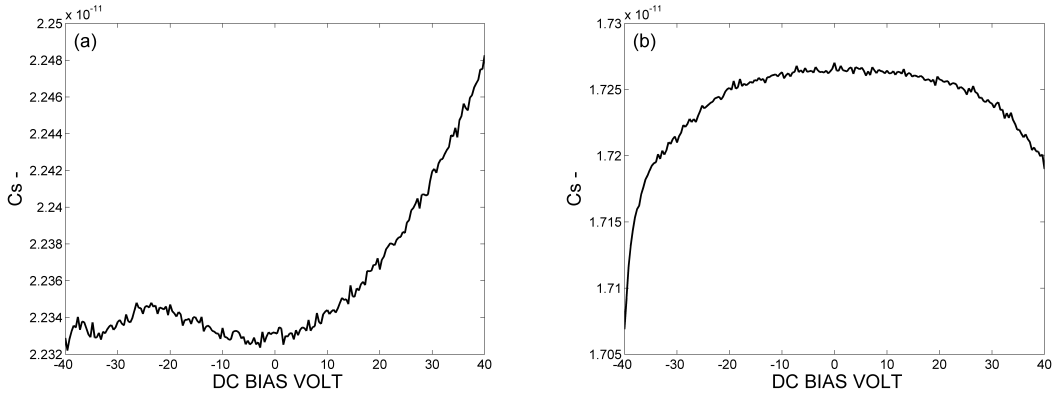

Figure 30. C-V curves of (a) the S3 sensor, (b) the S4 sensor

of-plane and in-plane resonant frequencies, potentially due to high damping. The gap between the fingers is 8 μm and between the moving mass and the silicon nitride bellow it is 1.1 μm; therefore, the squeeze film damping in the out-of-plane mode is significant compared to its values in the in-plane mode, since the sensor operates in atmospheric pressure. The numerical results of the resonant frequencies at in-plane direction for the S3 and S4 sensors are 144 kHz and 101 kHz, respectively. Further tests are needed to characterize the IP MEMS AE sensors.

4.5.2 Mechanical Characterization

The isolation of the intended in-plane motion and the unintended out-of-plane motion is the critical design criterion of the sensor. Figure 15 shows the photograph of the experimental setup, which includes Nd:Yag Q-switched laser source, optical breadboard, mounting block and oscilloscope. The sensors are connected to 45 DC bias source using 9 V batteries. The

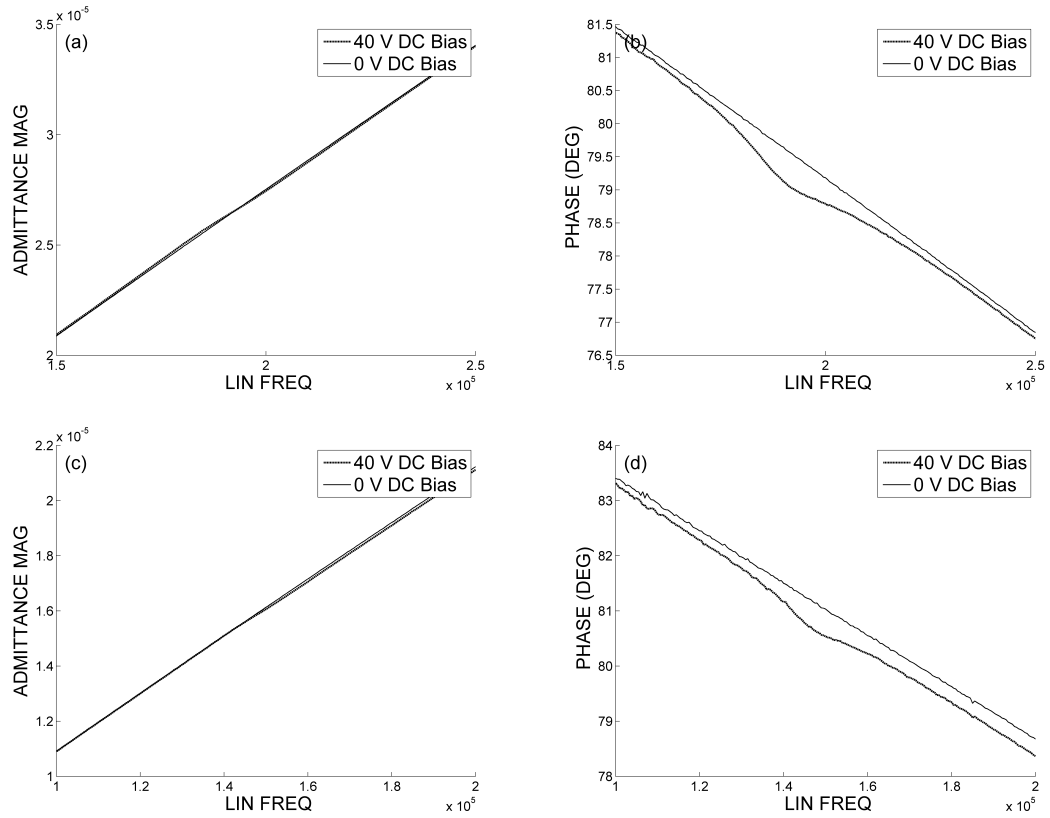

Figure 31. Admittance plots of sensors with the principle of (a,b) the S3 sensor, (c,d) the S4 sensor

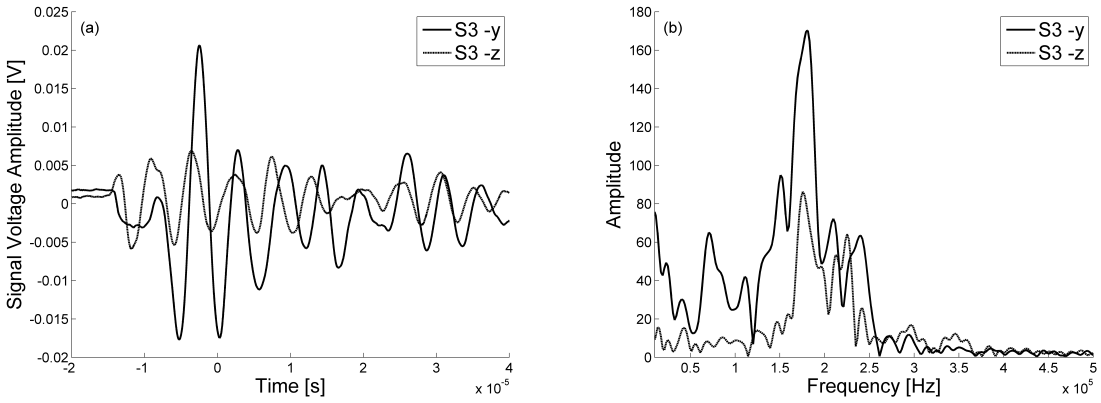

Figure 32. Waveform histories and frequency spectra of the gap change sensor, S3, for (a) out-of-plane (-z) and (b) in-plane (-x) directions.

orientation of the mounting block is changed in order to load the sensor in out-of-plane direction (-z) and in-plane direction (-x). The in-plane loading direction is -y direction for the gap change design. The laser source creates a step load defined with Heaviside step function with 3 nsec rise time in orthogonal direction to the loading direction.

Figure 33 shows the waveforms and frequency spectra of the area change sensor, S4, when the sources are varied in -z and -x (intended) directions. The response in -x direction has a sudden drop and then the sensor resonates. The initial displacement profile is similar to the theoretical response at the epicenter due to the laser source [49]. The initial displacement causes zero frequency, which is not observed for the -z direction (unintended) excitation. The frequency bandwidth of 160-300 kHz is observed for both excitation directions. This proves the high damping coefficient, which causes a wide bandwidth response. However, the intended

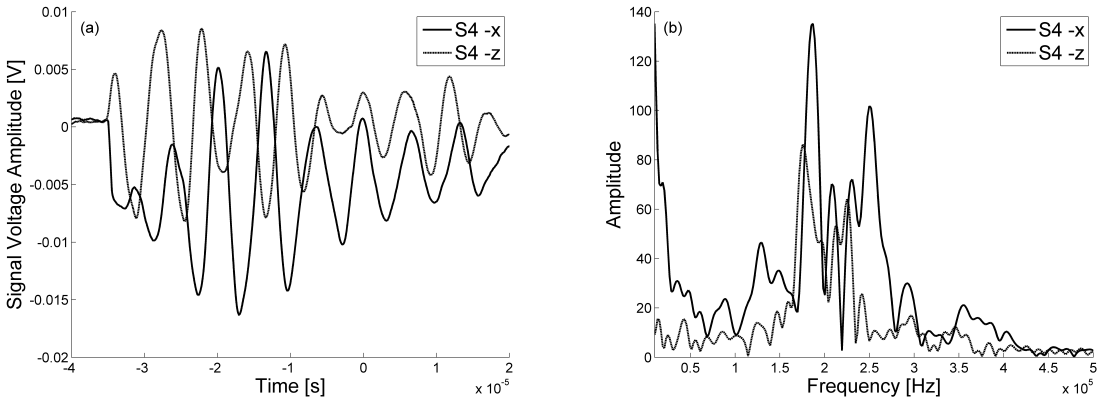

Figure 33. Waveform histories and frequency spectra of the area change sensor, S4, for (a) out-of-plane (-z) and (b) in-plane (-x) directions

direction excitation has a clear peak around 135 kHz, while the second peak is around 190 kHz. This observation agrees with the numerical simulation, where, without considering the damping, the in-plane frequency was 101 kHz and out-of-plane frequency was 165 kHz. The absence of the peak freaquency at 135 kHz when the excitation is at the out-of-plane direction is interpreted as that this frequency is the in-plane resonant frequency.

Figure 32 shows the waveform histories and frequency spectra of the gap change sensor, S3. The amplitude at the signal drop at the beginning of the waveform is smaller than that of the area change sensor; however, the overall maximum values are similar. There are several frequencies observed in the -y direction excitation as compared to the -z direction excitation such as 80 kHz, 150 kHz. The amplitude in the -y direction is also higher than the amplitude in the -z direction. While there are clear differences between the sensor response under the excitation

sources at the intended (-y) direction and the unintended (-z) direction, the frequency spectra doesn't show a clear pattern for separating the intended direction from the unintended ones as the numerical simulations predicts.

The responses of the in-plane sensors to the excitation sources in two orthogonal directions result in complex behavior. When the source is generated in –x direction, there is a sudden drop in the response, which is similar to the source time function of the laser induced source as Heaviside step function [49]. This may be because of higher damping coefficient and more broadband response. After the sudden drop, resonant type behavior is observed. When the excitation source is generated in –z direction, no such drop is observed. The sensor directly behaves as a resonant sensor. There are differences in the frequency domain responses, which can be utilized to decouple the response histories of the in-plane sensor due to motions in –x and –z directions. The frequency bandwidth of the IP MEMS AE sensors are higher than the frequency bandwidth of the OOP MEMS AE sensors. This may be due to different damping phenomenon at each direction.

4.5.3 S4 sensor: Individual Mode versus Differential Mode

The electrical and mechanical characterization tests show that the output signal is the result of in-plane and out-of-plane motions. The area change sensor, S4, is designed such as a way that the sensor can be connected in a differential mode in order to cancel the motion at the out-of-plane direction. The S4 sensor can operate as an individual mode using one side of the sensor or differential mode through applying opposite electric fields at each of the stationary electrodes, and connecting the moving electrode to the output terminal. For the differential

mode, a slight difference in capacitance may prevent such cancellation; therefore, each capacitor is connected to different level of input voltage to balance the overall energy levels.

4.5.3.1 Individual Mode Operation

Each side of the comb drive sensor is connected to the oscilloscope in order to compare the behavior to the in-plane and out-of-plane simulations. Figure 34 shows the electrical connections of the individual mode operation. The moving electrode is connected to the voltage source; the stationary electrodes are connected to the input channel of the oscilloscope. Ball drop impact simulations are conducted on the bottom of the package (out-of-plane wave generation) where a 3.2 mm steel ball is droped from the height of 231 mm.

Figure 35 shows the signals from both of the fixed electrodes or $V_{sensor1}$ and $V_{sensor2}$. Both sides of the S4 sensor have the same waveform shape while the amplitudes are slightly different. $V_{sensor1}$ has the amplitude of 0.1992 V while $V_{sensor2}$ has the amplitude of 0.1202 V. When each side is separately connected for the capacitance measurement, the capacitance values for sensor 1 and sensor 2 are measured as 17.5 pF and 16.3 pF, respectively. As C_L (or $C_{sensor1}$) has higher capacitance than C_R (or $C_{sensor2}$), its amplitude to the ball drop excitation is higher. The difference in the amplitudes of each side requires applying different voltages for the differential mode operation. Therefore by a simple post-processing step the unintended signal may be eliminated from the output.

4.5.3.2 Differential Mode Operation

Figure 36 shows the electrical connection of the differential mode operation. The stationary electrodes of the left side of the sensor are connected together to $+V_{DC}$. The stationary

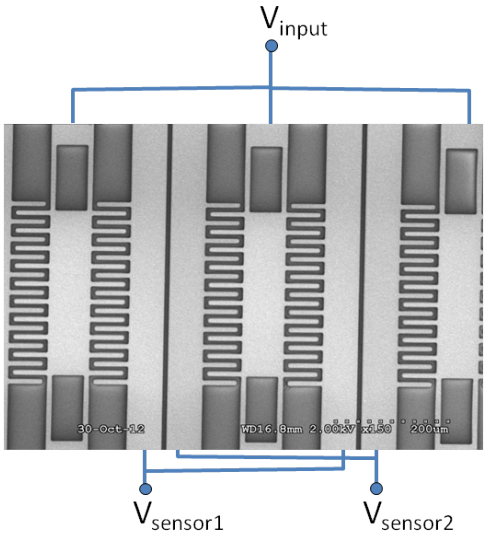

Figure 34. Electrical connection of individual mode operation shown on SEM image

electrodes of the right side of the sensor are connected to $-V_{DC}$. All the moving electrodes of individual cells are connected together to record the output signal. As the capacitance of each side is different, different voltage levels are applied, and the approach is referred as the balanced differential mode. The balanced differential mode is achieved by balancing the electrical field between two sides of the sensor using the following equations:

$$\frac{E_2}{E_1} = \frac{V_2}{V_1} \times \frac{C_2}{C_1} \tag{4.1}$$

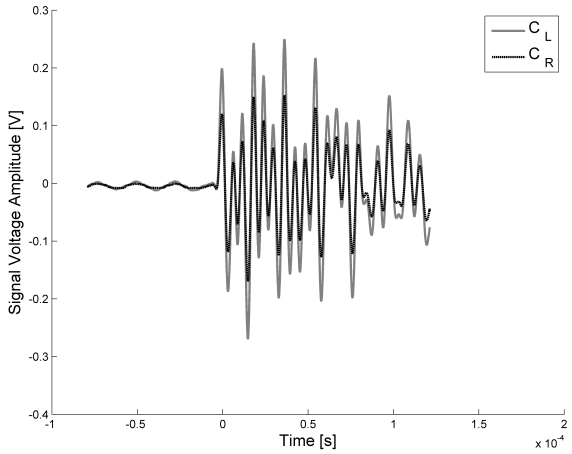

Figure 35. Electrical signal of individual mode operation

When $E_2 = E_1$, the equation becomes:

$$\frac{V_1}{V_2} = \frac{C_2}{C_1} \tag{4.2}$$

The capacitances of the left side and the right side are measured as 17.5 pF and 16.3 pF, respectively. The required voltage levels for the balanced differential mode are 42.2 V and 46 V. The ball drop experiments are repeated when the S4 sensor is operated in the differential mode. Figure 37 shows the output signal in time domain. Although the signal at the unintended out-of-plane direction could be not completely removed, the signal amplitude is reduced by 90% as compared to the individual mode operation.

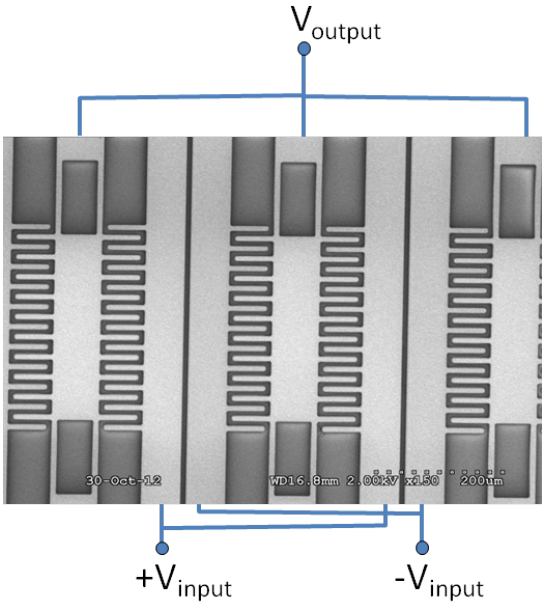

Figure 36. Electrical connection of differential mode operation shown on SEM image

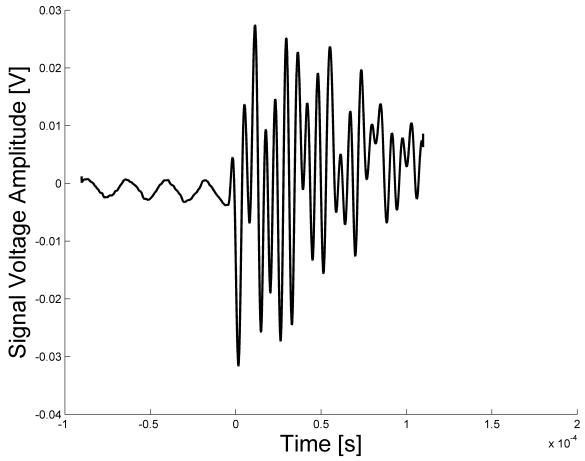

Figure 37. Electrical signal of differential mode operation

4.6 Summary

In this chapter, the IP MEMS AE sensors are introduced. The experimental characterization of the IP MEMS AE sensors shows that they exhibit complex response under static and dynamic loading due to the coupled behavior of the in-plane and the out-of-plane motions. While numerical simulations show two distinct frequencies at each direction, the experimental results show wideband frequency response. The balanced differential mode operation of the area change sensor (S4) reduces the amplitude of the unintended out-of-plane amplitude by 90%. Further research is needed to completely characterize the IP MEMS AE sensors, including the analytical equations of coupled in-plane and out-of-plane motions with damping models for capacitance, impedance and electrical signal measurement.

CHAPTER 5

MEMS STRAIN SENSORS

The content of this chapter is previously published as "MetalMUMPs-Based Piezoresistive Strain Sensors for Integrated on-chip Sensor Fusion" in the journal of IEEE sensors with my advisor, Dr. Ozevin, as the co-author [3].

5.1 Introduction

The organization of this chapter is as follows. The design parameters, manufacturing steps, and final design of the MEMS strain sensors are first presented. Then the numerical simulation results of the strain sensor including all the layers are discussed. The characterization experiments including monotonic, cyclic and fatigue mechanical loading, and thermal loading are presented.

5.2 Design Parameters, Microfabrication and Layout

As discussed in section 2.4 the resistance and the gauge factor are two important design parameters for resistive type strain sensors. The target strain-free resistance of the MEMS sensors designed in this study is 350 Ω in order to use conventional Wheatstone bridge data acquisition systems designed for metal gauges. Using the resistivity coefficient of polysilicon reported by the manufacturer as 22 Ω/sq, length and width of each microstructure were varied to reach the target resistance. The thickness of this layer is also fixed by MetalMUMPs as 0.7 μm. Therefore the length and the width are the adjustable variables. In this study, the

width of polysilicon layer is set as the minimum feature size of 5 μm leading the length of the resistance as 79.5 μm.

The manufacturing process steps, which are used for MEMS strain sensors, are schematically explained in Figure 38: (1) the process starts with a single crystal silicon wafer as the substrate. (2) A layer of silicon oxide is grown on the substrate and then another layer is deposited to from the total thickness of 2.5 μm. (3) Next a 0.35 μm thick silicon nitride layer is deposited. (4) A 0.7 μm thick layer of polysilicon, which forms the piezoresistive sensing element, is deposited and patterned, (5) followed by another 0.35 μm thick layer of silicon nitride. The silicon nitride is then etched in areas to create the etch holes for trenching the substrate and open a window on the polysilicon layer for the connection pads. (6) Then another 1.1 μm thick layer of silicon oxide is deposited to function as sacrificial layer for the suspended metal layer. (7) A thick layer of metal (20 μm of Nickel and 0.5 μm of Gold) is deposited. The metal layer is utilized as the wire pads for strain sensors. Finally, (8) the sacrificial layer is etched to release the metal layer (for AE and accelerometer designs), and the silicon substrate is etched about 25 μm deep to form the trench under strain sensors. Each device with the area of 1 cm x 1 cm is mounted on an aluminum oxide package using silver epoxy. Then they are electrically connected to the package through wire-bonding.

The final device layout is displayed in Figure 39. The figure illustrates three 350 Ω strain sensors at the bottom-left corner. The sensors are oriented in -x, -y, and -xy (i.e., 45 degrees) directions for the purpose of extracting principle strains. The Scanning Electron Microscope (SEM) images of the strain sensors are demonstrated in Figure 40. The dark surfaces at two

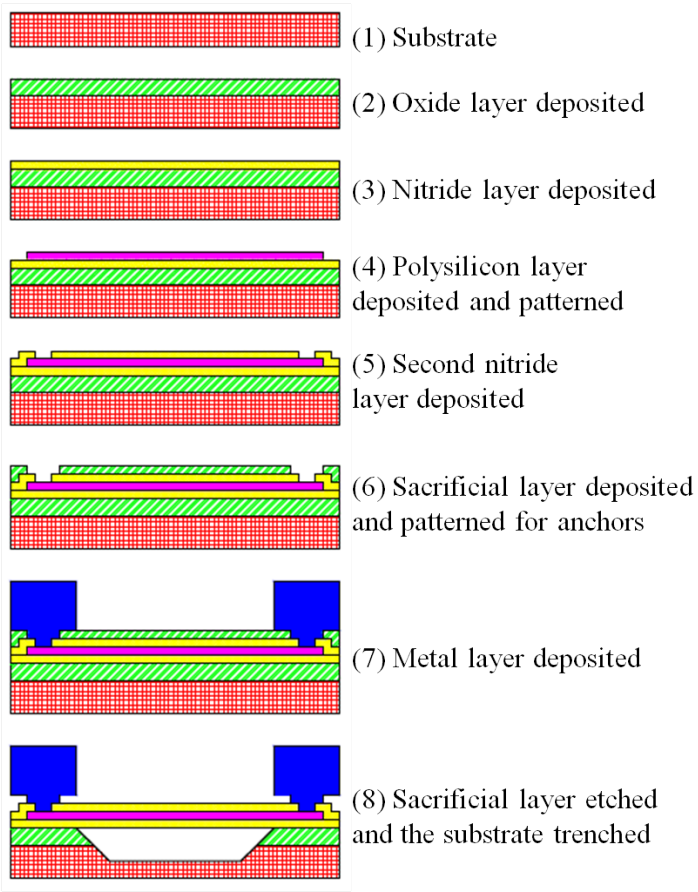

Figure 38. Schematics of MEMS manufacturing steps of MetalMUMP with their descriptions used for the MEMS strain sensors

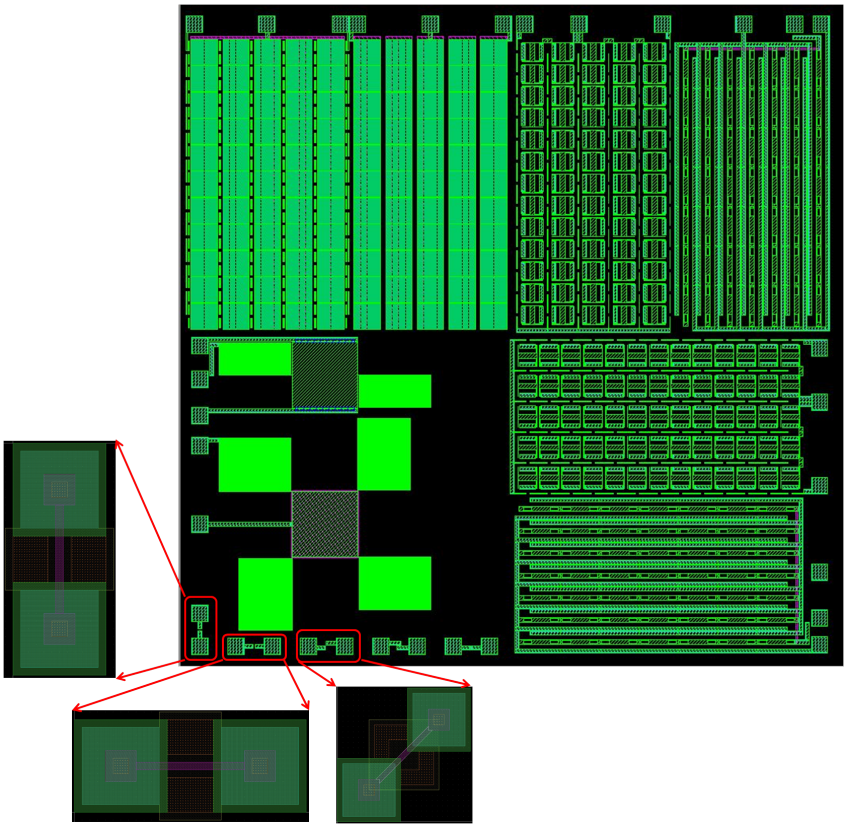

Figure 39. Final device layout illustrating the position of strain sensors along with other sensors

sides of the strain elements are the result of etched silicon substrate. This reduces the influence of stiff substrate for the strain transfer. Each strain sensor has anchors at both ends, and the strain change causes elongation or contraction depending on the direction of loading. In order to design for a specific resistance value (i.e. 350 Ω) the geometry sizes and resistance coefficient of the material are independent variables.

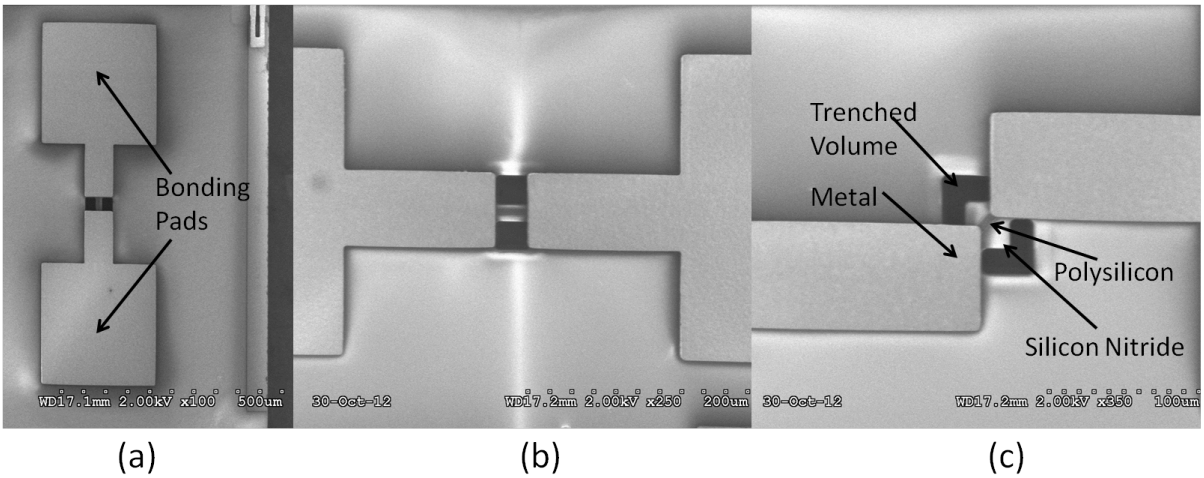

Figure 40. SEM images of the MEMS strain sensors for (a) –y, (b) –x, and (c) -xy directions

5.3 Numerical Characterization

5.3.1 Effect of Trenching

The first numerical model is a 2D model, which considers the effect of trenching on the strain value inside the sensing element. The 2D model includes a simple rectangular aluminum specimen fixed at one side, and the tensile load is applied from the other side. Silicon substrate and polysilicon layer are idealized as perfectly attached to the aluminum specimen. Figure 41(a) shows the configuration that silicon substrate is not trenched. The figure indicates complete view of numerical model as well as close-up views to highlight the edge effect of silicon substrate, and strain distribution along the polysilicon layer. Figure 41(b) shows the configuration that silicon substrate beneath the polysilicon layer is trenched.

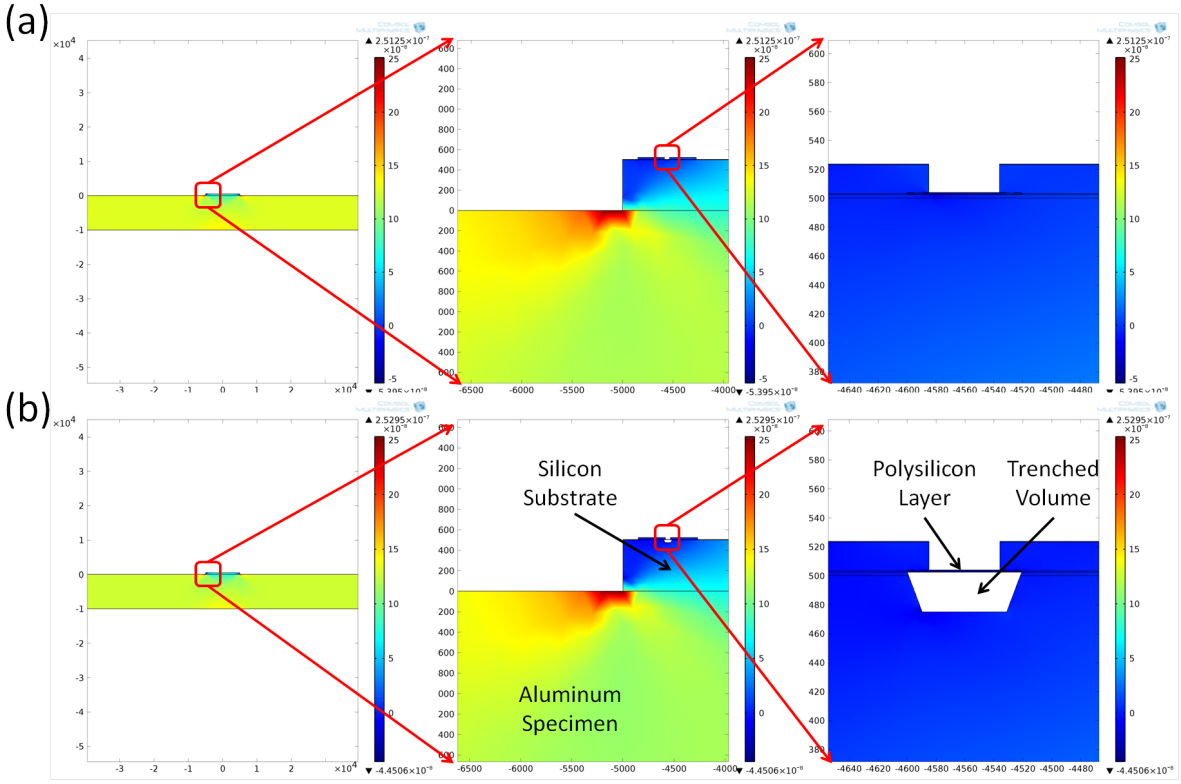

Figure 41. 2D numerical simulation of (a) un-trenched, and (b) trenched silicon substrate beneath the polysilicon layer

TABLE XII

STRAIN COMPARISON OF DIFFERENT LAYERS

Measurement Location	Strain ($\mu\epsilon$)
Aluminum specimen without sensor	127.3×10^{-3}
Polysilicon layer without trenching	-8.2×10^{-3}
Polysilicon layer with trenching	-13.5×10^{-3}

The average strain in the applied load direction (i.e. -x direction) is calculated under three conditions: strain on aluminum specimen without sensor, strain on polysilicon without silicon trenching, strain on polysilicon with silicon trenching. Table XII shows the strain values of three conditions. The comparison shows that the trenched condition increases the strain transfer to sensing element by 61% as compared to the un-trenched condition. In other words, approximately 39% of the strain loss due to substrate rigidity is recovered by trenching. The presence of trenching has clear positive influence to the strain transfer to sensing element. However, the strain reading on polysilicon layer is still about ten times less than the strain reading on aluminum specimen. In addition to the reduction of stress transferred from the aluminum specimen to polysilicon layer, stress observed on the polysilicon layer has opposite direction as compared to stress on the aluminum surface. While the aluminum specimen is loaded in tension, the numerical model results in compressive stress on the polysilicon layer. The polysilicon layer is located at the free boundary of the ceramic package. The opposite surface of the ceramic package is bounded to the aluminum specimen. The finite dimension of the ceramic package with bounded and free boundaries is considered as the reason of stress direction change on the polysilicon layer. This phenomenon is explained by the shear lag theory [38], [53]. Hautamaki et al. [53] performed a bonded silicon film model to a metallic structure, and resulted in a similar result as changing stress direction on the silicon layer as compared to the metal.

5.3.2 Effect of Sensor Location on the Device

Table XII reveals that the strain values at the sensing element placed at the edge of the substrate undergoes negative strain (compression) whereas the specimen experiences the positive strain (tensile). To better study this phenomenon the 3D model is built to simulate the experimental condition, which will be explained in more detail in the next section.

An aluminum specimen with a symmetrical winged rectangular cube and thickness of 1 cm, width of 2 cm, and length of 17 cm (Figure 42) is built to place the MEMS device on the winged section. The side wings are 1 cm^3 cubes located at the center of the length on the opposite sides. The boundary conditions of the top and the bottom areas are set as fixed and free, respectively. The layers of the MEMS ceramic package (thickness as 1 mm) and silicon substrate (thickness as 500 μm) are modeled on the left wing whereas the other side has free surface. Three different load steps (4 kN, 8 kN and 12 kN) are applied to the specimen at –z direction, and the strain values are measured on the silicon substrate surface as well as on the free surface of the right wing. Figure 43 shows the locations for which the strain data are calculated. The strain values in two in-plane directions (in this case –y and –z direction) along edge line (EL), center line (CL) as well as edge point (EP) and center point (CP) are compared in Figure 44 through Figure 46.

Figure 44 (a) and (b) show strains along the vertical lines of edge and center for the right wing on free surface, and the left wing on the silicon substrate, respectively. Strain values at two edges are significantly lower than those at the center. Additionally, the presence of ceramic package and silicon substrate layers cause different strain direction at the edges as compared

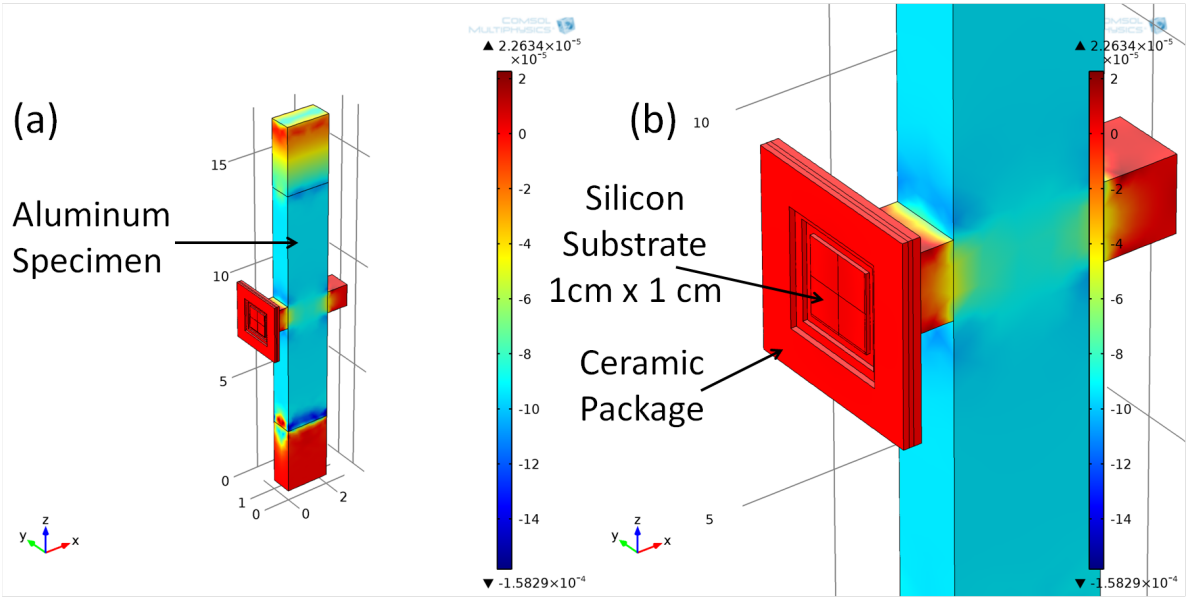

Figure 42. The 3D model used to study the effect of sensor location on the substrate (a) specimen under 4kN tension load, (b) close view of MEMS package attached to the aluminum specimen

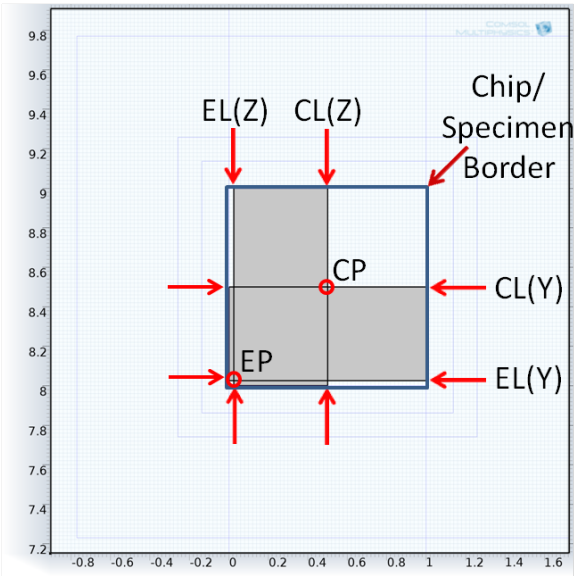

Figure 43. Surface of silicon substrate indicating the measurement lines of strain (EL: edge line, CL: center line, EP: edge point, and CP: center point)

to the centerline (shown in Figure 44(b)). Figure 45 shows the strains along –y direction. The comparison of two figures at the centerline indicates the difference in strain values at two orthogonal directions; however, the comparison becomes more complex at the edges. The transferred strain to the silicon substrate does not follow the same pattern of the free surface because of the rigidity of the ceramic package and silicon substrate, which is referred as the substrate effect. In order to show the differences of the free surface and the silicon surface, strains of edge and centerlines for two sides are plotted together in Figure 46 for a particular load level of 12 kN. The figure indicates the strain transfer effect to the silicon substrate. For instance, the strain at the center point of the edge line is about 50 $\mu\epsilon$ whereas the value is

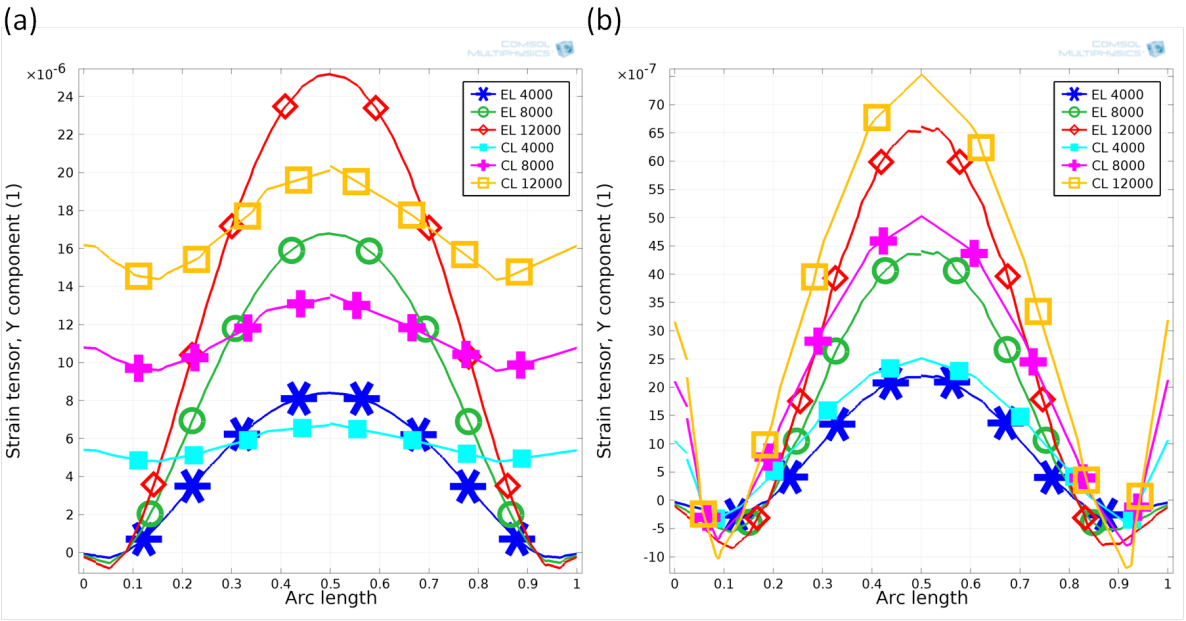

Figure 44. Vertical (-z direction) strain values along the length of silicon substrate due to three different loads at –z direction (a) the right wing on free surface, and (b) the left wing on silicon substrate

reduced to about 12 $\mu\epsilon$ on the silicon substrate. The free surface observes negative and positive strains along the edges at the vertical and horizontal directions, and the silicon substrate is under opposite strains due to the edge effect.

The numerical models indicate that the location of the strain sensor on the silicon substrate is critical for proper strain transfer. In this study, the strain sensors are placed to the edge of the substrate as the other sensors (acoustic emission and accelerometer) occupied the majority of

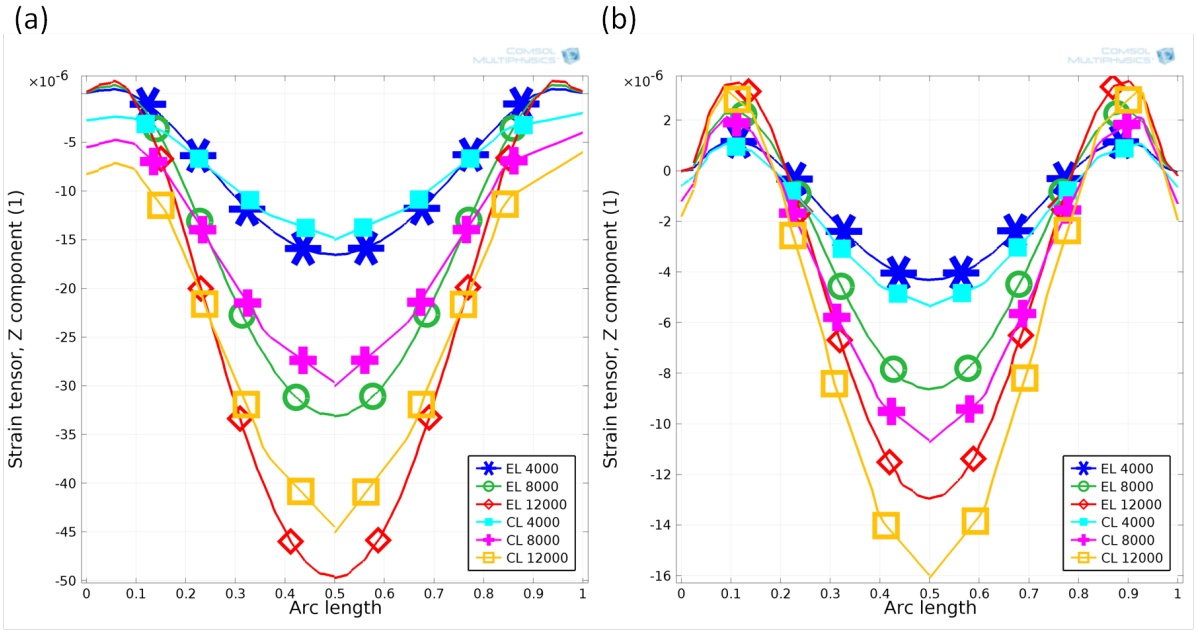

Figure 45. Horizontal (-y direction) strain values along the length of silicon substrate due to three different loads at –z direction (a) the right wing on free surface, and (b) the left wing on silicon substrate

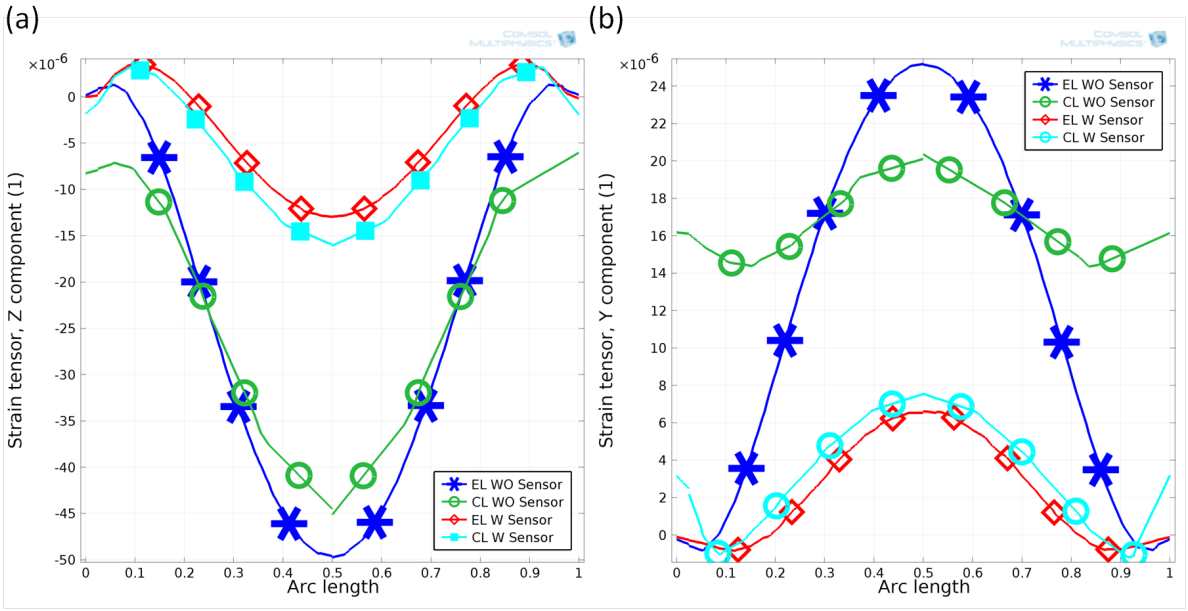

Figure 46. The comparison of strains on free surface (WO) and silicon substrate (W) for two load values at –z direction (a) vertical strain (-z direction), (b) horizontal strain (-y direction)

the substrate, Figure 39. However, in future designs, the optimal location of the strain sensors would be the center of the silicon substrate.

5.4 Experimental Characterization

5.4.1 Wheatstone Bridge Model

The piezoresistive MEMS strain sensors, presented in this chapter, are based on the direct relationship between the resistance of sensing element and the strain within. However the change in the resistance cannot be measured because of relatively low resistance change with strain. Therefore by using Wheatstone bridge (Figure 47 (a)), the resistance-change in a resistance-based strain sensor is converted to voltage signal in order to increase minimum detectable strain level. The data acquisition system, used in this paper, is a NI USB 9162 linked with NI 9237. This device is designed for conventional strain gauges and equipped with a separate Wheatstone bridge for each channel tuned with 350 Ω resistors. One of the design parameters is to have strain sensors with a target resistance of 350 Ω. As a result the existing data acquisition system could be utilized for the sensors, which would eliminate the need to design a new bridge for each sensor. However the resistance measurements done on the manufactured sensors revealed that the errors engraved in the manufacturing process prevent the final products from having the exact designed properties, including the resistance. To adjust the resistance value of each sensor to the target resistance (i.e. 350 Ω) a secondary circuit is designed as displayed in Figure 47 (b). In this circuitry, R_x is the measured resistance of MEMS strain sensor, R'_x is the bridge resistance and equals to 350 Ω, R_s and R_p are series and parallel resistors, respectively, to bring the total resistance as 350 Ω.

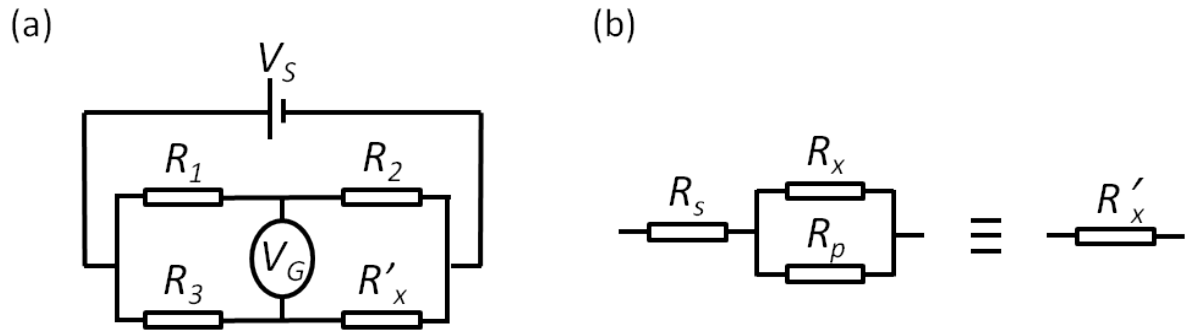

Figure 47. Schematics of electric circuit used to transform the change in resistance to voltage (a) Wheatstone bridge model, (b) additional circuit designed to adjust the resistance to the bridge resistance value as 350 Ω

In Figure 47 (a) the relationship between gauge voltage and other parameters of the circuit can be described as:

$$V_G = (\frac{(R'_x)}{(R_3 + R_x)} - \frac{R_2}{(R_1 + R_2)})V_S \tag{5.1}$$

where V_S is the power source voltage, V_G is the gauge voltage, R'_x is the equivalent resistance shown in Figure 47 (b), and the bridge resistances are $R_1 = R_2 = R_3 = R_0 = 350\Omega$. The above equation is simplified to:

$$V_G = (\frac{(R'_x)}{(R_0 + R'_x) - 0.5})V_S \tag{5.2}$$

If $R'_x = R_0 + \delta R'$ then

$$V_G = (\frac{1}{2 + \frac{4R_0}{\delta R'}})V_S \tag{5.3}$$

Considering R_0 as 350 Ω and $\delta R' \ll 350\Omega$, one can neglect the first term of the denominator (i.e. 2) in comparison to the second term (i.e. $\frac{4R_0}{\delta R'}$). Therefore the above equation is simplified to:

$$V_G = \frac{\delta R}{4R_0} V_S \tag{5.4}$$

Combining this equation with the gauge factor equation is obtained as:

$$GF = \frac{\frac{4V_G}{V_s}}{\epsilon} \tag{5.5}$$

Since the MEMS strain sensors resistances were different than Wheatstone bridge element's resistance, R_0, additional circuit is formed to adjust this resistance difference. In Figure 47 (b) the equivalent resistance is calculated by:

$$R'_x = R_s + \frac{1}{\frac{1}{R_p} + \frac{1}{R_x}} \tag{5.6}$$

where R_s is the series resistance, R_p is the parallel resistance, R'_x is the equivalent resistance which is aimed to be equal to R_0, and R_x is the measured resistance of MEMS strain sensor. The relation between the change in equivalent resistance R'_x is calculated as:

$$\delta R' = \frac{R_p R_p \delta R}{(R_p + R_x + \delta R)(R_p + R_x)} \tag{5.7}$$

In this study, R_p is set as equal to R_x, and R_s is varied to reach the equivalent resistance of 350 Ω. For the specific case of $R_p = R_x$, the resistance change in Equation 5.7 becomes:

$$\delta R' = \frac{1}{\frac{4}{\delta R} + \frac{2}{R_x}} \tag{5.8}$$

Since δR is very small in comparison to R_x, the above equation is simplified as:

$$\frac{\delta R'}{R'_x} \approx \frac{\frac{R_x}{R'_x}}{\frac{4R_x}{\delta R}} \tag{5.9}$$

Equation 5.9 can be rewritten in terms of resistance change of MEMS strain sensors as:

$$\frac{\delta R}{R_x} \approx 4\frac{R'_x}{R_x}\frac{\delta R'}{R'_x} \tag{5.10}$$

One of the MEMS strain sensors has R_x as 412 Ω, and the resistance change is computed as:

$$\frac{\delta R}{R_x} \approx 3.3654\frac{\delta R'}{R'_x} \tag{5.11}$$

Another MEMS strain sensor has R_x as 447 Ω, and the resistance change is computed as:

$$\frac{\delta R}{R_x} \approx 3.132\frac{\delta R'}{R'_x} \tag{5.12}$$

These equations are used in the following section in order to compute the gauge factors of the MEMS strain sensors.

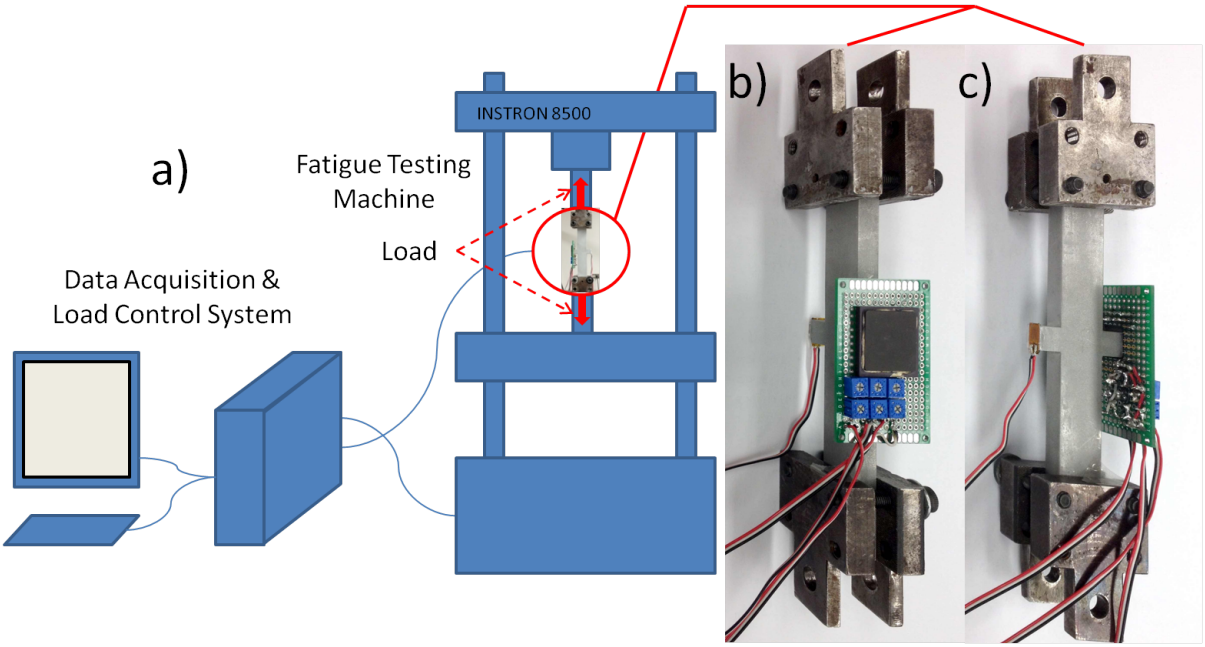

Figure 48. Experimental setup for strain measurement under monotonic and cyclic loading (a) schematic of the experimental setup, (b) the MEMS package attached to the wing of the specimen, (c) the rotated view to illustrate the geometry of the specimen and the location of the metal gauge

5.4.2 Response to Cyclic Loading and Step Loading

The MEMS strain sensors were connected to the additional circuits shown in Figure 47 (b), and then mounted onto aluminum 1100 specimen as illustrated in Figure 48 (b) and (c). The specimen was installed in the testing machine, Instron 8500 (Figure 48 (a)) for monotonic and cyclic loading. The load was linearly increased and decreased from 1 kN to 10 kN and vice versa.

Figure 49 demonstrates the strain reading of MEMS strain sensors along with conventional strain gauge. During the initial testing, the gauge factor of the MEMS strain sensors were inputted as 1; therefore, the strain reading equals the resistance change (see Equation 2.10). Although the MEMS strain sensors followed the trend of conventional strain gauge, a considerable amount of drift was observed as shown in the inset figure. A simple segment wise linear regression correction method was implemented to remove the drift. Various parameters can contribute to the observed drift. After a comprehensive study, the temperature appeared to have the highest impact on the drift, which is discussed in 5.4.3. Other influencing parameters include the stabilization of the data acquisition system as well as the thermal steady state condition of the sensors under a constant electrical load. Complementary tests revealed that when a sensor undergoes a change in the electrical load, the power consumed by the sensor changes, which leads to a change in the thermal condition of the sensing element. Although that can be categorized as a part of thermal effect, since thermal effect is usually referred to the change due to environmental temperature, it is preferred to be categorized as electrical load stability effect. In order to calibrate the sensors for, the system was left running for at least an hour, which smoothed out the drift behavior.

The next experiment was implemented to compare the gauge factors of conventional strain gauge and MEMS strain sensors. The tensile load was increased and decreased as a step load in the order of 0 kN to 12 kN with 4 kN increments, and then 12 kN to 0 kN with 4 kN increments. The measured strains of all the sensors are plotted in Figure 50. Similar to cyclic loading, the gauge factor of the MEMS sensors was inputted as 1 to the data acquisition system. The

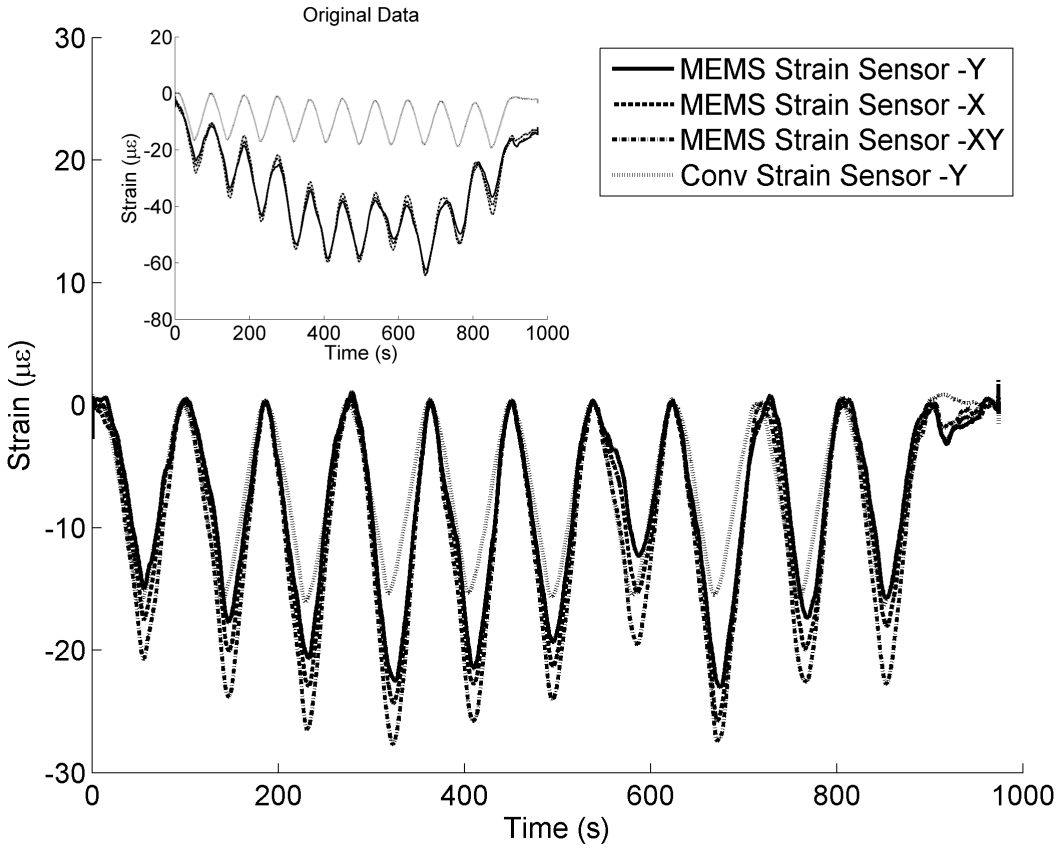

Figure 49. Strain measurements due to cyclic loading including the original (inset figure) and corrected data

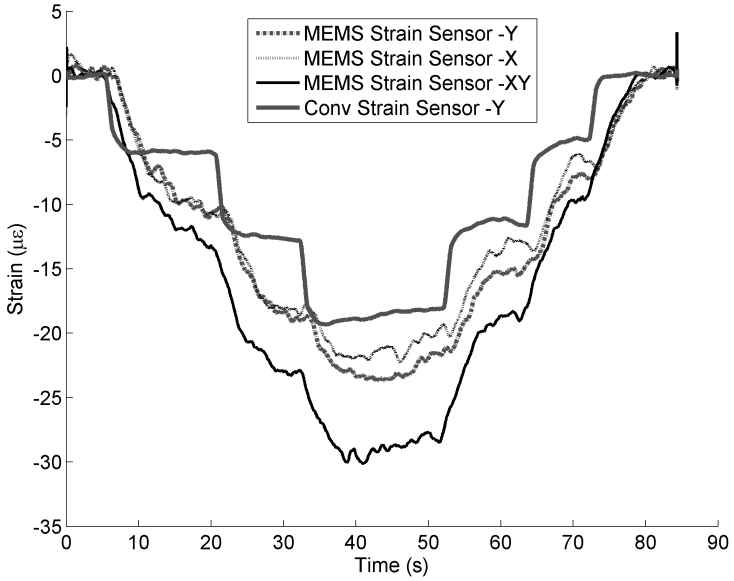

Figure 50. Strain measurements of MEMS strain sensors and conventional metal gauge under monotonic loading

conventional strain sensor exhibits step-like behavior when the load is increased and stayed constant. The MEMS strain sensors have higher noise levels due to the thermal-mechanical effect. In order to reduce the noise level, the data is averaged, which negatively affects the observation of step-like behavior when strain is suddenly changed.

The $\frac{\Delta R}{R_0}$ verses applied load is plotted to demonstrate the hysteresis behavior of the sensors. The hysteresis determines the stability and reliability of the sensor. Mohammed et al. [54] showed on the doped single crystal silicon that lower dopant concentrations have higher hysteresis due to nonlinear behavior of the sensor, which is caused by the leakage current with

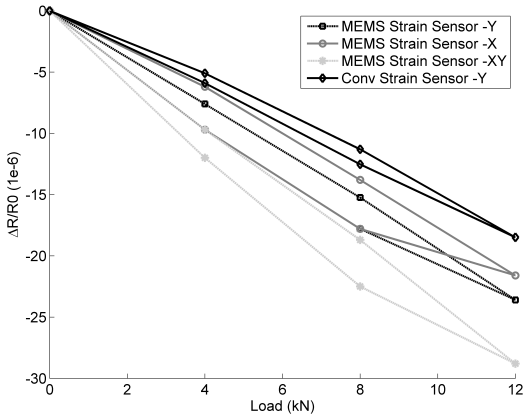

Figure 51. Hysteresis behaviors in terms of $\frac{\Delta R}{R_0}$ verses step loads for loading and unloading process

the operating temperature. The dopant type and level of polysilicon layer for MetalMUMPS are phosphorous (n-type) and $8 \times 10^{-15} cm^{-3}$, which is relatively low dopant concentration. Therefore, hysteresis of the piezoresistive strain sensors manufactured with MetalMUMPs is inevitable.

The gauge factor, as Equation 2.10 explains, is the ratio of $\frac{\Delta R}{R_0}$ divided by the strain within the material where the sensors are mounted. Since there was no practical way to have the exact value of the strain in all three directions in the presence of the MEMS sensor package, the measured value of the strain from the conventional strain gauge was used as the base to calculate the gauge factor. Although the conventional stain gauge is used as the base for the calculations, this introduces bias into the analysis in two ways. First, the conventional strain

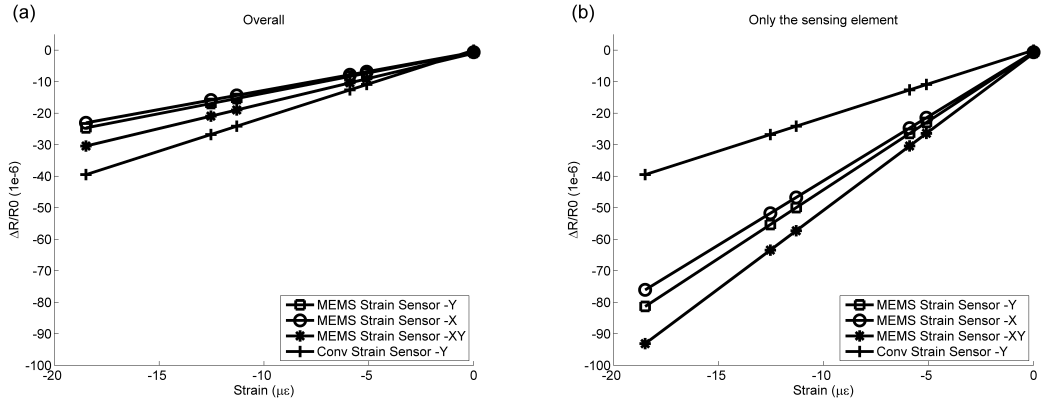

Figure 52. The gauge factor plots (the slope of the lines) (a) overall reading using equivalent resistance, (b) calculated for only the sensing element using the resistance of the MEMS strain sensors

gauge is mounted on the opposite side of the wing. Second, the metal gauge is only sensitive to the direction of the applied load. Figure 52 demonstrates the results of gauge factor when the $\frac{\Delta R}{R_0}$ is transformed to the value of solely the sensors (see Equation 5.10) and not the measurement values, which is done through the additional circuit.

The calculated gauge factors are summarized in Table XIII. The gauge factors of the MEMS strain sensors are still approximately twice that of the conventional strain gauges even though significant loss of strain transfer due to the MEMS package, and the location of MEMS strain sensors on the silicon substrate. The gauge factor of polysilicon depends on the piezoresistive coefficient, the film structure, and the process variables (e.g., annealing temperature, deposition temperature). The piezoresistive coefficient of polysilicon also depends on the dopant transport

TABLE XIII

GAUGE FACTOR OF THE MEMS STRAIN SENSORS AND METAL GAUGE

Gauge Factor	MEMS strain sensors			Conventional metal gauge
	-y direction	-x direction	-xy direction	
Circuit level	1.2956	1.2120	1.5912	2.135
Sensor level	4.3603	4.0788	4.9837	2.135

across the grain boundary (controlled by the process variables), dopant concentration, and dopant type. For instance, French and Evans [37] reported that the longitudinal gauge factor is near -10 for phosphorus doped material with 1026 m^{-3} dopant concentration, 60 nm grain size and <110> orientation. Considering all the variables and values reported in the literature, the gauge factor in the range of 4-5 is acceptable.

5.4.3 Response to Thermal Loading

The temperature effect is a source of error in strain measurement, which should be taken into account. The sensing element of the MEMS strain sensors is made of polysilicon, which has piezoresistivity property dependent on temperature [29], [54], [34]. Temperature coefficient of resistance (TCR) is a parameter, which quantifies the temperature sensitivity effect and is calculated as:

$$TCR = \frac{\frac{\Delta R'}{R}}{R'_x} \tag{5.13}$$

where ΔT is the temperature change which is calculated by the difference of the final temperature and the initial (room) temperature. TCR is often expressed in terms of $ppm/^{\circ}C$.

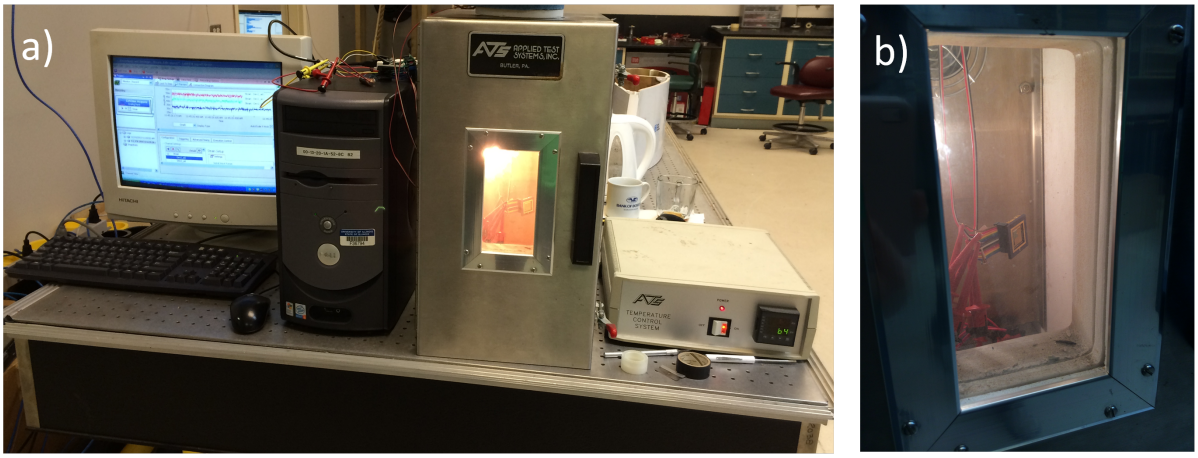

Figure 53. The experimental setup for measuring the TCR of the MEMS strain sensors

The MEMS device with open lid was suspended in a temperature chamber of Applied Test System Inc. (Figure 53). The reference room temperature was 25°C. The internal temperature of the chamber was raised in 5°C increments from 40°C to 60°C. This was followed by cooling cycle, which was slower than the heating cycle. Figure 54 shows the thermal loading cycles together with the measured strain values of the MEMS sensors when the gauge factor was set to 1 (i.e. $\frac{\Delta R}{R_0} = \epsilon$). It should be noted that while the temperature range implemented in this experiment is narrow, the range includes a significant part of the temperature, which the sensors can be exposed to the SHM of civil structures, such as highway bridges. Also the literature [29], [54] reports that the piezoresistive property of polysilicon has close to linear relationship with temperature in the range of -50°C to 50°C. Figure 55 demonstrates the thermal loading/unloading behavior of the MEMS strain sensors. The TCR is calculated by

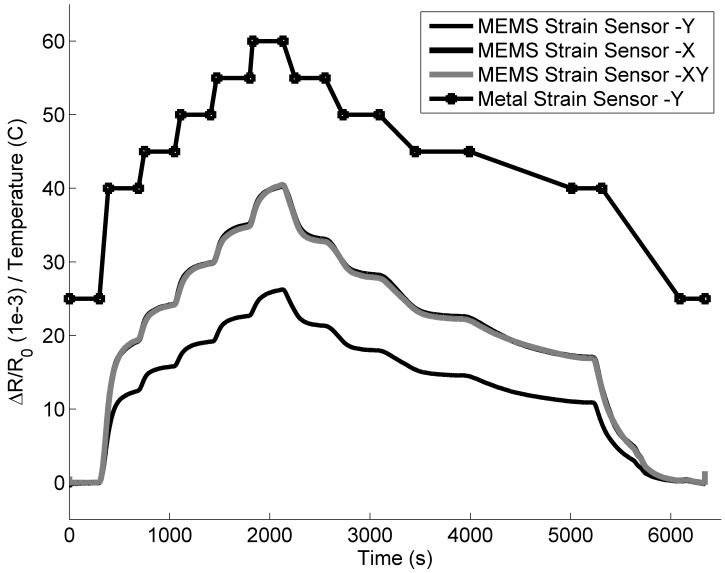

Figure 54. The responses of MEMS strain sensors to thermal loading

implementation of a linear regression as the slope of the lines in Figure 55(b). The TCR values are calculated as 738.0, 1140.3, and 1134.7 $ppm/^{\circ}C$ for -y, -x and -xy direction sensors, respectively. The measured TCR values is the summation of thermal expansion differences of multiple layers (i.e., ceramic package, thin silver epoxy, silicon substrate and polysilicon layer), and the thermionic emission of the carriers [29]. The TCR values fall within the range of the values reported in the literature [54]. Figure 55 shows that the MEMS strain sensor responds to temperature change linearly as compared to metal gauges [54]. The linear behavior enables the application of correction method to the strain data if the ambient temperature is measured.

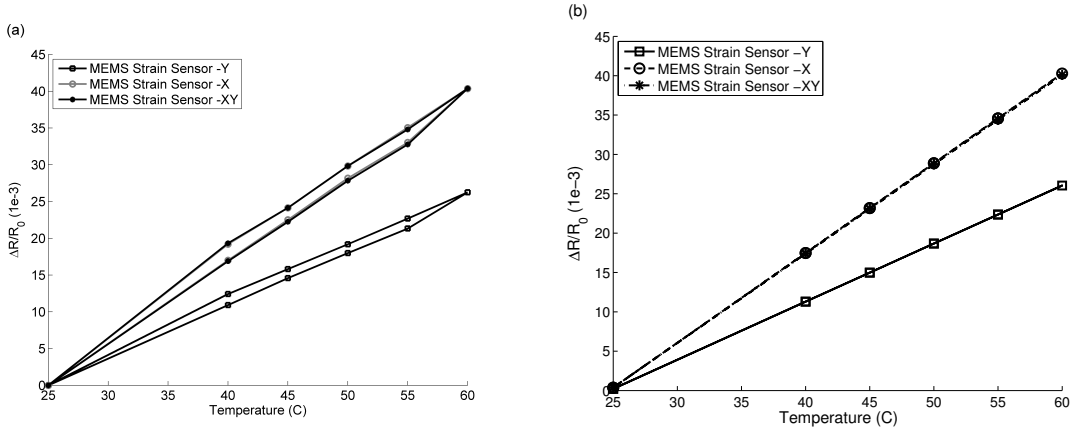

Figure 55. Dimensionless resistance of MEMS strain sensors with respect to temperature (TCR) (a) recorded data illustrating the thermal loading/unloading cycles, (b) linear regression to derive the TCR values

5.4.4 Application to Fatigue Loading

The MEMS strain sensors with similar setup as Figure 48 (with the exceptions of aluminum 7075 as material, half of thickness and only one cube added at the mid-height to mount the MEMS device) were tested under the fatigue loading in order to test the sensors' performance under higher sampling rate and longer duration. The specifications of the fatigue loading were 3 Hz frequency, 5.25 kN mean load and ± 2.25 kN alternating load. The data was collected about 900 seconds. The overall behavior of the MEMS strain sensor oriented in -y direction is shown in Figure 56. The load was constant about 20 second and then the fatigue test was started. The fatigue cycles are clearly seen in the data; however, a significant thermal drift is

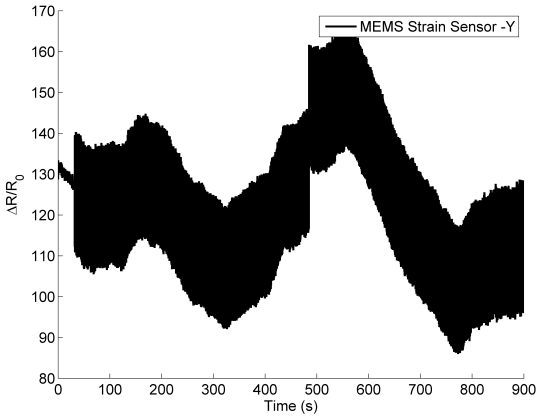

Figure 56. Normalized change in resistance verses time illustrating the thermal drift in a fatigue test of a 3 Hz and 5.25±2.25 kN tensile loading

observed. The thermal drift occurred for all the sensors, which means that a proper full bridge model built-in on the MEMS device can be utilized to cancel the thermal drift.

When the data window is narrowed, the fatigue cycles are clearly detected by the MEMS strain sensors. Figure 57 shows the six fatigue cycles recorded from the MEMS strain sensors. The inset figures show the resistance changes of the MEMS strain sensors with respect to load cycles. Similar to the results obtained from the monotonic loading, the MEMS sensors have significant hysteresis, which is caused by a combination of complex variables such as piezoresistive effect at different load directions, friction between parts etc. The hysteresis can be compensated by numerical models such as the inverse Preisach model [55]. While the sensors exhibit hysteresis, they have repeatable behaviors from one cycle to another. The

fatigue testing shows that the MEMS strain sensors can be utilized as fatigue cycle counts and the determination of load range that a structure is exposed to while measuring true strain is a challenge because of the influence of thermal drift, multiple-layers for strain transfer and hysteresis.

5.5 Summary

The analytical, numerical and experimental characterization of the MEMS strain sensors made of polysilicon layers and manufactured with MetalMUMPs are presented. Three sensors are oriented in -x, -y and -xy directions in order to extract the principal strains. The numerical results show the influence of trenching and the sensor location on the silicon substrate for the most efficient strain transfer from the structural surface to the sensing element. The numerical and experimental results validate that the strain sensors should be placed at the center of the silicon substrate in order to remove the edge effect. The responses of the MEMS strain sensors under mechanical and thermal loads are evaluated. Considering the strain loss due to the interfaces of the MEMS package and layers, the gauge factor is measured in the range of 4-5. The temperature dependence of the MEMS strain sensors is significant. However the temperature dependency of polysilicon properties requires additional compensation to eliminate the unwanted effect from the signal. Since the temperature variation happens at a slower rate than that of the strain change in the SHM applications, the MEMS strain sensors can be utilized to function as strain and temperature sensors. This can be achieved by decoupling the signal into strain signal due to load change in the structure (higher frequency) and the temperature signal due to gradual change of ambient temperature (lower frequency). Although the MEMS

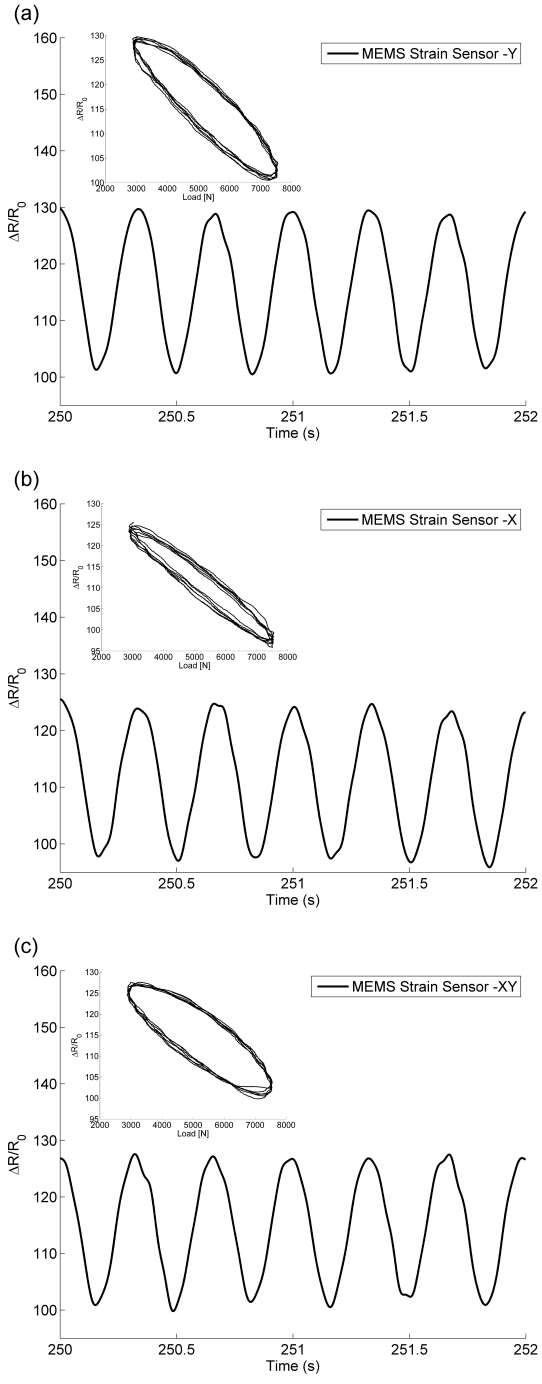

Figure 57. Fatigue test time domain strain data with sub figure of repeated hysteresis behavior, (a) -y, (b) -x, (c) -xy MEMS strain sensor

strain sensors have limitations on measuring true strain, the MEMS strain sensors can make good measurements of driving force estimates and fatigue cycle counts.

CHAPTER 6

THE IMPLEMENTATION OF THE MEMS DEVICE FOR THE DETECTION OF FATIGUE CRACK GROWTH

The content of this chapter is partially presented in the sixth world conference on structural control and monitoring [4].

6.1 Introduction

In the previous chapters, the characterizations of individual MEMS sensors are presented. In this chapter, the ability of the MEMS AE and strain sensors in order to detect the initiation and growth of fatigue crack and develop intelligent data acquisition approach is evaluated. Two notched aluminum 7075 coupon samples are tested under fatigue loading until the failure. The performances of the MEMS sensors are compared with conventional piezoelectric AE sensors and metal gauge.

6.2 Experimental Design

Two aluminum 7075 coupon samples with the dimensions of 170 mm x 20 mm x 5 mm were tested under fatigue loading. A small wing with the dimensions of 1 mm x 5 mm x 5 mm was added to the middle section in order to attach the MEMS device. In order to initiate crack growth, two notches were introduced by sawing the specimen. Figure 58 shows all the data acquisition systems, and the sensor locations. The loading machine was Instron 8500. The AE data was collected using PCI-8 board manufactured by Mistras Group Inc. The strain data

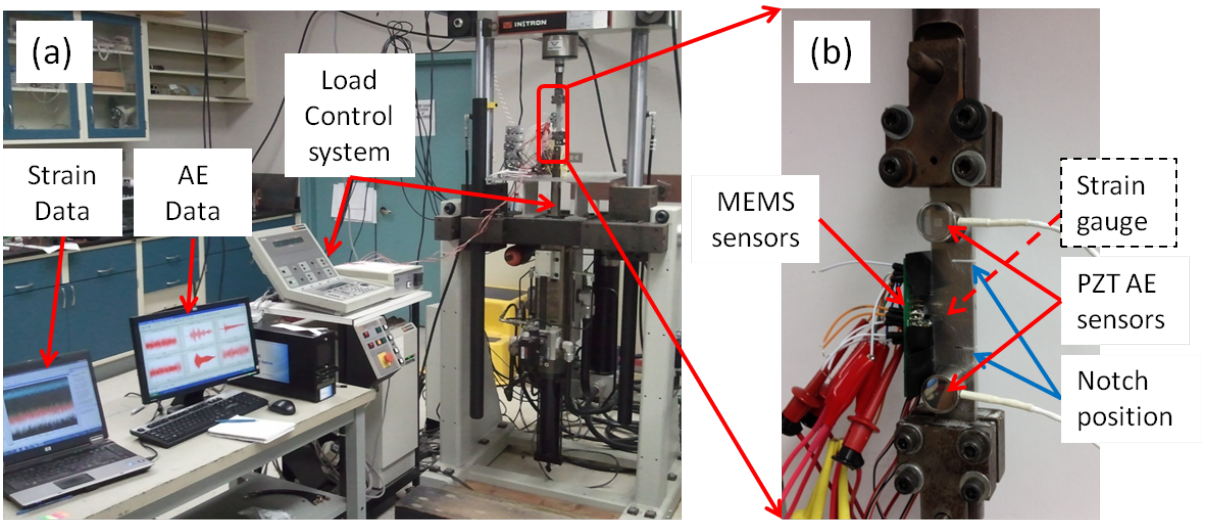

Figure 58. Experimental setup (a) the data acquisition and load control systems, (b) specimen with the sensors attached on it

was collected using National Instrument NI USB 9162 linked with NI 9237 high speed data acquisition board. In addition to the MEMS sensors, two WD (wideband) AE sensors on top and bottoms of the specimen between the grips and the notches, and a regular metal strain gauge (CEA-13-187-UW-350 strain gauges with the resistance of $350 \pm 0.3\Omega$) were bonded to the specimen. All the sensors were adhesively attached to the specimen. The specifications of the fatigue loading were 3 Hz frequency, 4.5 kN mean load and ± 2.25 kN alternating load.

The electrical circuit schematic of the experimental setup is illustrated in Figure 59. In this figureAE and strain data were collected using two separate data acquisition systems; however, a single instrument could be capable of collecting both AE and strain data.

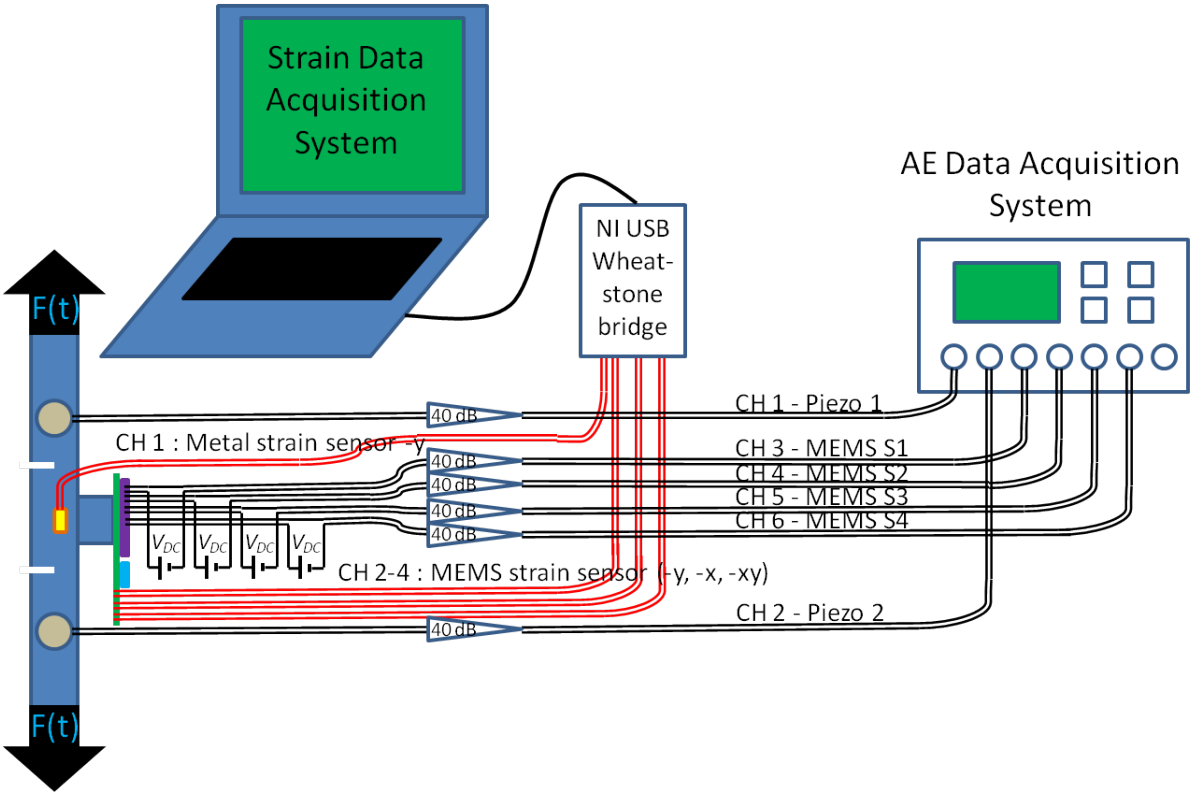

Figure 59. The electrical circuit schematic of the experimental setup

6.3 Fatigue Test I Results

6.3.1 MEMS AE Sensors in Comparison to Piezoelectric AE Sensors

If the sensitivity of an acoustic emission sensor is defined as the magnitude of the output signal of the sensor to the energy released by the excitation source, then the piezoelectric sensors have higher sensitivity than the MEMS AE sensors presented in this work. However this definition is not always the best since, as it is explained in the chapter 3, other factors, such as signal to noise ratio, may be a better parameter to compare the piezoelectric sensors and the MEMS AE sensors. In this section, the dynamic range and the ability of detecting the crack initiation and propagation of two sensor types are compared.

6.3.1.1 Dynamic range

In order to transfer the signal from the sensor to the data acquisition system through long cables, the signals from the sensors need to be amplified. In this study, the signals are amplified by 40 dB before connecting the sensors to the data acquisition system. The selection of 40 dB amplifier limits the maximum dynamic range to 100 dB. The detectable "Dynamic Range" (DR) for AE systems is the range between the threshold above noise level (dB) and the maximum dynamic range of the data acquisition system. Since the maximum amplitude of captured signal is limited to 100 dB, the lower the noise level, the larger the DR. Table XIV presents the threshold level for all the AE sensors when the loading machine is operational. The friction at the grip locations cause higher threshold setting for the piezoelectric sensors as they are more sensitive than the MEMS sensors. This friction produces such a high amplitude and low frequency emission that leads to the threshold level for the piezoelectric sensors to be

TABLE XIV

AE SENSOR AND CHANNEL DESCRIPTION OF THE FATIGUE TEST I

Channel	Type	Feature	Threshold above noise (dB)
1 (bottom)	Piezo	Wideband	68
2 (top)	Piezo	Wideband	52
3	MEMS	S1 - 60 kHz, OOP	35
4	MEMS	S2 - 150 kHz, OOP	35
5	MEMS	S3 - 150 kHz, Gap change, IP	35
6	MEMS	S4 - 100 kHz, Area change, IP	35

set to values approximately twice as high as the MEMS AE sensors, thus leaving these sensors with approximately half of the DR of the MEMS AE sensors. As the bandwidth of the MEMS sensors is limited, they are not sensitive to the friction emissions. Figure 60 illustrates the peak frequency of the hits recorded by all six channels. Piezoelectric sensors, especially piezo 2, have peak frequencies near 20 kHz. The piezo 2 was closer to the moving grip; therefore, it experienced more frictional noise. However, out-of-plane MEMS AE sensors (S1 and S2) have peaks at their resonant frequencies, in-plane MEMS AE sensors (S3 and S4) have peaks at two frequencies representing in-plane and out-of-plane motions.

6.3.1.2 The Ability to Detect the Fatigue Crack Initiation

One of the advantages of the AE method is the ability to detect the early stage of damage before the other NDE methods and visual inspection. Table XV shows the time and AE signal magnitude of each event detected by the sensors. The first event that the piezoelectric AE sensors detected occurred at 686 seconds. The MEMS S2 sensor also detected this event, which

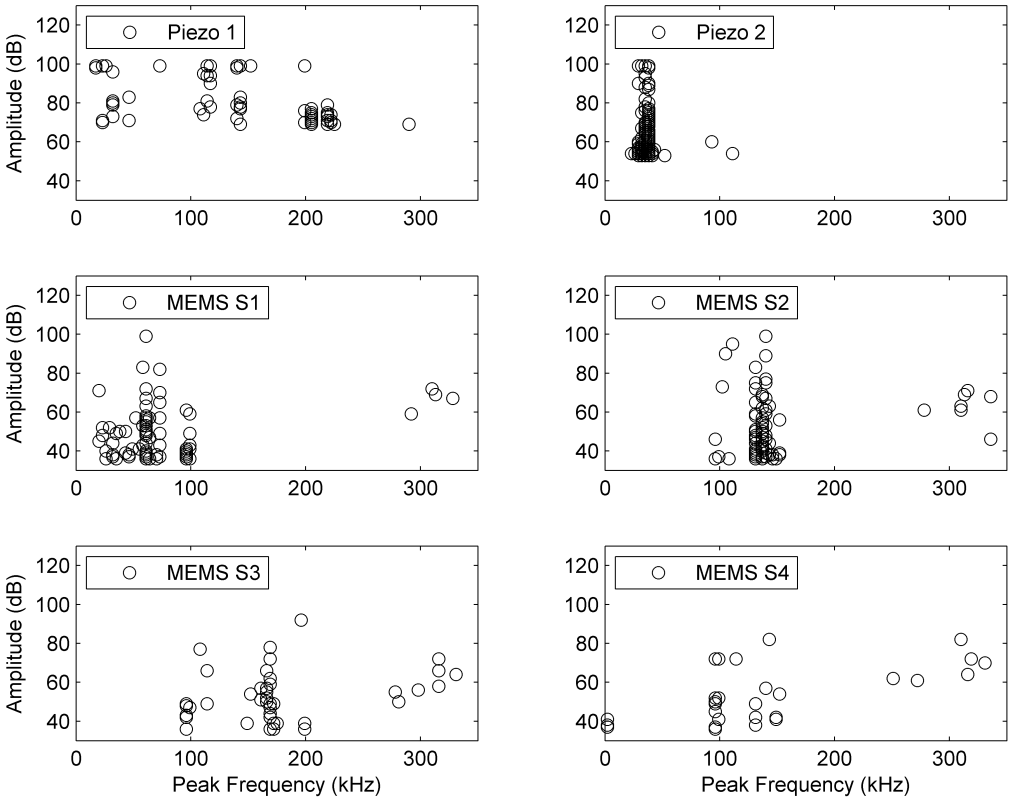

Figure 60. Peak frequency versus amplitude plots for all the AE sensors for the fatigue test I

TABLE XV

AE SENSOR AND CHANNEL DESCRIPTION OF THE FATIGUE TEST I

Time (sec)	Amplitude (db)					
	piezo 1	piezo 2	MEMS S1	MEMS S2	MEMS S3	MEMS S4
686.837	74.864	65.6228	-	37.6501	-	-
722.498	95.475	87.1344	48.2796	61.7325	49.6913	35.2663
⋮	⋮	⋮	⋮	⋮	⋮	⋮
823.519	99.2658	99.2285	63.3882	72.5578	59.4904	39.2337
⋮	⋮	⋮	⋮	⋮	⋮	⋮
858.191	99.2461	99.2914	67.3872	75.6988	62.6974	42.3606
⋮	⋮	⋮	⋮	⋮	⋮	⋮
880.511	99.2412	98.4763	85.7426	42.3606	85.8352	61.4005

is relatively low amplitude. The next event was detected at 722 seconds, and all the MEMS AE sensors detected this event. The next phase of testing included the fatigue crack growth phase, and all the sensors detected those events.

While the amplitudes of the MEMS AE sensors are smaller than piezoelectric AE sensors, they can detect the initiation of fatigue crack due to wider dynamic range and lower threshold as discussed above.

6.3.1.3 Damage evolution

Figure 61 illustrates the AE amplitudes of all the sensors with respect to time. The majority of the AE events were detected near 800 seconds of testing (i.e., two minutes before the failure). The aluminum 7075 is a brittle material; therefore, the fatigue crack grew fast after its initiation.

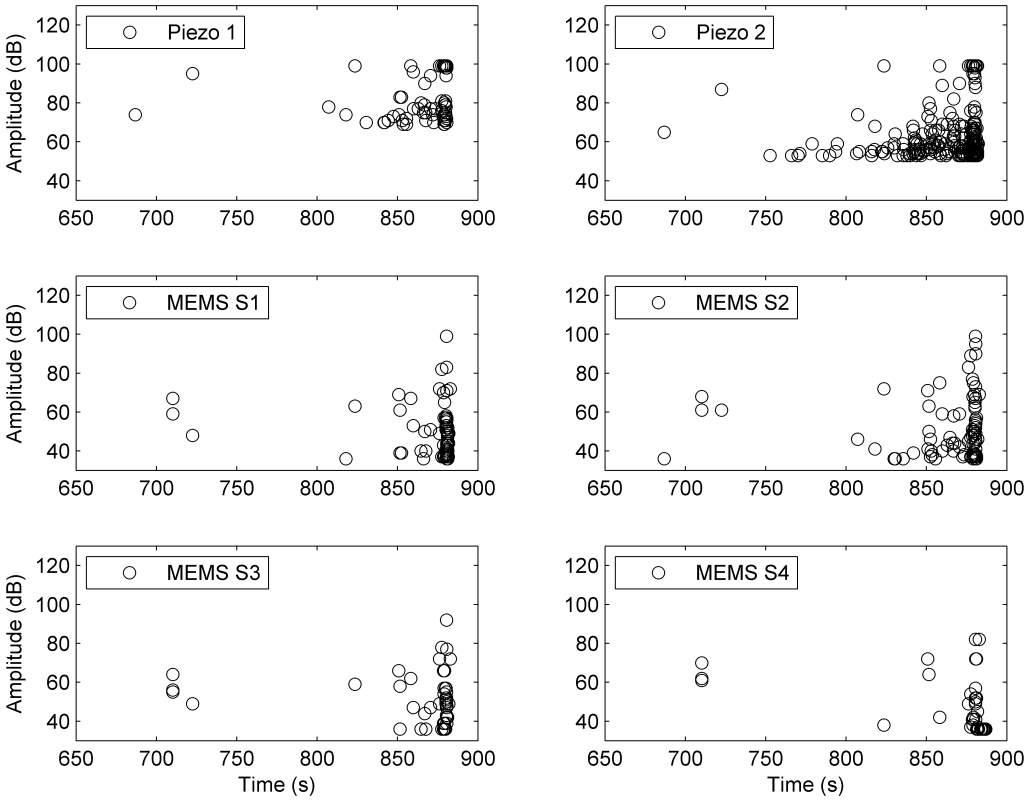

Figure 61. AE amplitude versus time for the fatigue test I

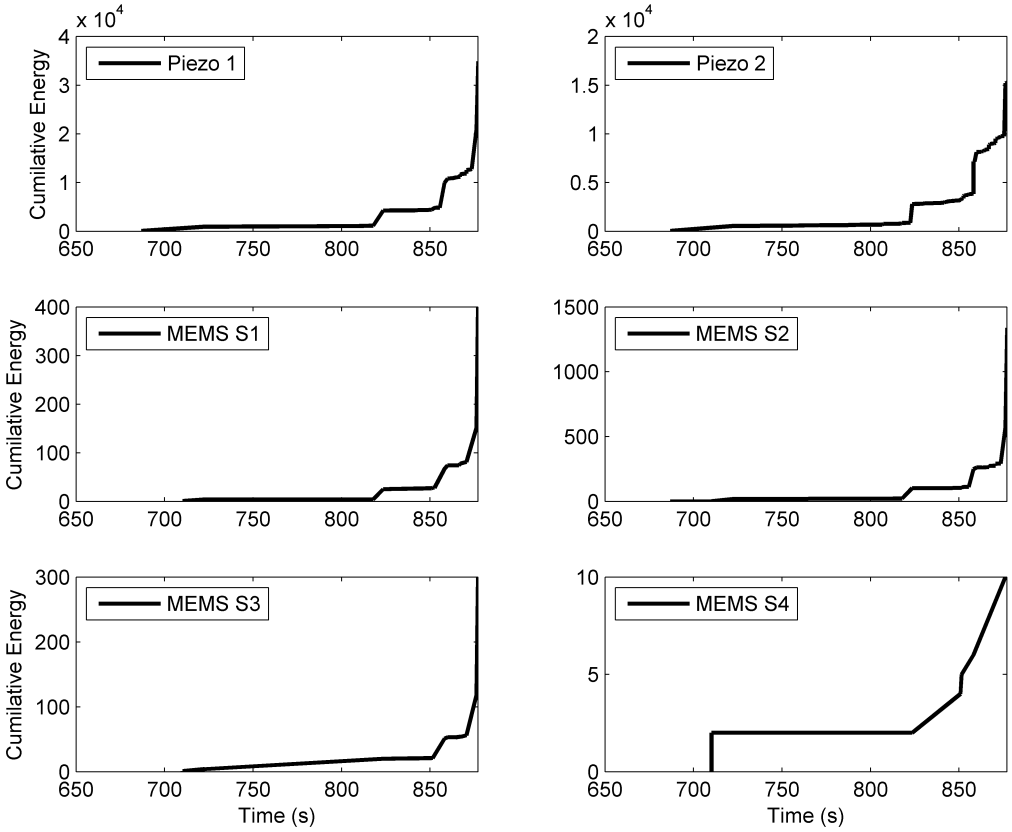

Figure 62. Cumulative AE energy of each sensor versus time for the fatigue test I

Figure 62 shows the cumulative energy of all the AE sensors with respect to time. All the sensors clearly show similar patterns including three steps of fatigue crack behavior: initiation, growth and fracture.

Figure 63 shows a cross sectional view of the aluminum 7075 specimen after the fracture. The aluminum 7075 is a high strength and quasi-brittle material [56]. In this picture, the

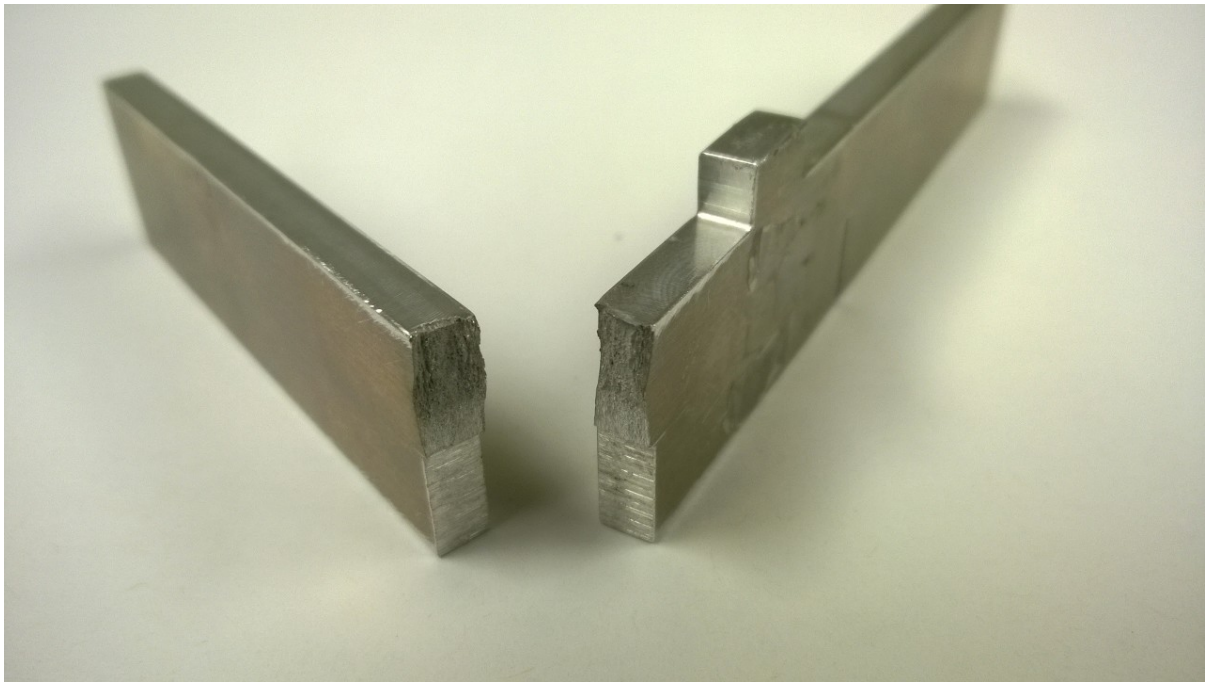

Figure 63. The failure section of the fatigue test I

bottom half of the cross sectional area is the artificially introduced notch (zone 0). The next 3-4 mm of the height is the initiation and growth area (zone 1). The remaining 6-7 mm of the height of the cross sectional area is the length of fracture area (zone 2). There is a clear change of color in the metal between the zone 1 and zone 2. Also the surface of zone 1 is similar to brittle fracture while the zone 2 is very similar to a cone-and-cup surface of a ductile material. Future metallurgical study is required to better understand behavior of the aluminum specimen and its fracture phases.

6.3.1.4 Waveform Characteristics

Figure 64 shows the time domain waveforms and the frequency spectra of the first event detected at 686 seconds. The piezoelectric sensors exhibit complex frequency spectra while the MEMS sensor has a narrowband response with no response to frequencies below 100 kHz. Zero-response below 100 kHz allows setting low threshold value in order to sense only the emission due to crack initiation and growth, which is represented by a wideband source function.

Figure 65 shows the time domain and the frequency spectra of the second event detected at 722 seconds. This event has higher energy release than the first event. The amplitudes of all the sensors are shown in Table XV. The MEMS S1 and S2 sensors have narrow bandwidth responses at their design frequencies. The amplitude comparison shows the intensity change of different events. The behaviors of the MEMS S3 and S4 sensors (in-plane sensors) are more complex due to their coupled behaviors to in-plane and out-of-plane motions.

6.3.2 MEMS Strain Sensors in Comparison to Strain Gauge

The comparison of the MEMS strain sensors and the metal strain gauges is discussed in detail in chapter 5. In this section, their comparison is performed for a longer testing and a realistic loading condition.

Figure 66 shows the overall strain histories of the metal gauge and MEMS strain sensors. Both sensor types exhibit a level of drift while the level of drift is higher for the MEMS strain sensor. As discussed earlier, the MEMS strain sensor has thermal drift problem. However, when a narrow window of sensor response is compared in , both sensors detect the fatigue cycles. Figure 67 illustrates a narrow window of strain history due to fatigue loading detected by three

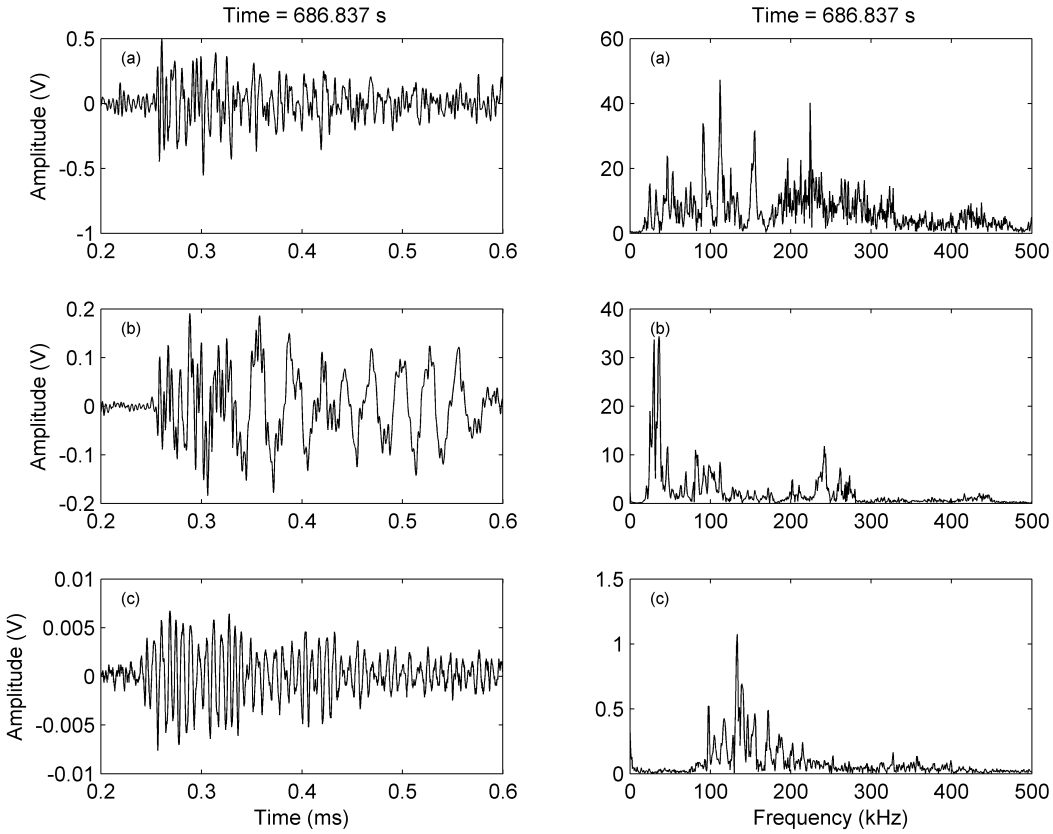

Figure 64. Time domain signals and their frequency spectra of the first event detected at the fatigue test I (a) piezo 1 (b) piezo 2, (c) MEMS S2

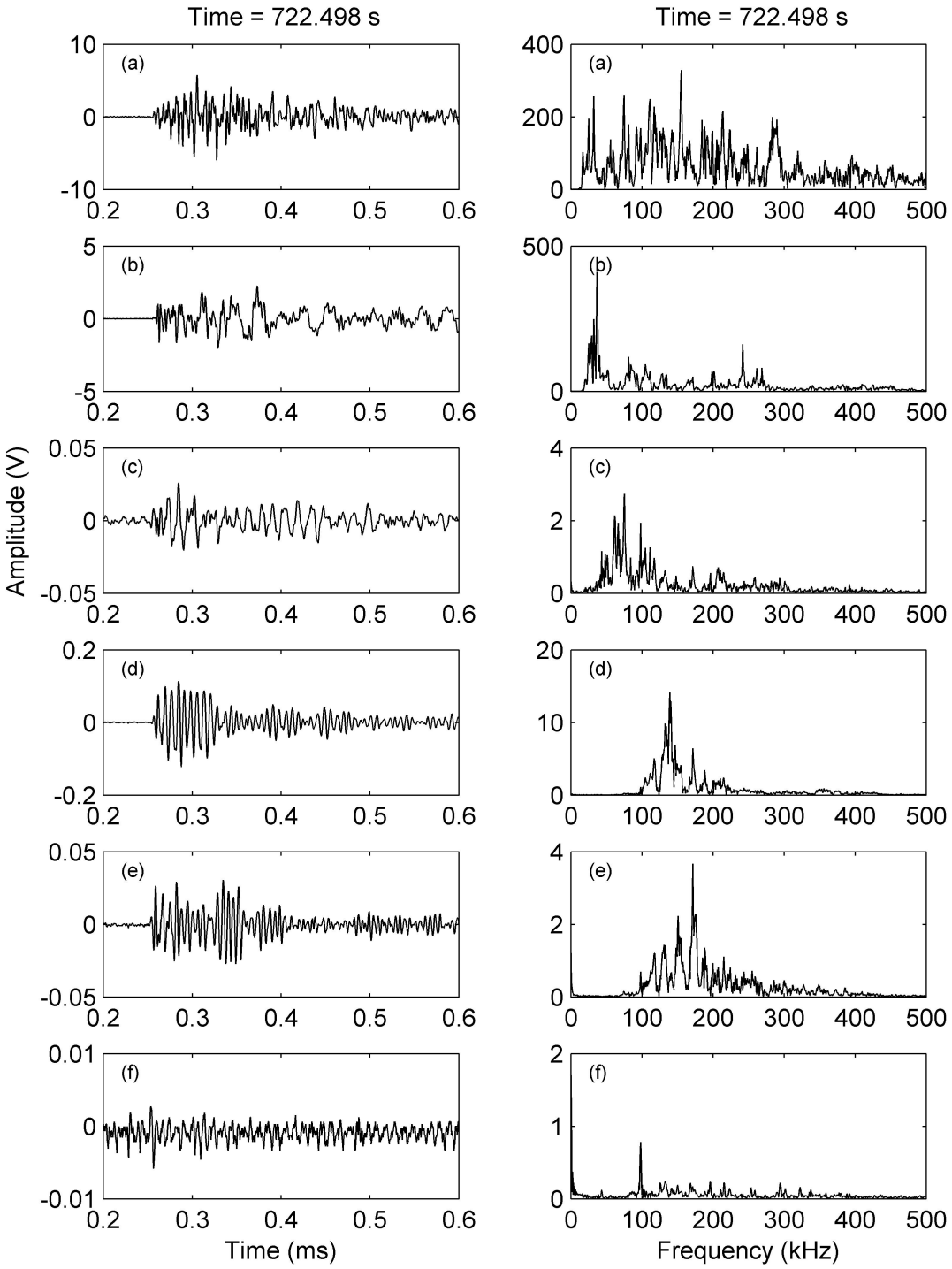

Figure 65. Time domain signals and their frequency spectra of the second event (a) piezo 1 (b) piezo 2, (c) MEMS S1 (d) MEMS S2 (e) MEMS S3 (f) MEMS S4

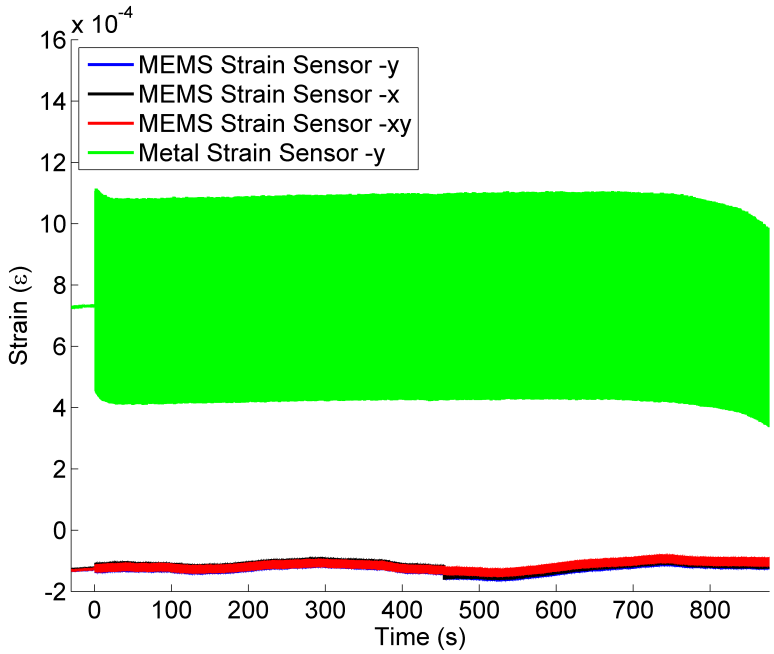

Figure 66. MEMS strain sensors comparison with metal strain sensor versus time for the fatigue test I

MEMS strain sensors and a conventional metal-base strain gauge. The metal strain gauge is attached to body of specimen while the MEMS sensors are attached to wing on the side. The strain amplitudes, that both strain sensor types are exposed to, are different. Therefore, the amplitude of metal gauge is higher than the amplitudes of MEMS strain sensor. Figure 68 shows the normalized and scaled strain histories. The MEMS strain sensors follow the same pattern of metal gauge.

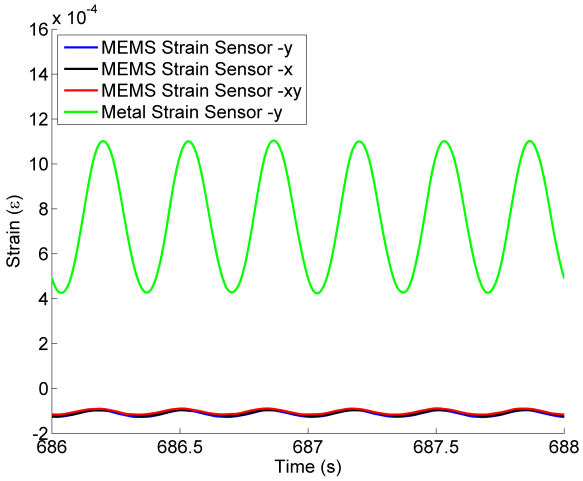

Figure 67. Windowed time histories of metal gauge and MEMS strain sensors for the fatigue test I

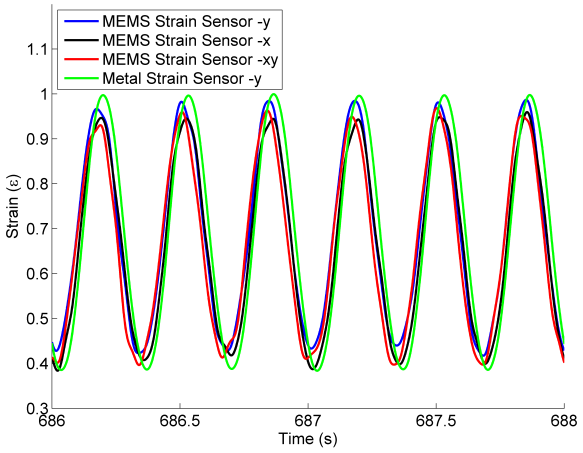

Figure 68. Windowed, normalized and scaled time histories of metal gauge and MEMS strain sensors for the fatigue test I

The expected life of the structure under fatigue loading can be calculated by the Paris law [57]:

$$\frac{da}{dN} = C(\Delta K)^m \tag{6.1}$$

where a is the crack length, N is the number of fatigue cycles, C and m are material conctants, and ΔK is the stress intensity factor range. The stress intensity is a factor of material, geometry and applied load.

A strain monitoring system can provide both the number of cycles in the load and the variation of applied load and subsequently the stress intensity factor range. Therefore strain monitoring is an important component of the SHM systems.

6.3.3 The Combined Behavior of MEMS AE and Strain Sensors

As discussed earlier, it is important to detect only relevant AE data in order to reduce the data set, and understand the AE data/damage relationship with minimum post-processing methods. Typical data acquisition for AE systems is based on threshold crossing: if the signal level at a sensor output channel is higher than the pre-set threshold level, the data acquisition system acquires AE data. This approach can cause high hit-rate and recording of irrelevant data; relevant data in this case include the propagating elastic waves due to newly formed damage surfaces. Strain-based triggering mechanism where AE data is recorded when strain (i.e., load) level is high significantly reduces the collection of irrelevant data, which further reduces the size of data collected, and increases the reliability of AE sensing.

Figure 69 shows the first AE event detected by the MEMS S2 sensor on the strain history of the MEMS strain sensor. As expected, the AE event due to the initiation of fatigue crack

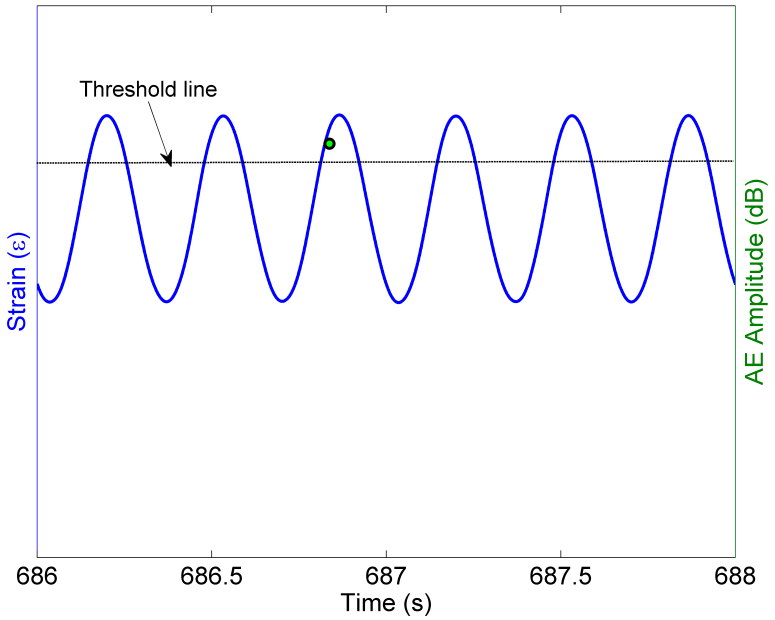

Figure 69. The MEMS strain history in the window of the first AE event detected by the MEMS S2 transducer for the fatigue test I

occurs at high load level. A detection threshold as shown in the figure can be set using the strain data in order to activate the detection of the AE data, which can significantly reduce the acquisition of the irrelevant data.

6.4 Fatigue Test II Results

In this section, the experiment explained in the previous section is repeated. The focus of this section is to determine repeatability of the performances of the MEMS sensors.

TABLE XVI

AE SENSOR AND CHANNEL DESCRIPTION OF THE FATIGUE TEST II

Channel	Type	Feature	Threshold above noise (dB)
1 (top)	Piezo	Wideband	65
2 (bottom)	Piezo	Wideband	72
3	MEMS	S1 - 60 kHz, OOP	43
4	MEMS	S2 - 150 kHz, OOP	35
5	MEMS	S3 - 150 kHz, Gap change, IP	35
6	MEMS	S4 - 100 kHz, Area change, IP	35

6.4.1 MEMS AE Sensors in Comparison to Piezoelectric AE Sensors

6.4.1.1 Dynamic Range

Table XVI shows the noise threshold level for all the six AE sensors. The noise level in this experiment is close to that of the first experiment. Therefore the dynamic range for the MEMS AE sensors are approximately twice of that of the piezoelectric AE sensors.

Figure 70 illustrates the peak frequency of the hits recorded by all six channels. As expected channels 1 and 2 have a broadband peak frequency range. The peak frequency of hits detected by MEMS S1 and S2 are mostly gathered around their resonant frequencies. And MEMS S3 and S4 both show peak frequency concentrations near two frequencies (first two modes of vibration: in-plane and out-of-plane direction).

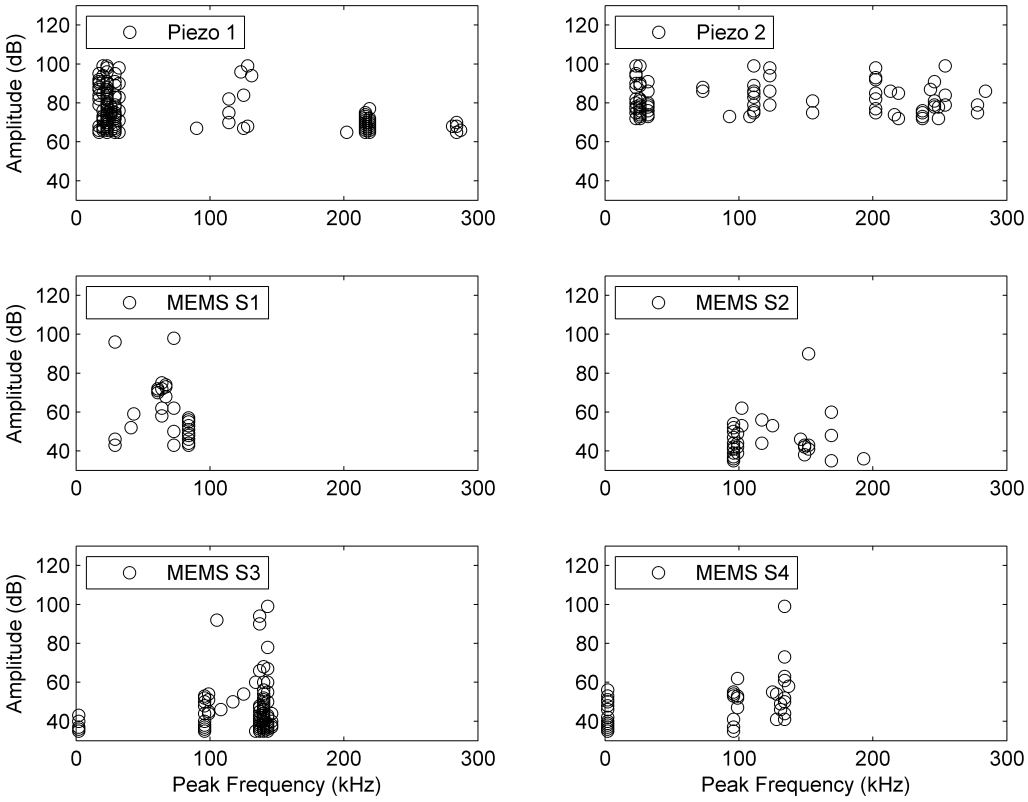

Figure 70. Peak frequency versus amplitude plots for all AE sensors for the fatigue test II

6.4.1.2 The Ability to Detect the Fatigue Crack Initiation

Figure 71 shows that the piezo 1 and the MEMS S3 were the most active sensors in this experiment and their AE signal histories are similar. Both of these sensors detect the first AE signals in the time intervals of 90 s to 400 s. Then the AE signals were detected at 678 s and 1033 s. Determining the relevant signal due to the damage initiation requires further analyses; however, the preliminary evaluation of data indicates that the observed hits at the earlier time are due to external noise sources as none of two sensors detected those events at the same time.

6.4.1.3 Damage Evolution

In the first test, the alternative load ranges and frequencies were initially applied in order to determine the optimal load range and frequency, which would not generate excessive emissions at the grip locations. Due to initial loading history, the first specimen failed at lower number of cycles as compared to the second test. The duration of the second test with 3 Hz frequency was 2000 s while it was 900 s for the first test.

Figure 72 shows the cumulative energy of all the AE sensors with respect to time. All the sensors clearly show patterns similar to the expected patterns of brittle materials. The final rupture causes significant energy release that masks the released energy at earlier stages of the fatigue test.

Figure 73 shows a cross sectional view of the aluminum 7075 specimen used in this experiment after the fracture. In this picture, zones similar to the first set are observed.

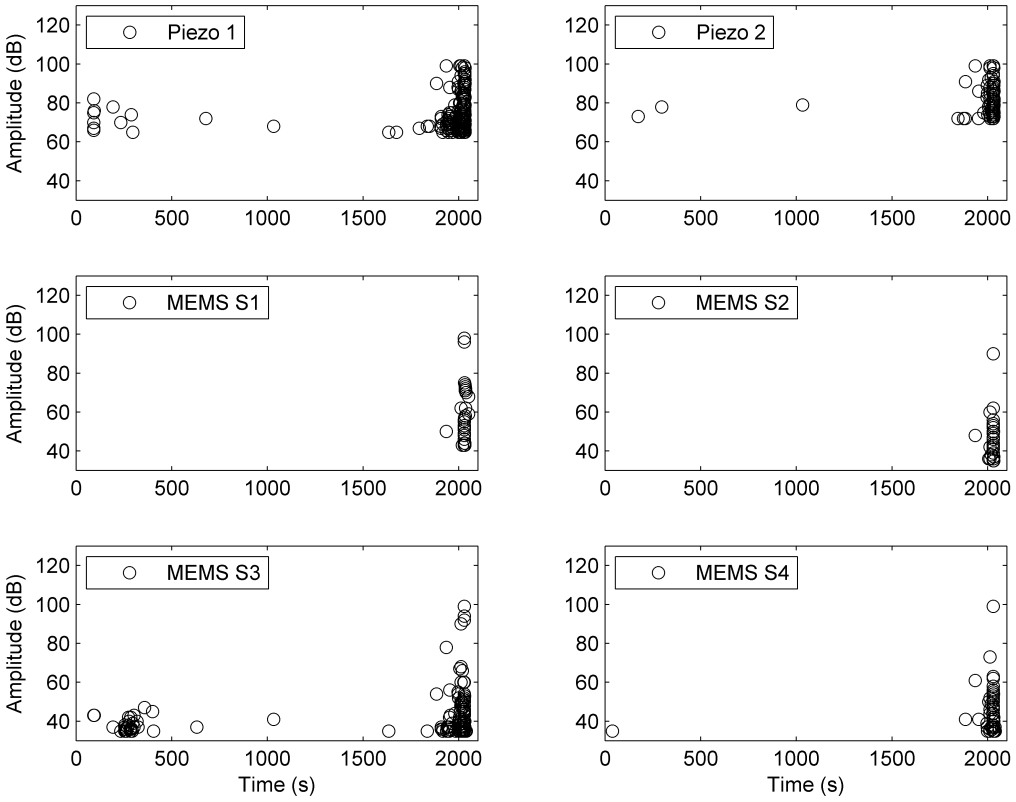

Figure 71. Amplitude of hits versus time for the fatigue test II

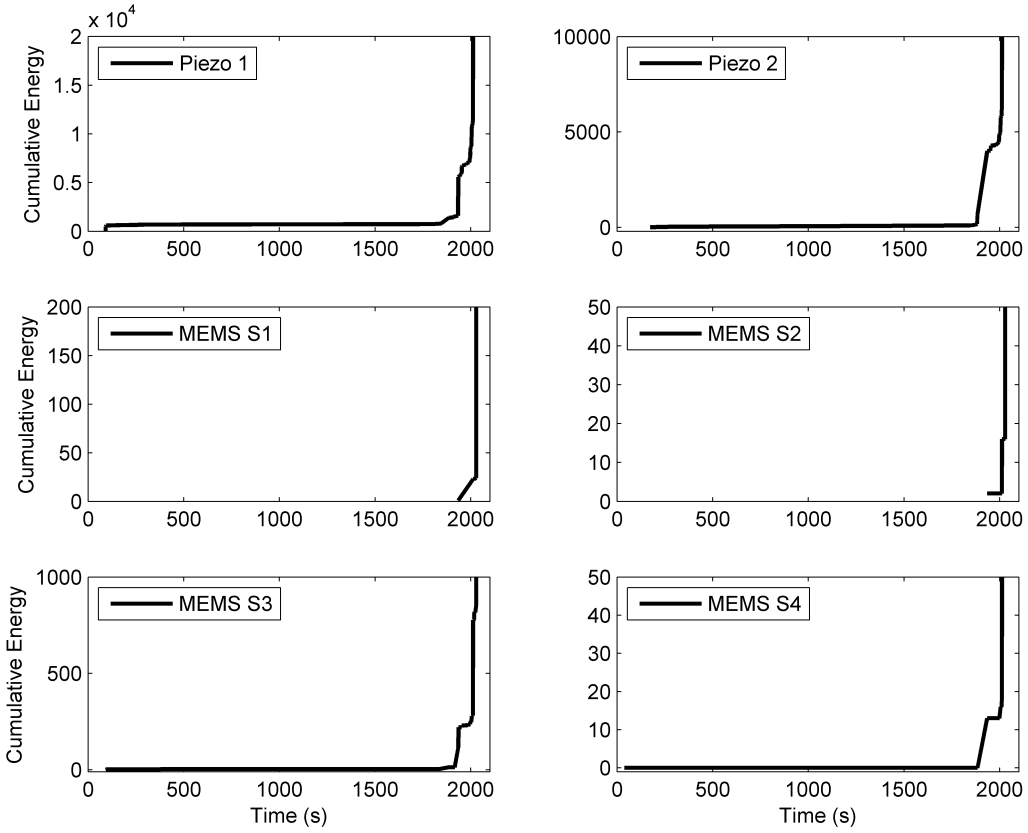

Figure 72. Cumulative energy of hits versus time for the fatigue test II

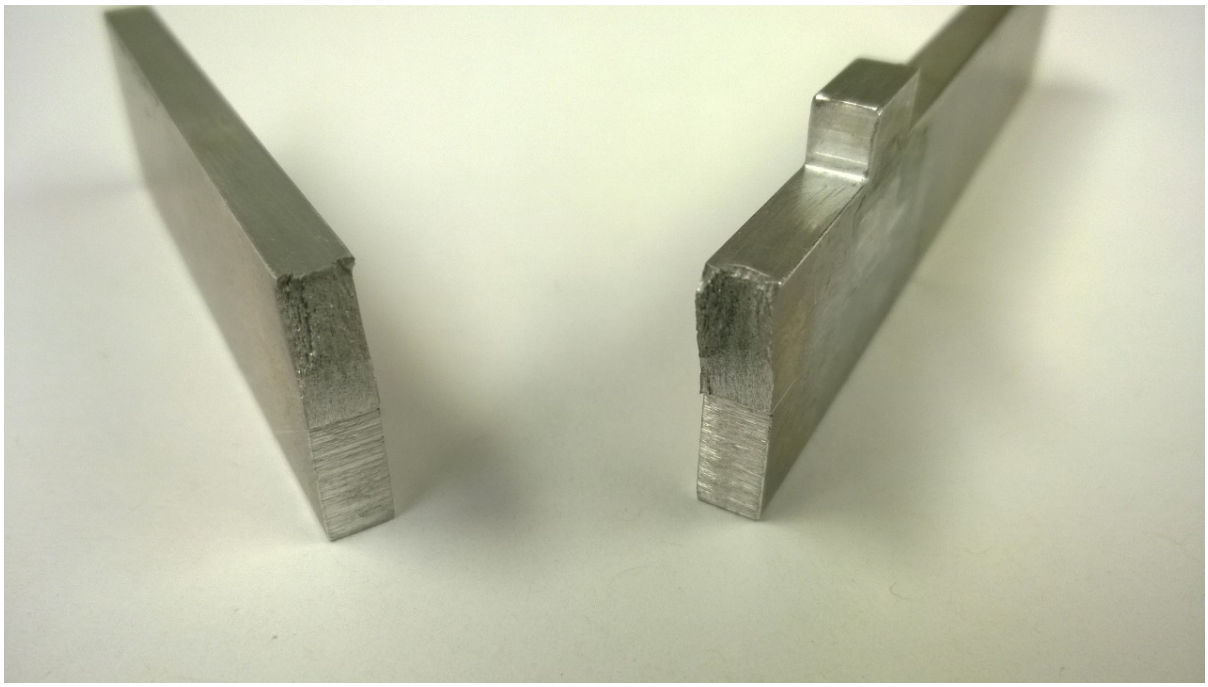

Figure 73. The failure section of the fatigue test II

6.4.1.4 Waveform Characteristics

Figure 74 shows the AE signal amplitudes detected by piezo 1 and MEMS S3. The waveforms of two AE signals highlighted on the figure are analyzed. Figure 75 shows the time domain waveforms and frequency spectra at time=1032 s for piezo 1 and MEMS S3. The pre-trigger time window before the arrival of the AE signal shows that MEMS S3 has lower noise level than piezo 1. A windowed image shown in the inset figure indicates that MEMS S3 clearly detects the wave arrival and the potential reflection at 250 μs; however, piezo 1 has more complex waveform due to wideband frequency response. MEMS S3 has two peaks at the design resonant frequencies.

Figure 76 shows the AE signals detected at t=1884 s. The amplitudes of the AE signals are higher than those detected at t=1032 s, which potentially indicates longer crack growth. Interestingly, the inset figure of MEMS S3 shows longer duration than that of time=1032 s (smaller amplitude). The initial duration of the AE signal recorded by the MEMS sensor may be correleated with the crack size if there is no dispersion problem.

6.4.2 MEMS Strain Sensors in Comparison to Strain Gauge

Similar to the first test, the MEMS strain sensors are compared with the metal gauge located on the specimen.

The thermal drift was again observed at both sensor types, Figure 77. In order to observe the fatigue cycles, a windowed time zone is plotted in Figure 78. Similar to the first fatigue test, the amplitude of metal gauge is higher than those of MEMS strain sensors because of their locations. The normalized and scaled time histories are shown in Figure 79. Similar to the first

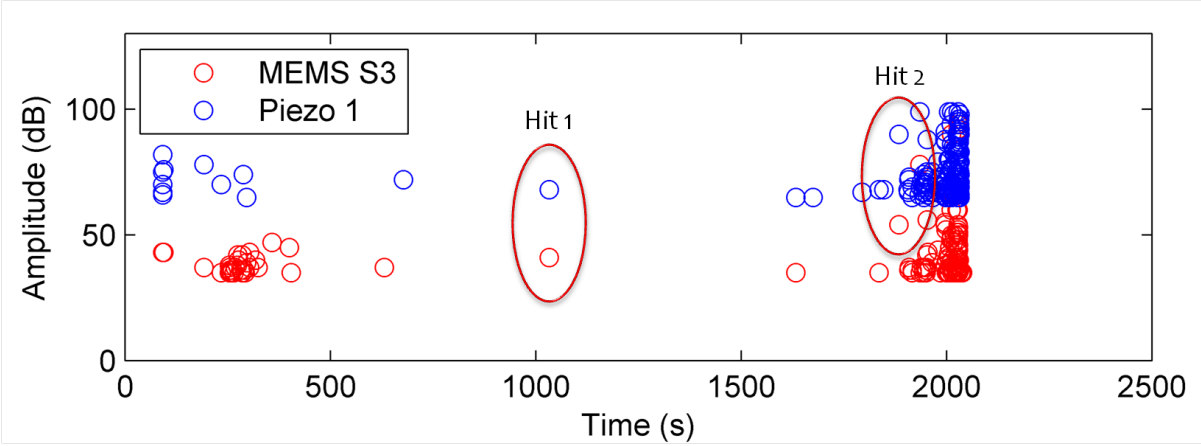

Figure 74. AE amplitudes of piezo 1 and MEMS S3

fatigue test, the MEMS strain sensors can track the fatigue cycles. This result demonstrates that regardless of the sensitivity and potential sources of errors, the MEMS strain sensors can be utilized to count the fatigue cycles. However, due to the effect of the thermal drift the absolute values of strain cannot be derived without special compensation.

6.4.3 AE/Strain Combined Behavior to Estimate Fatigue Cycles

Figure 80 shows the time history of the MEMS strain sensor together with the AE signal detected by the MEMS AE sensor. Similar to the first fatigue test, the AE signal was released at the peak of strain, which confirms that the strain data can be utilized to record the AE signals only above the strain threshold defined based on the expected load ranges.

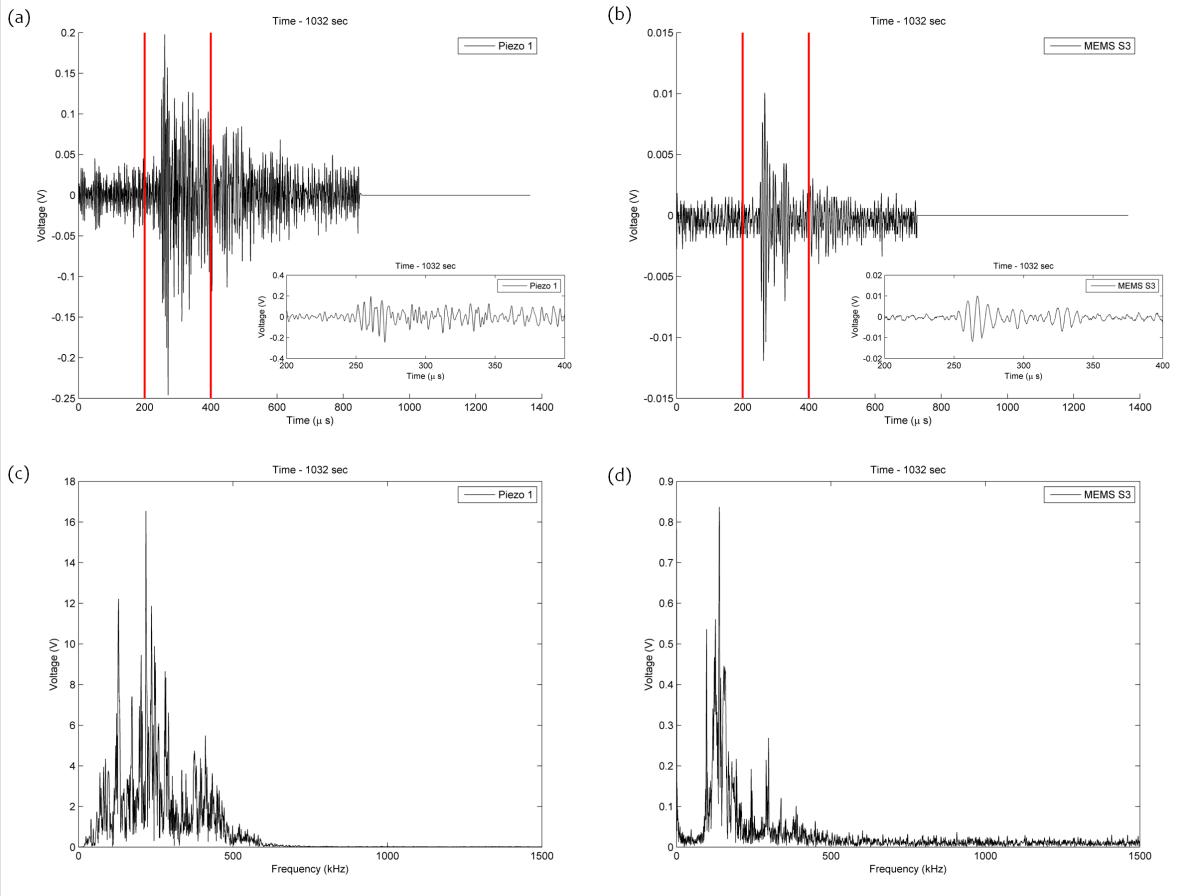

Figure 75. Waveforms and frequency spectra at t=1032 for (a, c) piezo 1, (b, d) MEMS S3.

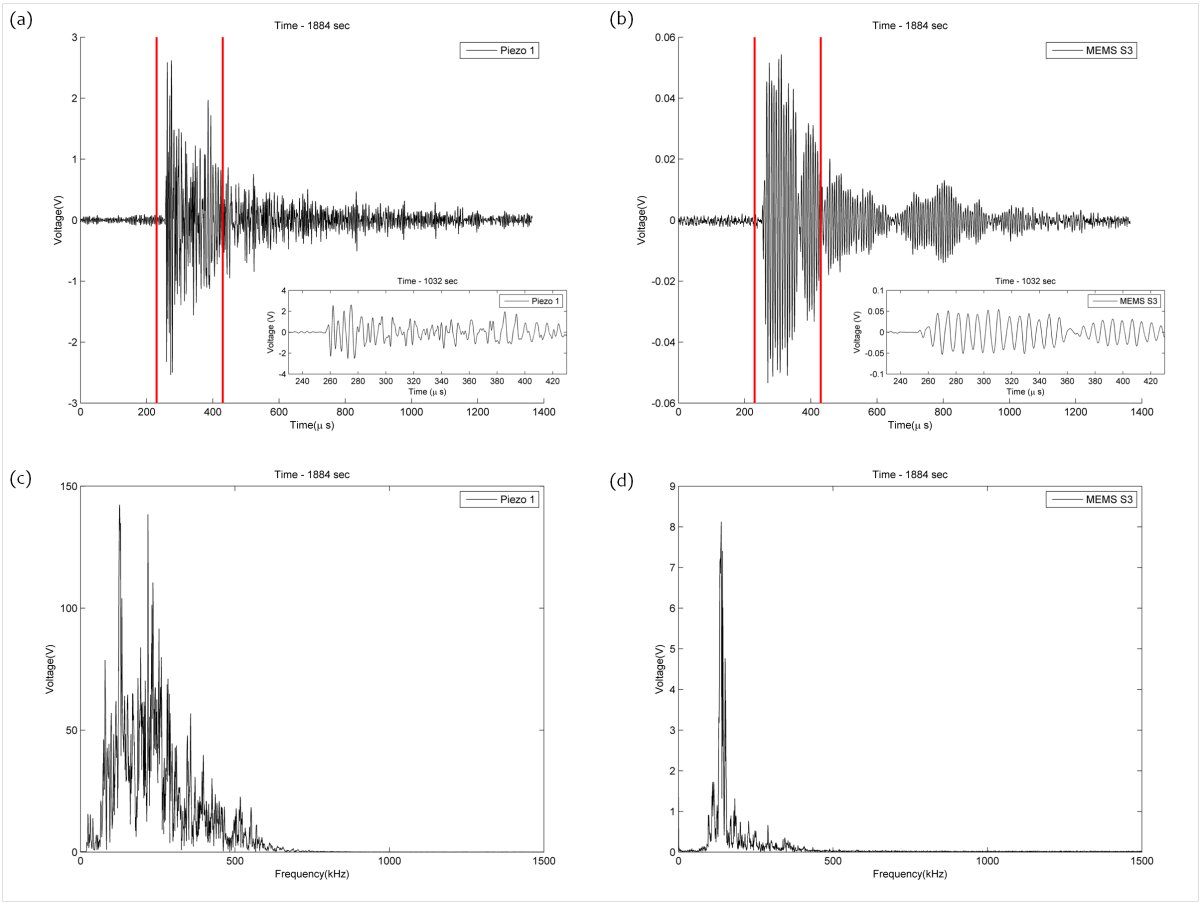

Figure 76. Waveforms and frequency spectra at t=1884 for (a, c) piezo 1, (b, d) MEMS S3.

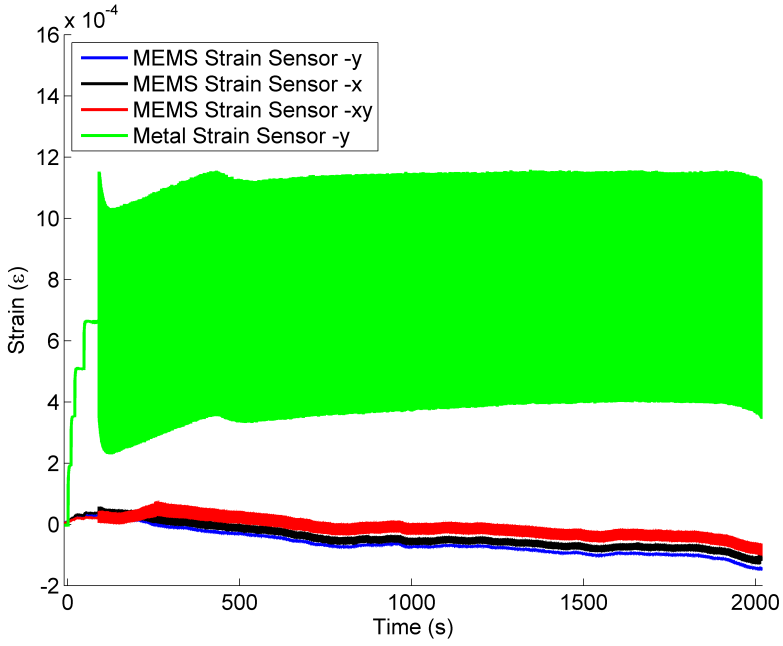

Figure 77. Overall time histories of metal gauge and MEMS strain sensors recorded at the second fatigue test

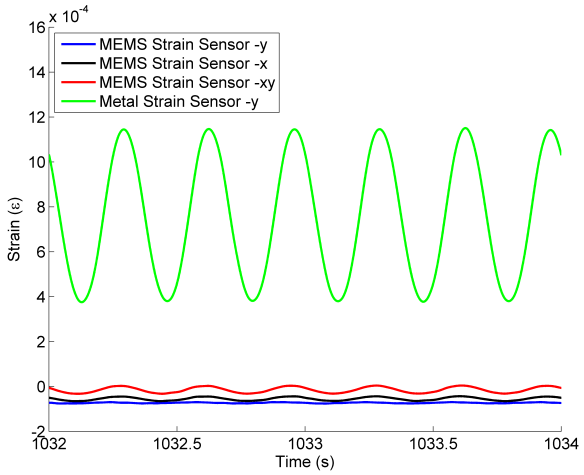

Figure 78. Windowed time histories of metal gauge and MEMS strain sensors for the fatigue test II

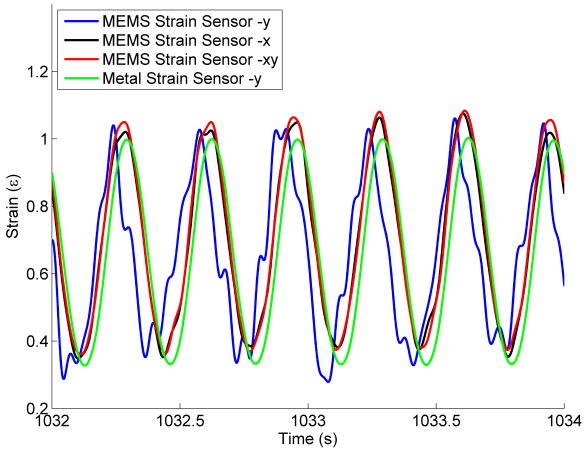

Figure 79. Windowed time histories of strain gauge and normalized, calibrated, and scaled MEMS strain sensors for the fatigue test II

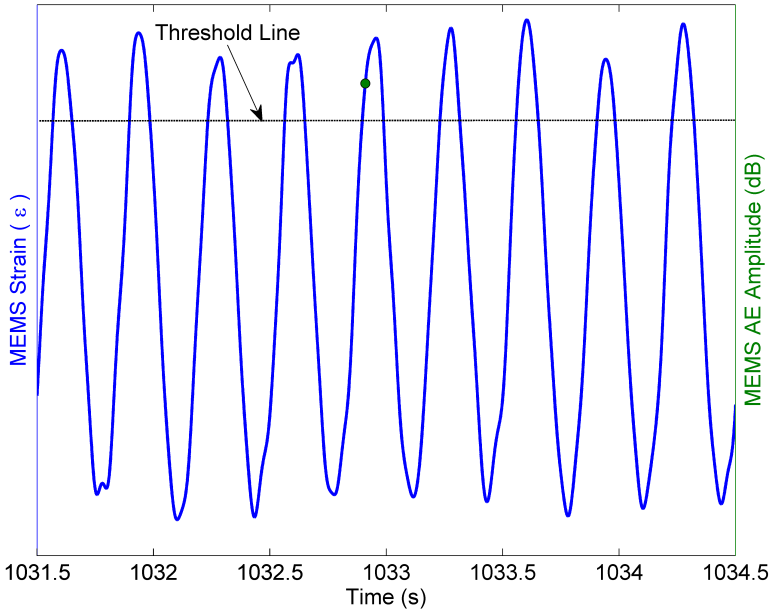

Figure 80. The concurrent presentation of the AE signal detected by the MEMS AE sensor, and the time history of the MEMS strain sensor for the fatigue test II

6.5 The Summary of the Combined MEMS AE and Strain Sensor Responses

Two fatigue tests were conducted in order to evaluate the performances of the MEMS AE and strain sensors in comparison to the conventional sensors. Additionally, the potential of using MEMS strain sensor as a trigger mechanism to detect the AE signal was evaluated. While the sensitivity of the MEMS AE sensors is lower than the piezoelectric sensors, they have better dynamic range due to lower threshold setting. The MEMS AE sensors have such a narrowband frequency response that they do not detect low frequency signals, typically emitted by the grip location at this particular test. The MEMS AE sensors can detect the initiation and the growth of the fatigue crack similar to the piezoelectric sensors. The MEMS strain sensors have significant thermal drift, which prevents the measurement of true strain. However, the sensors can detect the fatigue cycles similar to the metal gauge. The concurrent presentation of the MEMS AE and strain sensors show that the AE signals occur near the peak load; therefore, the strain data can be utilized as a trigger mechanism for recording the AE signal. This is especially crucial for long-term field testing where immense amount of data may be generated due to structural movement or operational condition. When the AE signal rate is intelligently reduced, the AE sensors can be combined with wireless nodes and energy harvesting devices.

CHAPTER 7

CONCLUSIONS AND FUTURE WORKS

7.1 Conclusions

In this study, new MEMS acoustic emission (AE) and strain sensors on the same device are designed, manufactured and characterized. The objective of this research is to reduce the drawbacks of the AE method through integrating AE and strain sensors on the same platform using micromachining methods for redundant measurement and generating a trigger mechanism for the AE sensors based on strain data in order to record AE data at high strain values when crack initiation and growth is expected. The major conclusions of this study are as follows:

- The electrical and mechanical properties of the OOP (out-of-plane) MEMS AE sensors obtained from numerical results agree with the experimental measurement. Through a more conclusive simulation the existing difference can be reduced even further.
- The signal to noise characteristics of MEMS AE sensors developed in this study have improved as compared to the sensors designs using the surface micromachining method. The sensors are functional in atmospheric pressure, and their sensitivities are improved to a level comparable to piezoelectric sensors' level of sensitivity. Considering the relative sizes of two sensor types, the MetalMUMPs allows for the design of a thick metal layer, which allowed further improvement in the sensor performance.

- The dielectric layer between the electrodes prevents the failure mode of stiction in the OOP MEMS AE sensors. This feature improves the reliability of these sensors.
- The OOP MEMS AE sensors are sensitive to the unique wave direction. This feature can be utilized in plate-like structures to select the correct wave velocity in order to increase the accuracy of source localization.
- The IP (in-plane) MEMS AE sensors are sensitive to both in-plane and out-of-plane directions. However, they are capable of detecting the initiation and growth of crack. The wave motions in two orthogonal directions may be separated using frequency-based filtering or differential mode operation of the area change sensor, which requires further research.
- The MEMS strain sensors with the transduction principle of piezoresistivity are designed, manufactured and characterized on the same device as the MEMS AE sensors. The gauge factor of the MEMS strain sensors is about twice the conventional metal gauges after considering all the strain losses through interfaces.
- The numerical results show the influence of trenching and the sensor location on the silicon substrate for the most efficient strain transfer from the structural surface to the sensing element. The ideal location of the strain sensor on the MEMS device is the center of the silicon substrate in order to increase the strain transfer, and sense the strains at different directions.
- The temperature dependence of the MEMS strain sensors is significant. The temperature dependency of polysilicon properties requires additional compensation to eliminate the

unwanted effect from the signal. Although the MEMS strain sensors have limitations on measuring true strain, the MEMS strain sensors can make good measurements of driving force estimates and fatigue cycle counts.

- The combined use of MEMS AE and strain sensors is evaluated to detect the initiation and growth of the fatigue crack at aluminum 7075. The experiments show that the MEMS AE sensors detect the crack behavior similar to the piezoelectric sensors. The detected emissions occur at high strain levels detected by the MEMS strain sensors, which can track the fatigue cycles, while they suffer from the thermal drift.

7.2 Contribution to Knowledge

The major contributions of this research to the knowledge are the following:

- The sensitivity of the MEMS AE sensors are brought to a comparable level to conventional piezoelectric AE sensors as the first time in literature.
- The MEMS strain sensors are combined with the MEMS AE sensors on the same package as the first time in the literature.

Combining AE and strain sensors on the same package tackles the major limitations of SHM methods such as the need of redundant measurement to increase the reliability and defining idle/active mode of the acoustic emission sensor using the strain sensor output to reduce the data processing need and the power consumption.

7.3 Future Works

The numerical and experimental results show that the sensors have unique characteristics, which require further research to understand the fundamental behavior. The future work of this study is as follows:

- The analytical and numerical models will be built in order to understand the electrical and mechanical behaviors of in-plane MEMS AE sensors.
- The damping values and their influence on the natural frequencies of AE sensors will be studied by analytical and numerical modeling.
- New generation of MEMS strain sensors will be manufactured with full-bridge sensors' geometry located at the center of the MEMS device in order to overcome the limitation of thermal drift and edge effect.
- Current packaging reduces the signal amplitude of MEMS AE sensors and the strain amplitude transferred to MEMS strain sensors. A new packaging will be designed specific to the MEMS device with the built-in electronics.
- The laboratory tests show that the MEMS AE sensors are not sensitive to friction emission, which is the most common extraneous emission source that the AE data is influenced by. The performance of the MEMS device will be evaluated in a field testing to show their immunity to the extraneous emissions.
- Accelerometers will be characterized to understand their electrical and mechanical behavior.

APPENDICES

Appendix A

COPYRIGHT PERMISSION

Subject: Permissions

From: Me

To: permissions@iop.org

Jun 17

Dear Publisher,

I'm a Co-Author of the following paper. I needed to use most of content published in that paper as a part of thesis dissertation and I need a written permission for that purpose.

MEMS and Nanotechnology, Volume 5 Conference Proceedings of the Society for Experimental Mechanics Series 2014, pp 81-87 In-Plane MEMS Acoustic Emission Sensors Development and Experimental Characterization

Hossain Saboonchi, Didem Ozevin

Thanks,

Hossain Saboonchi

Subject: Re: Permissions

From: Lucy Evans

To: Me

Jun 18

Appendix A (Continued)

Dear Hossain Saboonchi,

Thank you for your email and for taking the time to seek this permission.

When you assigned the copyright in your article to IOP, we granted back to you certain rights, including the right to include the article within any thesis or dissertation.

Therefore, please go ahead and make what use you wish of the content of the article.

The only restriction is that if, at a later date, your thesis were to be published commercially, further permission would be required.

Please let me know if you have any further questions.

In the meantime, I wish you the best of luck with the completion of your dissertation.

Kind regards,

Lucy Evans

Publishing Assistant

IOP Publishing

Subject: Permissions

From: Me

To: permissions@iop.org

Jun 17

Dear Publisher,

Appendix A (Continued)

I'm a Co-Author of the following paper. I needed to use most of content published in that paper as a part of thesis dissertation and I need a written permission for that purpose.

Smart Materials and Structures Volume 22 Number 9 H Saboonchi and D Ozevin 2013 Smart Mater. Struct. 22 095006 doi:10.1088/0964-1726/22/9/095006 MEMS acoustic emission transducers designed with high aspect ratio geometry

Thanks,

Hossain Saboonchi

Subject: Re: Permissions

From: Karen Thomas

To: Me

Jun 17

Dear Hossain Saboonchi,

Thank you for seeking permission from SPIE to reprint material from our publications. As author, SPIE shares the copyright with you, so you retain the right to reproduce your paper in part or in whole.

Publisher's permission is hereby granted under the following conditions:

(1) the material to be used has appeared in our publication without credit or acknowledgment to another source; and

(2) you credit the original SPIE publication. Include the authors' names, title of paper, volume title, SPIE volume number, and year of publication in your credit statement.

Appendix A (Continued)

Sincerely,

Karen Thomas for

Eric Pepper, Director of Publications

SPIE

P.O. Box 10, Bellingham WA 98227-0010 USA

360/676-3290 (Pacific Time) eric@spie.org

Title: MetalMUMPs-Based Piezoresistive Strain Sensors for Integrated on-chip Sensor Fusion

Author: Saboonchi, H.; Ozevin, D.

Publication: IEEE Sensors Journal

Publisher: IEEE

Logged in as: Hossain Saboonchi

Thesis / Dissertation Reuse

The IEEE does not require individuals working on a thesis to obtain a formal reuse license, however, you may print out this statement to be used as a permission grant:

Requirements to be followed when using any portion (e.g., figure, graph, table, or textual material) of an IEEE copyrighted paper in a thesis:

Appendix A (Continued)

1) In the case of textual material (e.g., using short quotes or referring to the work within these papers) users must give full credit to the original source (author, paper, publication) followed by the IEEE copyright line © 2011 IEEE.

2) In the case of illustrations or tabular material, we require that the copyright line © [Year of original publication] IEEE appear prominently with each reprinted figure and/or table.

3) If a substantial portion of the original paper is to be used, and if you are not the senior author, also obtain the senior author's approval.

Requirements to be followed when using an entire IEEE copyrighted paper in a thesis:

1) The following IEEE copyright/ credit notice should be placed prominently in the references: © [year of original publication] IEEE. Reprinted, with permission, from [author names, paper title, IEEE publication title, and month/year of publication]

2) Only the accepted version of an IEEE copyrighted paper can be used when posting the paper or your thesis on-line.

3) In placing the thesis on the author's university website, please display the following message in a prominent place on the website: In reference to IEEE copyrighted material which is used with permission in this thesis, the IEEE does not endorse any of [university/educational entity's name goes here]'s products or services. Internal or personal use of this material is permitted. If interested in reprinting/republishing IEEE copyrighted material for advertising or promotional purposes or for creating new collective works for resale or redistribution, please go to http://www.ieee.org/publications_standards/publications/rights/rights_link.html to learn how to obtain a License from RightsLink.

Appendix A (Continued)

If applicable, University Microfilms and/or ProQuest Library, or the Archives of Canada may supply single copies of the dissertation.

CITED LITERATURE

1. Saboonchi, H. and Ozevin, D.: MEMS acoustic emission transducers designed with high aspect ratio geometry. Smart Materials and Structures, 22(9):095006, September 2013.

2. Saboonchi, H. and Ozevin, D.: In-Plane MEMS Acoustic Emission Sensors Development and Experimental Characterization. In MEMS and Nanotechnology, Volume 5 Proceedings of the 2013 Annual Conference on Experimental and Applied Mechanics, eds. G. Shaw III, B. C. Prorok, L. Starman, and C. Furlong, volume 5 of Conference Proceedings of the Society for Experimental Mechanics Series, chapter 10, pages 81–87. Cham, Springer International Publishing, 2014.

3. Saboonchi, H. and Ozevin, D.: MetalMUMPs-Based Piezoresistive Strain Sensors for Integrated on-chip Sensor Fusion. IEEE Sensors Journal, (c):1–1, 2014.

4. Saboonchi, H. and Ozevin, D.: Combined MEMS Acoustic Emission and Strain Sensors for On Chip Data Fusion. In Structural Health Monitoring 2013 : A Roadmap to Intelligent Structures: Proceedings of the 9th International Workshop on Structural Health Monitoring, Stanford University, Stanford, CA, September 10-12, 2013, pages 2562–2569, 2013.

5. Transportation for America: The Fix We're In For : The State of Our Nation's Bridges 2013. Technical report, 2013.

6. Brownjohn, J. M. W.: Structural health monitoring of civil infrastructure. Philosophical transactions. Series A, Mathematical, physical, and engineering sciences, 365(1851):589–622, February 2007.

7. Howell, D. and III, H. S.: System for in-service strain monitoring of ordinary bridges. Journal of Bridge Engineering, 11(6):673–680, November 2006.

8. Chen, Y., Feng, M., and Tan, C.: Bridge structural condition assessment based on vibration and traffic monitoring. Journal of engineering mechanics, (August):747–758, 2009.

9. Nair, A. and Cai, C.: Acoustic emission monitoring of bridges: Review and case studies. Engineering Structures, 32(6):1704–1714, June 2010.

10. DOTNY: DOT NY, 2007.

11. OhioDOT: Manual of Bridge Inspection. 2010.

12. TALREJA, R.: Damage analysis for structural integrity and durability of composite materials. Fatigue & Fracture of Engineering Materials & Structures, 29(7):481–506, July 2006.

13. Pakzad, S., Kim, S., Fenves, G., and Glaser, S.: Multi-purpose wireless accelerometers for civil infrastructure monitoring. International Workshop of Structural Health Monitoring, 2005.

14. Chan, T.: Fatigue analysis and life prediction of bridges with structural health monitoring data — Part II: application. International Journal of Fatigue, 23(1):55–64, January 2001.

15. Liu, M., Frangopol, D. M., and Kim, S.: Bridge System Performance Assessment from Structural Health Monitoring: A Case Study. Journal of Structural Engineering, 135(6):733–742, June 2009.

16. Benedetti, M., Fontanari, V., and Zonta, D.: Structural health monitoring of wind towers: remote damage detection using strain sensors. Smart Materials and Structures, 20(5):055009, May 2011.

17. Dally, J. and Berger, J.: The Role of the Electrical Resistance Strain Gauge in Fracture Research. In Experimental Techniques in Fracture, pages 1–39. 1993.

18. Harlow, D. G. and Wei, R. P.: Probability modeling and material microstructure applied to corrosion and fatigue of aluminum and steel alloys. Engineering Fracture Mechanics, 76(5):695–708, March 2009.

19. Kulkarni, S. and Achenbach, J.: Structural Health Monitoring and Damage Prognosis in Fatigue. Structural Health Monitoring, 7(1):37–49, March 2008.

20. Figliola, R. S. and Beasley, D. E.: Theory and Design for Mechanical Measurements. John Wiley and Sons, 2010.

21. Jeric, K.: An experimental evaluation of the application of smart damping materials for reducing structural noise and vibrations. pages 4–17, 1999.

22. Yalcinkaya, H. and Ozevin, D.: The design and calibration of particular geometry piezoelectric acoustic emission transducer for leak detection and localization. Measurement Science and Technology, 24(9):095103, September 2013.

23. Pickwell, A. J., Dorey, R. a., and Mba, D.: Development of a thick film PZT foil sensor for use in structural health monitoring applications. IEEE transactions on ultrasonics, ferroelectrics, and frequency control, 60(2):373–9, March 2013.

24. Feng, G.-H. and Tsai, M.-Y.: Acoustic emission sensor with structure-enhanced sensing mechanism based on micro-embossed piezoelectric polymer. Sensors and Actuators A: Physical, 162(1):100–106, July 2010.

25. Ozevin, D., Pessiki, S., Greve, D., and Oppenheim, I.: A MEMS Transducer for Detection of Acoustic Emission Events. IEEE Sensors Journal, pages 776–779, 2005.

26. Harris, a. W., Oppenheim, I. J., and Greve, D. W.: MEMS-based high-frequency vibration sensors. Smart Materials and Structures, 20(7):075018, July 2011.

27. Auerswald, C., Sorger, a., Dienel, M., Shaporin, a., and Mehner, J.: MEMS acoustic emission sensor with mechanical noise rejection. International Multi-Conference on Systems, Sygnals & Devices, pages 1–6, March 2012.

28. Rausch, J., Heinickel, P., Koegel, B., Zogal, K., and Meissner, P.: Experimental comparison of piezoresistive MEMS and fiber bragg grating strain sensors. 2009 IEEE Sensors, pages 1329–1333, October 2009.

29. Kim, Y., Kim, Y., Lee, C., and Kwon, S.: Thin Polysilicon Gauge for Strain Measurement of Structural Elements. IEEE Sensors Journal, 10(8):1320–1327, August 2010.

30. Mohammed, A. a. S., Moussa, W. a., and Lou, E.: Optimization of geometric characteristics to improve sensing performance of MEMS piezoresistive strain sensors. Journal of Micromechanics and Microengineering, 20(1):015015, January 2010.

31. Alpuim, P., Gaspar, J., Gieschke, P., Ehling, C., Kistner, J., Goncalves, N. J., Vasilevskiy, M. I., and Paul, O.: Study of the piezoresistivity of doped nanocrystalline silicon thin films. Journal of Applied Physics, 109(12):123717, 2011.

32. Nathan, A. and Baltes, H.: Microtransducer CAD: Physical and Computational Aspects (Computational Microelectronics). Springer, 1999.

33. Smith, C.: Piezoresistance effect in germanium and silicon. Physical review, 919, 1954.

34. Kanda, Y.: A graphical representation of the piezoresistance coefficients in silicon. IEEE Transactions on Electron Devices, 29(1):64–70, January 1982.

35. Hopcroft, M. a., Nix, W. D., and Kenny, T. W.: What is the Young's Modulus of Silicon? Journal of Microelectromechanical Systems, 19(2):229–238, April 2010.

36. Johns, G.: Modeling Piezoresisitivity in Silicon And Polysilicon. Journal of Applied Engineering Mathematics April, 2:1–5, 2006.

37. French, P. and Evans, A.: Piezoresistance in polysilicon and its applications to strain gauges. Solid-State Electronics, 32(1), 1989.

38. Moradi, M. and Sivoththaman, S.: Strain Transfer Analysis of Surface-Bonded MEMS Strain Sensors. Sensors Journal, IEEE, 13(2):637–643, 2013.

39. Sosnowchik, B. D., Azevedo, R. G., Myers, D. R., Chan, M. W., Pisano, A. P., and Lin, L.: Rapid Silicon-to-Steel Bonding by Induction Heating for MEMS Strain Sensors. Journal of Microelectromechanical Systems, 21(2):497–506, April 2012.

40. Barlian, a. A., Park, W.-T., Mallon, J. R., Rastegar, A. J., and Pruitt, B. L.: Review: Semiconductor Piezoresistance for Microsystems. Proceedings of the IEEE. Institute of Electrical and Electronics Engineers, 97(3):513–552, January 2009.

41. Fraga, M. a., Furlan, H., Pessoa, R. S., Rasia, L. a., and Mateus, C. F. R.: Studies on SiC, DLC and TiO2 thin films as piezoresistive sensor materials for high temperature application. Microsystem Technologies, 18(7-8):1027–1033, January 2012.

42. Cowen, A., Mahadevan, R., Ohnson, S., and Hard, B.: MetalMUMPs design handbook. MEMSCAP Inc, 2012.

43. Liu, C.: Foundations of MEMS. Upper Saddle River,New Jersey: Prentice Hall;, 2nd edition, 2011.

44. Wright, A.: A Multi-Axis Capacitance MEMS Sensor System for Acoustiv Emission Sensing. Phd, Carnegie Mellon University, 2009.

45. Lindroos, V., Tilli, M., Lehto, A., and Motooka, T.: Handbook of Silicon Based MEMS Materials and Technologies (Micro and Nano Technologies). William Andrew Publishing, 2010.

46. Freedman, J.: Residual stress in single-crystal nickel films. IBM Journal of Research and Development, (October):449–455, 1962.

47. Reflective Index: http://refractiveindex.info/?group=CRYSTALS&material=Al2O3.

48. Davies, S., Edwards, C., Taylor, G., and Palmer, S.: Laser-generated ultrasound: its properties, mechanisms and multifarious applications. Journal of Physics D, 26:329–348, 1993.

49. Scruby, C. and Drain, L.: Laser Ultrasonics Techniques and Applications. Taylor & Francis, 1990.

50. Goldsmith, W.: Impact: The Theory and Pysical Behavier of Colliding Solids. Dover Publications, 2001.

51. Gary, J. and Hamstad, M.: On the far-field structure of waves generated by a pencil lead break on a thin plate. Journal of Acoustic Emission, 12(3/4):157–170, 1994.

52. Spengen, W. M. V. and Heeres, E. C.: A method to extract the lateral and normal components of motion from the capacitance change of a moving MEMS comb drive. Journal of Micromechanics and Microengineering, 17(3):447–451, March 2007.

53. Hautamaki, C. and Mantell, S.: Calibration of MEMS strain sensors fabricated on silicon: Theory and experiments. Journal of Microelectromechanical Systems, 12(5):720–727, October 2003.

54. Mohammed, A., Moussa, W., and Lou, E.: Development and experimental evaluation of a novel piezoresistive MEMS strain sensor. Sensors Journal, IEEE, 11(10):2220–2232, 2011.

55. Chuan, Y. and Chen, L.: The Compensation for Hysteresis of Silicon Piezoresistive Pressure Sensor. IEEE Sensors Journal, 11(9):2016–2021, September 2011.

56. Karihaloo, B.: What is Quasi-Brittle Fracture and How to Model its Fracture Behaviour. The FESI Bulletin, 4(4):18–20, 2010.

57. Paris, P. and Erdogan, F.: A critical analysis of crack propagation laws. Journal of Basic Engineering, Transactions of the American Society of Mechanical Engineers, pages 528–534, 1963.

VITA

HOSSAIN SABOONCHI

hsaboo2@uic.edu

AREAS OF INTEREST

Micro-electro-mechanical systems (MEMS), piezoresistive and capacitive sensors, multiphysics finite element models, fracture mechanics, acoustic emission, fluid dynamics, nondestructive evaluation and testing

EDUCATION

2014 University of Illinois at Chicago, Chicago, IL

Ph.D. in Civil Engineering,

Thesis: A Family of MEMS Sensors for Structural Health Monitoring

2008 Isfahan University of Technology, Isfahan, Iran

Master of Science in Mechanical Engineering,

Thesis: Multi-Block Lattice Boltzmann Method Fluid Flow Simulations

2005 Yazd University, Yazd, Iran

Bachelor of Science in Mechanical Engineering,

EXPERIENCE

Research Assistant/Teaching Assistant, Jan. 2011- Aug. 2014

University of Illinois at Chicago, Chicago, IL

- Developed unique MEMS acoustic emission, strain and acceleration sensors on the small footprint for on-chip sensor fusion;
- Characterized capacitive MEMS AE sensors using impedance analyzer, Nd:YAG Q-switched laser, laser Doppler vibrometer and mechanical testing;
- Characterized piezoresistive MEMS strain sensors using SEM, probe station, mechanical and thermal testing;
- Developed FEM multiphysics models for comparing the predictions with experimental results.

Substitute Instructor, Aug. 2010- Sep. 2010

Southern Illinois University Carbondale, Carbondale, IL

- Instructed the "ME 300 – Engineering Thermodynamics "

Research Assistant/Teaching Assistant, Aug. 2009- Dec. 2010

Southern Illinois University Carbondale, Carbondale, IL

- Developed a 2D direct numerical simulation Fortran code in order to study the "Manipulation of Red Blood Cells with Electric Field";
- Developed a 3D direct numerical simulation Fortran-MPI code in order to "Simulate the 2-phase interaction of gas bubble inside a liquid medium";
- Validated the performance of the Fortran-MPI code on the Purdue university supper computer, LSU supper computer and a local cluster computer.

- Post processed and rendered animations in order to visualize the movement of bubble interface through the liquid using developed Matlab codes.

Knowledge Advisor, Dec. 2008-Jun. 2009

Micro Center, Rockville, MD

- Advised customers for their Technical computer related questions and assist them with their purchases.

Research Assistant/Teaching Assistant, Aug. 2005- May 2008

Isfahan University of Technology, Isfahan, Iran

- Developed a Matlab code to numerically simulate fluid flow on a few benchmarks using an improved macroscopic equations" Multi-Block Lattice Boltzmann Method";

Internship, May 2004- Aug. 2004

Isfahan Power Planet Maintenance Co., Isfahan, Iran

- Assisted repair engineers on daily inspections of the thermal power plants;
- Gathered details of each unit in the power plant and prepared a report.

EXPERTISE

Micro-Electro-Mechanical Systems (MEMS), Structural Health Monitoring (SHM), Computational Fluid Dynamics (CFD), Heat Transfer, Solid Mechanics.

Trained to Operate: Lithography, Varian E-beam evaporation, Oxidation furnace, LPCVD, Wire-bonding Machine, Oxford DIRE, Optical Microscope, Profilometer, Probe station, Impedance

analyzer, Nd:YAG Q-switched Laser, Pocket UT device and AE data acquisition systems, Oscilloscope, laser Doppler vibrometer and mechanical testing.

Engineering Software: COMSOL Multiphysics, ANSYS CFX, AutoCAD, NI LabVIEW (CLAD certified), Cadence, L-Edit.

Computer Programming: Matlab, C, Fortran, Parallel Programming (MPI)

Operating Systems: Windows, Linux, Mac OS X Lion, Sun Solaris.

General Software: MS Word, Excel, PowerPoint, and Latex.

HONORS AND AWARDS

- Christopher B and Susan S. Burke Exceptional Academic Achievement Award 2013.
- Selected to represent Civil and Materials Engineering Department research focuses at Dalian University of Technology (China), SHM Workshop founded by National Science Foundation 2013.
- 1st Rank among Mechanical Engineering Department B.Sc. Students, Spring 2004.
- 2nd Rank among Mechanical Engineering Department B.Sc. Students, Fall 2004

REFEREED JOURNAL PUBLICATIONS

- Saboonchi, H. and Ozevin, D. "Combined MEMS Acoustic Emission and Strain Sensors for On Chip Data Fusion", in preparation.
- Saboonchi, H. and Ozevin, D. "MetalMUMPs-Based Piezoresistive Strain Sensors for Integrated on-chip Sensor Fusion", IEEE Sensors Journal, doi: 10.1109/JSEN.2014.23479711.

- Saboonchi, H. and Ozevin, D. "MEMS acoustic emission transducers designed with high aspect ratio geometry", Smart Materials and Structures, Vol. 22, 095006, 2013.

CONFERENCE PUBLICATIONS

- Saboonchi, H. and Ozevin, D. "Numerical and Experimental Characterization of Piezoresistive MEMS Strain Sensors," SPIE Smart Structures/NDE Conference, San Diego CA, March 2014.
- Saboonch, H. and Ozevin, D. "Combined MEMS Acoustic Emission and Strain Sensors for On Chip Data Fusion," 9th International Workshop on Structural Health Monitoring, Stanford CA, September 2013.
- Saboonchi, H. and Ozevin, D. "In-Plane MEMS Acoustic Emission Sensors Development and Experimental Characterization," SEM 2013 Annual Conference and Exposition on Experimental and Applied Mechanics, Lombard IL, June 3-5 2013.
- Saboonchi, H. and Ozevin, D. "Numerical and Experimental Characterizations of Low Frequency MEMS AE Sensors," SPIE Smart Structures/NDE, San Diego CA, March 2013.
- Saboonchi, H. and Ozevin, D. "Numerical Simulation of Novel MEMS Strain Sensor for Structural Health Monitoring," ASCE Structural Congress, Chicago IL, March 2012.
- Saboonchi, H. and Ozevin, D. "Numerical Demonstration of MEMS Strain Sensor," SPIE NDE/Smart Structures International Conference, San Diego CA, March 2012.

- Saboonchi, H. and Ozevin, D. "Optimization of Design Parameters of a Novel MEMS Strain Sensor Used for Structural Health Monitoring of Highway Bridges," COMSOL Conference, Boston MI, October 2011.
- Punchihewa, K. G., Saboonchi, H., et al., "Improvements of the Sensitivity and Operating Range of MEMS-based Resistive-type Vacuum Gauges," Technical Digest, 24th International Vacuum Nanoelectronics Conference, Wuppertal Germany, July 2011.

SYNERGISTIC ACTIVITIES

- Certified LabVIEW Associate Developer (CLAD).
- Member of American Society of Civil Engineers (ASCE).
- One of founding member of UIC Department of Civil and Materials Engineering (CME) Graduate Student Association.
- Participated to the MicroFluids workshop at The Lurie Nanofabrication Facility (LNF), 2014, Ann Arbor, MI.

ADVANCED COURSES TAKEN

Micro-fabrication and Micro-devices, N/MEMS Sensors and Actuators, Characterization of Materials by Nondestructive Testing, Structural Dynamics, Fracture Mechanics and Failure Analysis, Continuum Mechanics.